LEABHARLANN CHOLÁISTE NA TRÍONÓIDE, BAILE ÁTHA CLIATH | TRINITY COLLEGE LIBRARY DUBLIN
Ollscoil Átha Cliath | The University of Dublin

Terms and Conditions of Use of Digitised Theses from Trinity College Library Dublin

Copyright statement

All material supplied by Trinity College Library is protected by copyright (under the Copyright and Related Rights Act, 2000 as amended) and other relevant Intellectual Property Rights. By accessing and using a Digitised Thesis from Trinity College Library you acknowledge that all Intellectual Property Rights in any Works supplied are the sole and exclusive property of the copyright and/or other IPR holder. Specific copyright holders may not be explicitly identified. Use of materials from other sources within a thesis should not be construed as a claim over them.

A non-exclusive, non-transferable licence is hereby granted to those using or reproducing, in whole or in part, the material for valid purposes, providing the copyright owners are acknowledged using the normal conventions. Where specific permission to use material is required, this is identified and such permission must be sought from the copyright holder or agency cited.

Liability statement

By using a Digitised Thesis, I accept that Trinity College Dublin bears no legal responsibility for the accuracy, legality or comprehensiveness of materials contained within the thesis, and that Trinity College Dublin accepts no liability for indirect, consequential, or incidental, damages or losses arising from use of the thesis for whatever reason. Information located in a thesis may be subject to specific use constraints, details of which may not be explicitly described. It is the responsibility of potential and actual users to be aware of such constraints and to abide by them. By making use of material from a digitised thesis, you accept these copyright and disclaimer provisions. Where it is brought to the attention of Trinity College Library that there may be a breach of copyright or other restraint, it is the policy to withdraw or take down access to a thesis while the issue is being resolved.

Access Agreement

By using a Digitised Thesis from Trinity College Library you are bound by the following Terms & Conditions. Please read them carefully.

I have read and I understand the following statement: All material supplied via a Digitised Thesis from Trinity College Library is protected by copyright and other intellectual property rights, and duplication or sale of all or part of any of a thesis is not permitted, except that material may be duplicated by you for your research use or for educational purposes in electronic or print form providing the copyright owners are acknowledged using the normal conventions. You must obtain permission for any other use. Electronic or print copies may not be offered, whether for sale or otherwise to anyone. This copy has been supplied on the understanding that it is copyright material and that no quotation from the thesis may be published without proper acknowledgement.

Novel magnetic materials for spin electronic applications

by

Ciara Bridget Fitzgerald

A thesis submitted to the University of Dublin in application for the degree of Doctor of Philosophy

Department of Physics
Trinity College Dublin

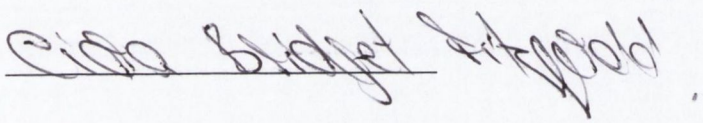
December 2004

TRINITY COLLEGE
07 FEB 2005
LIBRARY DUBLIN
THESIS
7463

Declaration

This thesis is submitted by the undersigned for examination for the degree of Doctor of Philosophy at the University of Dublin. It has not been submitted as an exercise for a degree at any other university.
This thesis, apart from the advice, assistance and joint effort mentioned in the acknowledgements and in the text, is entirely my own work.

I agree that the library may lend or copy this thesis freely on request.



Ciara Bridget Fitzgerald

Summary

Among various types of semiconductors, oxide semiconductors are the most promising host compounds to realise high Curie temperatures with transition metal doping. Room temperature ferromagnetism in dilute oxide semiconductors was first reported in anatase and rutile phases of TiO_2 doped with Co in 2001. Various other transition metal doped oxide semiconductors (SnO_2, ZnO) have been reported to be ferromagnetic at room temperature. High temperature ferromagnetism is not expected in these materials because the magnetic doping level is far below the cation percolation threshold x_p needed for long-range order based on superexchange or double exchange interactions. These reports were greeted with scepticism, and the belief that the data somehow reflected the presence of secondary ferromagnetic phases rather than intrinsic long range ferromagnetism. The possibility of an extrinsic origin for the ferromagnetism, such as ferromagnetic impurity segregation, could not be ruled out in some cases.

To understand better the origin of the magnetism in these novel magnetic systems we have carried out careful systematic analysis of three systems:

1. $Sn_{1-x}M_xO_2$, where M = Mn, Fe or Co, $0 \leq x \leq 0.3$
2. $Zn_{1-x}M_xO$ for M = Sc - Cu where x = 0.05 nominally, and $Zn_{1-x}Co_xO$ where $0 \leq x \leq 0.25$
3. $Hf_{1-x}Co_xO_2$ where $0 \leq x \leq 0.03$, and $Hf_{1-x}M_xO_2$ where M = Sc, Ti and Ta and x = 0.05 nominally

The most striking feature of the present work is the discovery of room temperature ferromagnetism in undoped HfO_2 films - evidence is presented for defect-induced ferromagnetism in these samples. Transition metal doping in all three systems leads to magnetic moments exceeding the spin-only values at concentrations far below the percolation threshold. The strongest evidence of intrinsic ferromagnetism in these oxides comes when their properties clearly differ from those of any conventional ferromagnetic material - for example the huge anisotropy of the saturation magnetisation that we have found. No known room temperature ferromagnets approach this level of anisotropy at room temperature - and hence secondary ferromagnetic phases cannot be responsible.

We find evidence for two contributions to the magnetisation - one due to transition metal doping and a second due to defects at the film/substrate interface. A novel exchange mechanism involving donor electrons in a defect related impurity band has been proposed to account for the ferromagnetism of these oxides. We have been able to model the behaviour of both contributions, resulting in a good fit to the experimental data.

Meteoritic graphite and carbonado samples have also been examined following recurrent reports of weak ferromagnetism in graphite and synthetic carbon materials such as rhombohedral C_{60}. We find that ferromagnetism in the meteoritic graphite is due to a magnetic proximity effect induced at the interface due to magnetic inclusions.

There is an ongoing quest for ferromagnetic semiconductors with a Curie temperature above room temperature which could be used for a second generation of spin electronics, as well as a search for transparent ferromagnets which could add an optoelectronic dimension. The implications of ferromagnetic carbon, whatever its origin, are likely to be wide reaching - potentially we have a zero-gap, high temperature ferromagnetic semiconductor.

Acknowledgements

I would like to thank Prof. J. M. D. Coey for supervising my thesis work and for supporting and encouraging me along the way. Thanks to M. Venkatesan for all of your help over the last four years - for SQUID and resistivity measurements, for your patience in teaching me the skills I've needed to develop, and for reading my thesis so carefully - I've really enjoyed working with you. Thanks to Prof. James Lunney for allowing me to use his PLD facilities, to Alex for Mössbauer analysis, to Lucio for x-ray reflectivity measurements, to Oscar for thickness measurements and AFM/MFM work, to Richard for TEM images, to Yang Zhou for AGFM data, and to CMA for allowing me to use their SEM facilities.

Thanks to everyone in the lab - Eoin, Nandu, Fernando, Robbie, Plamen, Emma and Treasa - to everyone in SFI, to the many summer students that have come through the lab, to Rui, Janko and Cora, and of course, to the members of Group L. Thanks to everyone else in the department who have helped me over the last few years - Sandra, Jackie, Michelle, Susan, Dave, Mick, John, Jemmer, Tom, Ken, Joe, Nigel and Kevin.

Thanks also to my parents and sisters for their support and encouragement over the last few years, and to Cian, not only for lattice simulations, but for taking such good care of me.

Thanks to Enterprise Ireland and Science Foundation Ireland for financing this work.

Table of Contents

Summary

1. Introduction **4**

1.1 Spin electronics 4
1.1.1 Spin diffusion lengths and spin polarisation 5
1.1.2 Devices – spin valves and tunnel junctions 6
1.1.3 Materials for spin electronics 9
1.1.4 Chapter outline 11

1.2 Semiconductors 12
1.2.1 Dilute magnetic semiconductors 14
1.2.2 II-VI semiconductors 16
1.2.3 III-V semiconductors 18
1.2.4 Oxide magnetic semiconductors 20
1.2.5 Group IV based magnetic semiconductors 22
1.2.6 Semiconductor spin electronics 24

1.3 Other novel materials 26
1.3.1 Carbon-based ferromagnets 26
1.3.2 High-k dielectrics – hafnium dioxide 29
1.3.3 Calcium, Strontium, Barium and Europium hexaborides 30

1.4 Impurity phases 32

References 34

2. Experimental procedures **40**

2.1 Sample preparation 40
2.1.1 Target production 40
2.1.2 Pulsed laser deposition 40

2.2 Phase identification and structural characterisation 43
2.2.1 X-ray diffraction (XRD) 43
2.2.2 X-ray reflectivity 44
2.2.3 Microscopy 45
2.2.4 Optical spectrometry 46
2.2.5 Chemical Analysis 47

2.3 Magnetic measurements 47
2.3.1 Thermogravimetric analysis 47
2.3.2 Magnetic Force Microscopy (MFM) 48
2.3.3 Vibrating sample magnetometry 48
2.3.4 Superconducting Quantum Interference Device (SQUID) 49

2.4 Electrical measurements 50
2.4.1 Four-point resistivity measurements 50

3. $Sn_{1-x}M_xO_2$, M = Mn, Fe, Co **51**

3.1 Introduction 51
3.2 Bulk material 52
3.3 Thin films 55
3.4 Indium-tin oxide (ITO) 68
3.5 Discussion 69

References 72

4. Transition metal doped ZnO **73**

4.1 Introduction 73
4.2 Structure and composition 75
4.3 Thin films 77
4.3.1 $Zn_{1-x}Co_xO$ 77
4.3.2 $Zn_{1-x}M_xO$, M = Sc – Cu 87
4.3.3 Multilayer structures 92
4.4 Discussion 93

References 96

5. HfO_2 **98**

5.1 Introduction 98
5.2 Undoped HfO_2 100
5.2.1 Bulk material 100
5.2.2 Films 101
5.3 Doped HfO_2 films 108
5.4 Discussion 110

References 112

6. Discussion – dilute magnetic oxides **113**

6.1 Introduction 113
6.2 Results 115
6.2.1 Giant moments 115
6.2.2 Anisotropic saturation magnetisation 119
6.2.3 Hysteresis 120
6.3 Impurities and secondary phases 121
6.4 The syndrome 123
6.5 Conclusion 128

References 129

7. Ferromagnetic carbon **131**

7.1 Introduction 131
7.2 The Canyon Diablo meteorite 132
7.2.1 Optical microscopy and scanning electron microscopy 133
7.2.2 Structural and compositional analysis 135
7.2.3 Magnetic properties 136
7.3 Carbonados 142
7.3.1 Structural and compositional analysis 143
7.3.2 Magnetic properties 144

7.4 Discussion 147

Appendix A: Mineral names and their chemical compositions **149**

References 150

8. Further work **152**

8.1 Dilute magnetic oxides 152
8.2 Ferromagnetic carbon 154

References 156

Publications **157**

Chapter 1

Introduction

1.1 Spin electronics

While traditional electronic devices rely only on the charge of the electron, the field of spin electronics aims to manipulate its spin. Although this is a relatively new area of study, there have already been advances in understanding spin-dependent transport processes in various physical systems (eg metallic multilayers with giant magnetoresistance), and it has led to the development of magnetic memory storage, MRAM (magnetic random access memory), and read head disk technology. As many current technologies and devices are based on semiconductor materials, combining their properties with controlled electron spin is seen as the next target and could lead to the combination of the three broad areas of information technology into a single device (figure 1.1):

1. Processing - employing electron charge in a semiconductor
2. Storage - using electron spin in a ferromagnet
3. Communication - frequently using optical signals

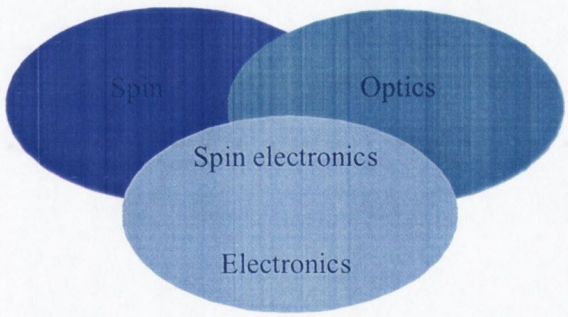


Figure 1.1 Spin-electronics could lead to new devices for information technology by combining traditional electronics and optoelectronics with spin.

1.1.1 Spin diffusion lengths and spin polarisation

In the 1930's Mott [1] suggested that spin-up and spin-down conduction electrons in metallic ferromagnets could be considered as independent types of charge carriers, with different transport properties - and so contributing differently to electrical transport processes. The spin-up and spin-down conduction bands are split due to the ferromagnetic exchange field, leaving different band-structures at the Fermi surface. If the spin-up channel has a greater density of electron states (or mobility) at the Fermi level than the spin-down states, then they will participate more in the conduction process.

If a current is passed from a material with a spin asymmetry, for example more up- than down-spins, into a material with no spin asymmetry, a surplus of up-spins will appear in the second material. This surplus is called spin accumulation, and is associated with a small magnetic moment. Spin-flip processes in the second material can return these up-spins to down-spins (figure 1.2). λ_{sd}, the spin diffusion length, is the average distance travelled by a spin before a spin-flip event occurs, and is given by (1.1).

$$\lambda_{sd} = \sqrt{\frac{\lambda \nu_F \tau_{\uparrow\downarrow}}{3}} \tag{1.1}$$

where λ is the mean free path, ν_F is the velocity of the spin (the Fermi velocity) and $\tau_{\uparrow\downarrow}$is the time taken for the spin to flip.

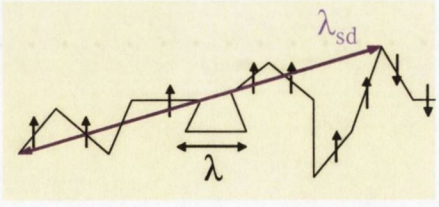


Figure 1.2 Illustration of spin travelling through a material, where λ is the mean free path and λ_{sd} is the spin diffusion length

Impurities reduce the spin diffusion length by reducing the mean free path, and may

	$\lambda^{\uparrow}$	$\lambda^{\downarrow}$	λ_{sd} (nm)
Semiconductor	200	200	2000
Semimetal	> 50	> 50	> 500
s-band metal	30	30	300
d-band metal	5.0	0.9	30

Table 1.Typical mean free path lengths for up and down spins, and spin diffusion lengths for semiconductors, semimetals and metals - all are in nm

also reduce the spin-flip time ($\tau_{\uparrow\downarrow}$) by introducing more spin-orbit scattering. Some typical mean free path lengths for up and down spins, as well as spin diffusion lengths are shown in Table 1. Semiconductors have the longest spin diffusion lengths, followed by semimetals, s-band metals and finally d-band metals.

The spin polarisation, P, of a material indicates the extent to which there are carriers of one spin direction in excess of the other and is given by (1.2):

$$P = \frac{(n^{\uparrow} - n^{\downarrow})}{(n^{\uparrow} + n^{\downarrow})} \tag{1.2}$$

where $n^{\uparrow,\downarrow}$ is the density of states at the Fermi level. Fe, Co and Ni have spin polarisations of 45, 42 and 44 % respectively, while CrO_2, a half-metal, has 100 % spin polarisation.

1.1.2 Devices - spin valves and tunnel junctions

There are three prerequisites for spin electronics devices [2]:

1. The presence of spin-polarised carriers
2. Effi cient transfer of these spins across an interface
3. Once they cross the interface the spin polarisation must be preserved for long enough to carry out the desired operation

The simplest spin-electronic device is the two-terminal spin-valve, a magnetic field sensor which forms the basis of hard disk read heads, illustrated in figure 1.3 below. In current generation spin valves the current flows in the plane of the metal stack (current in

plane, CIP).

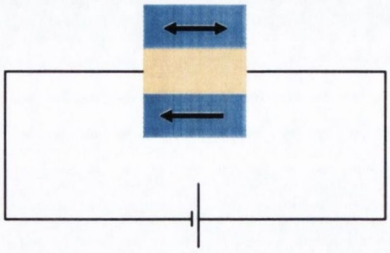


Figure 1.3 A CIP spin valve with a paramagnetic metal (orange) between two ferromagnetic layers (blue)

An externally applied magnetic field can switch the relative magnetic orientations of the two ferromagnetic layers - so that they are parallel or anti-parallel. If the thickness of the paramagnetic layer is comparable with or smaller than its spin-diffusion length the spin accumulation can extend all the way across it to the second ferromagnetic layer which acts as a spin filter. When the ferromagnetic layers lie parallel to each other the resistance across the structure is lower than in the antiparallel state - with changes in resistance of order 10 % between the two states - giving rise to giant magnetoresistance (GMR). Magnetoresistance (MR) is defined as:

$$MR = \frac{R^{\uparrow\downarrow} - R^{\uparrow\uparrow}}{R^{\uparrow\uparrow}} \tag{1.3}$$

where $R^{\uparrow\downarrow}$ and $R^{\uparrow\uparrow}$ are the resistances in the antiparallel and parallel states. MR is related to spin polarisation in a simple model [3] by the expression 1.4:

$$MR = \frac{2P}{(1+P^2)} \tag{1.4}$$

An antiferromagnetic layer can be used to pin the direction of magnetisation of one of the ferromagnetic layers in a spin-valve by exchange coupling (figure 1.4). The direction of magnetisation of the free ferromagnetic layer can then be switched from parallel to anti-parallel to the pinned layer by applying a small field. Manganese alloys such as FeMn, NiMn

and IrMn are commonly used as well as some antiferromagnetic oxides such as NiO and α-Fe $_2O_3$.

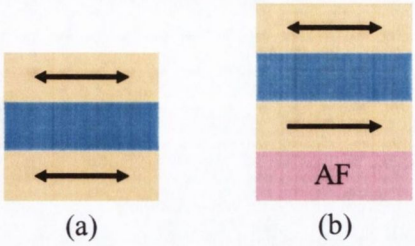


Figure 1.4 (a) The original spin valve structure where both ferromagnetic layers (orange) are free to change the direction of their magnetisation and (b) the direction of magnetisation of the lower ferromagnetic layer is pinned by the antiferromagnetic (AF) layer

If an insulating layer was sandwiched between two metallic electrodes and a voltage applied between them, current could travel from one electrode to the other by tunneling through the insulating layer, providing that it was suffi ciently thin - the current flows perpendicular to the stack (current perpendicualr to plane, CPP). The spin of tunneling carriers is preserved. If the two magnetic electrodes were half-metals, current would only flow if they were aligned parallel, as only in that case would there be an appropriate density of states available to receive the incoming spin. This tunnel junction structure forms the basis of Magnetic Random Access Memory (MRAM) (figure 1.5).

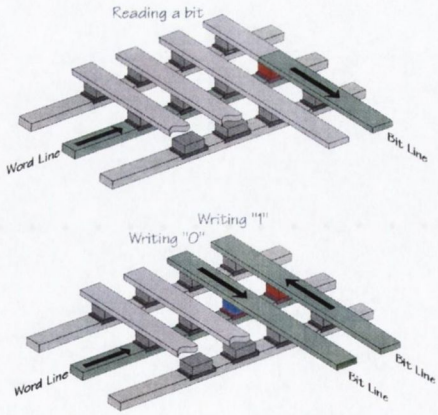


Figure 1.5 Schematic illustration of MRAM

Both spin valves and tunnel junctions are two terminal devices, while three, four and

more terminal devices are expected in the future (analogous to transistors and MOSFETS in conventional electronics). Materials and processing techniques in the semiconductor industry have advanced to such a degree that exceptional levels of material purity and technical precision are possible, providing an opportunity for semiconductor-based devices to be developed, the most novel of which may be quantum information processing hardware for quantum computing.

1.1.3 Materials for spin electronics

Spin polarisation arises naturally in the ferromagnetic elements Fe, Co and Ni. Their crystal structures differ, with the body centred cubic structure (bcc) for Fe, hexagonal close packed (hcp) for Co and face-centred cubic (fcc) for Ni. They have relatively high Curie temperatures of 1044, 1380 and 630 K for Fe, Co and Ni respectively. While Co and Ni are strong ferromagnets, with their $3d^{\uparrow}$ band lying entirely below the Fermi level states, Fe is not, with both $3d^{\uparrow}$ and $3d^{\downarrow}$ states at the Fermi level. The $4s$ bands are partially spin split by exchange with the 3d core states and so complete spin polarisation of these conduction electrons, which carry most of the current, is not achieved. Fe has the highest spin polarisation of 45 %, followed by Ni at 44 % and Co at 42 % [4]. Alloys of these ferromagnetic elements are commonly used as the metallic electrodes in spin-valves and tunnel junctions, with oxide materials such as Al_2O_3, ZrO_2, $SrTiO_3$, TiO_2 and CeO_2 forming the insulating layers.

Ferromagnetic half-metals have a gap in the density of states at the Fermi level and are a source of fully spin polarised electrons (figure 1.6a and b). Examples include CrO_2, Fe_3O_4, the mixed-valence manganites $(La_{1-x}A_x)MnO_3$; A = Ca, Sr or Ba, $x \sim 0.3$, the double perovskites A_2BBO_6 such as Sr_2FeMoO_6, and the Heusler alloys NiMnSb, PtMnSb

and Co_2MnSi. Although the polarisation is high (P > 90 % at low temperatures), the Curie temperatures of many of these materials are quite low, particularly for the oxides ($T_c \sim$ 400 K), with the exception of magnetite, where $T_c \sim 860$ K. The spin polarisation falls off rapidly with increasing temperature.

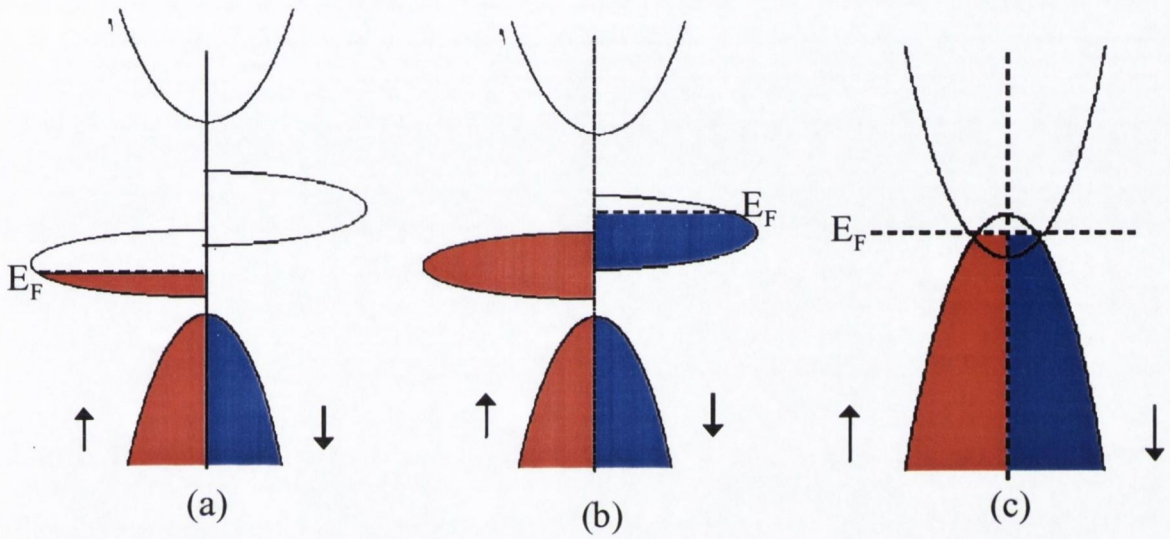


Figure 1.6 Schematic density of states for a half-metallic ferromagnet with (a) only ↑ electrons or (b) only ↓ electrons at the Fermi level and (c) the schematic band structure of a semimetal

The Curie temperature and mobility of some potential spin-electronics materials are listed in Table 2. Semiconductors and semimetals have the highest mobilities (μ), in addition to large spin diffusion lengths (Table 1), but are not ferromagnetic, while the ferromagnetic metals have low spin diffusion lengths and mobility due to strong scattering, as do half-metals. The band structure of a semimetal is shown in figure 1.6c, where there is a small overlap between the valence and conduction bands. Graphite, bismuth and antimony are semimetals, while $Tl_2Mn_2O_7$ is the only known ferromagnetic semimetal. Others may be discovered by doping with magnetic impurities.

		T_c (K)	μ ($cm^2V^{-1}s^{-1}$)
Semiconductors	Si	-	1400
	InSb	-	30000
	GaAs	-	8000
	(Ga,Mn)As	170	
Semimetals	Graphite	-	2000
	Bi	-	180000
Metals	Cu	-	44
	Au	-	48
	Fe	1044	20
	Co	1380	12
	Ni	630	16
Half-metals	CrO_2	390	1.4
	Fe_3O_4	860	0.2

Table 2.Curie temperature (Tc) and mobility values of a variety of semiconductor, semimetal, metal and half-metal materials

Effi cient spin-electronics devices will need materials with high spin-polarisation, high mobility and large spin diffusion lengths. While devices made from Si and GaAs form the basis of semiconductor technology, no "ideal" material has yet been identified for spin-electronics applications. Novel materials include ferromagnetic semiconductors and the half-metallic oxides with high Curie temperatures. Ferromagnetic semiconductors do exist, with EuX; X = O, S, B_6 and the chalcogenide spinels $CdCr_2X_4$; X = S, Se extensively studied in the late 1960s and early 1970s. Semiconductors can also be made ferromagnetic by doping with magnetic ions, such as Mn-doped GaAs which has been extensively studied. Research has also continued into the double perovskites, with substantially higher Curie temperature being reported - 620 K in Sr_2CrReO_6 [5]. Either family of materials could open a new chapter in spin-electronics.

1.1.4 Chapter outline

As described above, new materials are needed for the next generation of spin electronics and the rest of this chapter examines several classes of materials which may be suitable. As

doped semiconductors form a large portion of these some space is first given to describing their basic properties and is followed by descriptions of traditional II-VI, III-V and group IV materials. Oxide semiconductors are briefly introduced, as they will be discussed in much greater detail in later chapters, followed by a short description of unusual results in some perovskite materials and then a summary of experiments to date to control spin in semiconductors.

A section on more novel materials follows, describing reports that carbon may be ferromagnetic, that high-k dielectrics can be doped to produce ferromagnetic insulators and that the alkaline earth hexaborides may also be intrinsically ferromagnetic and semiconducting, all of which are interesting not only in terms of fundamental physics, but may also prove useful in the field of spin electronics. The final section of this chapter discusses some potential extrinsic causes of the reported ferromagnetism.

1.2 Semiconductors

A semiconductor is a material whose conductivity lies between that of metals and insulators, or more precisely, which is insulating at low temperatures and conducting at higher temperatures. Insulating materials have a fully occupied valence band and an empty conduction band at T = 0 K (figure 1.7). However, when the temperature is not zero, electrons in the valence band can be thermally excited across the energy gap E_g, into the conduction band. These electrons are free charge carriers capable of conducting electrical current, as are the "holes" left behind in the valence band. The size of the energy gap determines whether appreciable conductivity will occur. The fraction of electrons excited across the gap at temperature T is of the order $\exp(\frac{-E_g}{2k_BT})$ where k_B is Boltzmanns constant.

Materials which are insulators at T = 0 K, but which have an energy gap small enough

to allow electrons to be thermally excited to the conduction band at higher temperatures are semiconductors. Their room temperature resistivity lies in the range 10^{-3} - 10^{9} Ωcm, greater than that of metals ($\sim 10^{-6}$ Ωcm) and less than insulators ($\sim 10^{22}$ Ωcm). As the fraction of electrons excited into the conduction band of a semiconductor varies exponentially with 1/T, the conductivity increases with increasing temperature - unlike metals, where the conductivity decreases with increasing temperature.

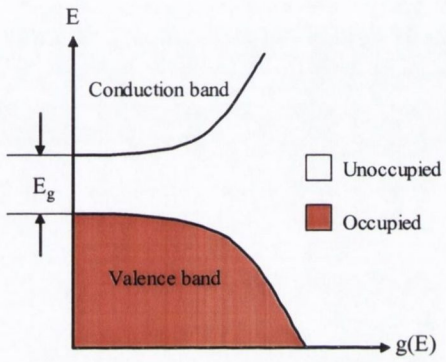


Figure 1.7 Band structure of an insulator

Pure semiconductors, in which electrons and holes formed by thermal excitation dominate the electronic properties - are called *intrinsic semiconductors.* Electrons can also absorb energy from other sources - lattice vibrations, photons - also forming electron-hole pairs and contributing to the conductivity. In equilibrium the number of holes per unit volume (p) equals that of electrons per unit volume (n), and the intrinsic carrier density n_i is given by

$$np = n_i^2 \tag{1.5}$$

In *extrinsic semiconductors* the electronic properties are determined by the electrons/holes contributed by impurity atoms. n-type doping occurs if the impurity atom, known as a donor atom, contributes electrons - for example N or P in Si. In p-type doping an impurity atom contributes holes to the host material and is an acceptor atom - for example Al or Ga in

Si. Donor atoms have a higher valence than that of the component they substitute, and introduce additional electronic levels (E_D) just below the bottom of the conduction band. Acceptor atoms have a lower valence and form an energy level (E_A) just above the top of the valence band (figure 1.8).

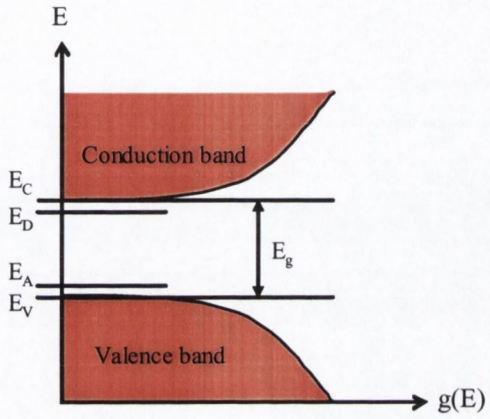


Figure 1.8 Energy levels in a doped semiconductor

A semiconductor has a direct band-gap when the maximum of the valence band occurs at the same location in k-space as the minimum of the conduction band, and indirect if it does not (figure 1.9). For indirect transitions to occur, a phonon must also participate.

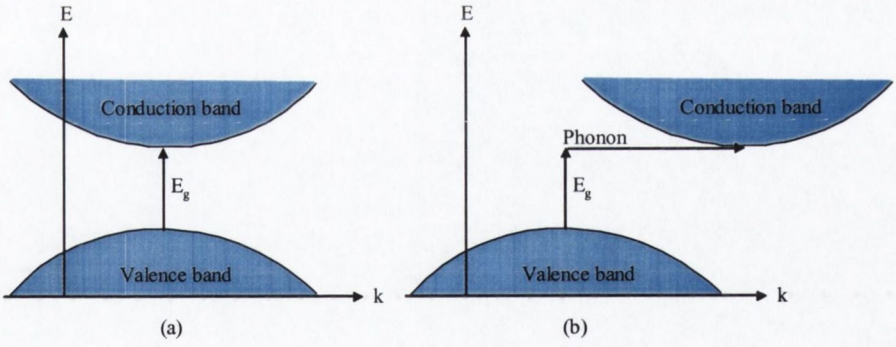


Figure 1.9 Direct (a) and indirect (b) band gap transitions in a semiconductor

1.2.1 Dilute magnetic semiconductors

Dilute magnetic semiconductors are produced by doping non-magnetic semiconductors

with magnetic ions to make them ferromagnetic (figure 1.10). The valence of the dopant atom can match that of the atom it's replacing, or can differ, introducing electrons or holes to the host lattice.

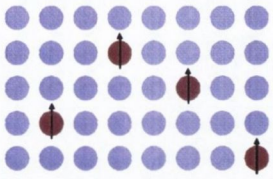


Figure 1.10 Schematic illustration of a dilute magnetic semiconductor - with dopant atoms sitting in sites in the semiconductor lattice and creating magnetic moments (illustrated by arrows)

The concentration of dopant atoms introduced will be limited by their solubility limit in the lattice - a homogeneous distribution of atoms is required, with no clustering of the dopant atoms. When a semiconductor becomes ferromagnetic the conduction band, valence band or impurity band can become spin-split [6] due to exchange interactions. The schematic band structure of an oxide with $3d$ impurities and a spin-split impurity band is shown in figure 1.11 for low and high Curie temperatures.

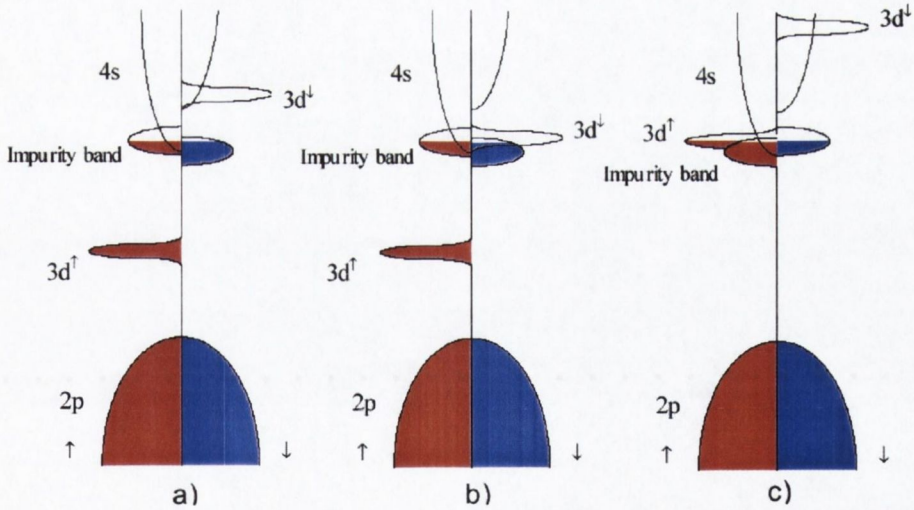


Figure 1.11 Schematic band structure of an oxide with $3d$ impurities and a spin-split impurity band - (a) and (b) show the positions of the minority spin $3d$ bands for low and high T_c respectively and (c) shows the position of the majority spin band for high T_c

Research into dilute magnetic semiconductors was initially based on doped II-VI ma-

terials, then moved into III-V semiconductors and now also encompasses the elemental semiconductors, oxide and nitride materials and the alkaline-earth hexaborides.

1.2.2 II-VI semiconductors

Studies of doped II-VI semiconductors have focused on the Mn doped alloys, $II_{1-x}Mn_xVI$, where the valence of the cation matches that of manganese. These materials crystallise in the cubic zinc-blende, or hexagonal wurtzite structures and can accomodate large amounts of Mn in the lattice - up to $x = 0.86$ for $Zn_{1-x}Mn_xTe$ - while still maintaining the parent ZnTe zinc blende structure. They are direct band gap materials, with the cadmium and zinc chalcogenides being wide gap, and the mercury materials narrow gap. As the Mn concentration is increased, the band gap also increases, and so can be tuned. Large Zeeman splitting occurs at the band edge in $II_{1-x}Mn_xVI$ materials due to $sp-d$ exchange interaction between the Mn^{2+} ions and the s and p band electrons, leading to a large Faraday effect and negative magnetoresistance. Figure 1.12 illustrates a typical magnetic phase diagram for $Zn_{1-x}Mn_xTe$, although this is similar for all $II_{1-x}Mn_xVI$ dilute magnetic semiconductors, excluding the antiferromagnetic region which only appears with high Mn solubility.

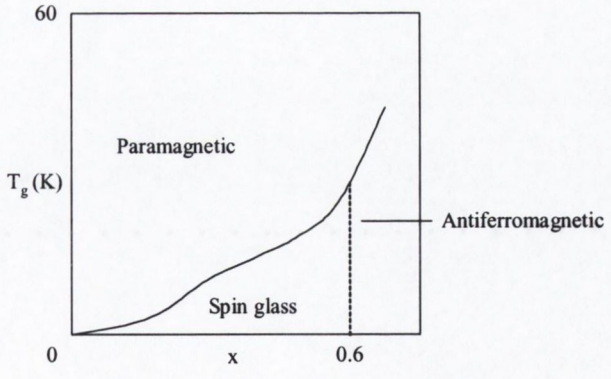


Figure 1.12 Magnetic phase diagram for $Zn_{1-x}Mn_xTe$

In the dilute limit, where $x < 0.01$, the Mn ions are effectively isolated and the material

behaves as a paramagnet. At higher values of x the Mn ions are no longer isolated and couple through an antiferromagnetic exchange interaction. The low temperature phase is macroscopically disordered, and displays many characteristics of a spin glass state, although whether it is a true spin-glass state remains unresolved. Ferromagnetism in $p-$type IIMnVI materials has been predicted (figure 1.13) [7] and observed in (Zn,Mn)Te ($x = 0.019$) [8] at very low temperatures (< 2 K).

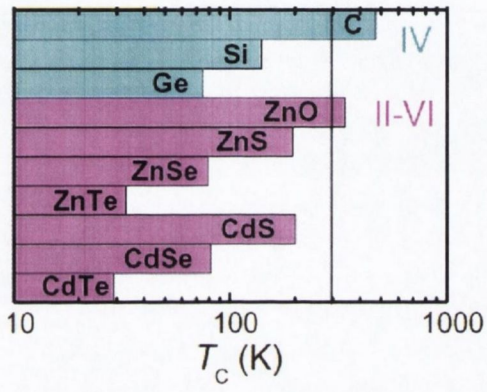


Figure 1.13 Predicted Curie temperature values for $p-$ type II-VI and group IV materials doped with 5 at. % Mn [7]

However, a much higher Curie temperature has now been found in $n-$type $Zn_{1-x}Cr_xTe$ [9], with ferromagnetism persisting up to room temperature when $x = 0.20$ (figure 1.14), following a prediction that superexchange in Cr and V based II-VI compounds can lead to ferromagnetic order [10]. Zn is divalent, but Cr is trivalent (electron doping).

Thin films of doped II-VI materials are grown by pulsed laser deposition (PLD) and molecular beam epitaxy (MBE). Typically, GaAs substrates are used. Although recent work has shown that room temperature ferromagnetic II-VI dilute magnetic semiconductors are achievable, the usefulness of these materials is limited by the fact that it is diffi cult to dope them $n-$ and $p-$type and control the carrier concentration, which is necessary for spin electronics devices.

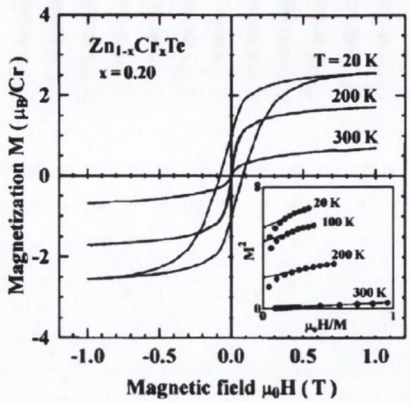


Figure 1.14 Magnetisation curves of a $Zn_{0.80}Cr_{0.20}Te$ film at 20, 200 and 300 K, with the inset showing the Arrott plots of the magnetisation data [9]

1.2.3 III-V semiconductors

III-V semiconductors such as GaAs are quite widely used for high speed electronic and optoelectronic devices, and so are natural candidates for doping to produce magnetic semiconductors. The major obstacle in making III-V semiconductors magnetic has been that the solubility of magnetic ions is quite low in these compounds. This was overcome by depositing films by molecular beam epitaxy, at conditions far from equilibrium. This led to the discovery of partial ferromagnetic order in (In,Mn)As [11] with Curie temperatures of $\sim$ 35 K [12][13], and ferromagnetic (Ga,Mn)As [14], with a Curie temperature of up to 172 K [15]. These materials have the zinc blende structure, and are $p-$type as Ga (or In) is trivalent, while Mn is divalent - and so they are a source of spin-polarised holes rather than polarised electrons.

In 2000, Dietl et al [16] proposed a model to explain the ferromagnetism in (Ga,Mn)As, and extended it to other materials, predicting Curie temperatures above room temperature for GaN and InN doped with 5 at. % of Mn (figure 1.15 (a, b)). Sato and Katayama-Yoshida have predicted the stability of ferromagnetic states in transition-metal doped GaN (figure

1.16a) [19], suggesting that V, Cr and high concentrations of Mn dopants should produce ferromagnetic ordering, while Fe, Co and Ni doping will lead to a spin-glass state.

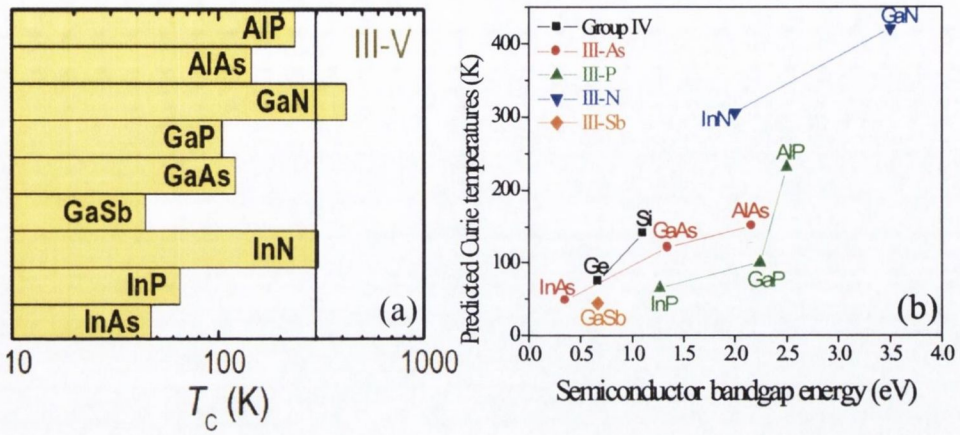


Figure 1.15 (a) The predicted Curie temperature values for $p-$ type III-V materials doped with 5 at. % Mn from Dietl et al [16] and (b) predicted Curie temperature values from (a) plotted as a function of bandgap energy

Room temperature ferromagnetism has since been reported in (Ga,Mn)N, with 9 at. % Mn grown by MBE by Sonoda et al [20], with a Curie temperature of 940 K (figure 1.16b). Table 3 summarises the results acheived for doped III-V materials.

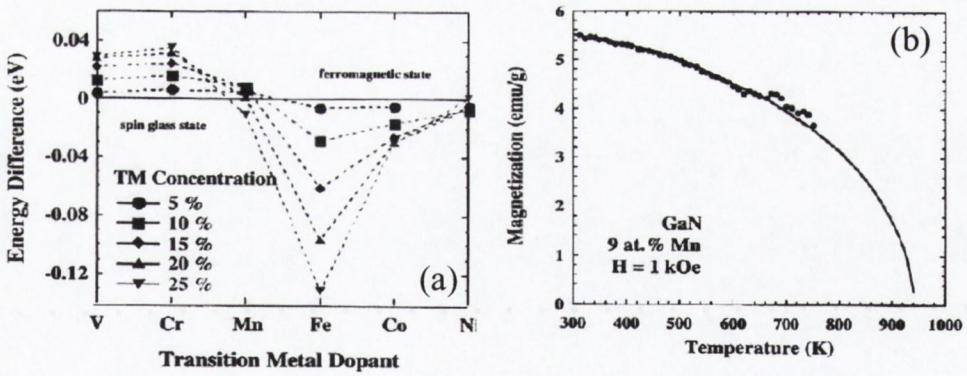


Figure 1.16 (a) The predicted stability of ferromagnetic states in transition metal doped GaN as a function of concentration. The vertical axis shows the energy difference between the ferromagnetic and spin-glass states for each metal atom [19] and (b) magnetisation versus temperature for a (Ga,Mn)N film grown by MBE with $\sim$ 9 at. % Mn. The extrapolation of the curve is based on a mean-field approximation [20]

Although there are few reports of ferromagnetism above room temperature in doped

III-V materials, it is hoped that new growth techniques and post-deposition annealing treatments will lead to high quality films with consistent and reproducible room temperature ferromagnetism.

Material	Curie temperature (K)	Reference
(In,Mn)As	30	H. Ohno (1992) [11]
(Ga,Mn)As	172	Nazmul et al (2003) [15]
(Ga,Mn)N	940	S. Sonoda et al, (2002) [20]
(Ga,Cr)N	> 400	M. Hashimoto et al, (2002) [21]
(Ga,Mn)Sb	25	Matsukura et al, (2000) [22]
(Ga,Mn)P	270	N. Theodoropoulou et al, (2002) [23]
(Ga,Mn)P:C	> 330	M. E. Overberg et al, (2002) [24]
(In,Mn)Sb	8.5	T. Wojtowicz et al, (2004) [25]
(Al,Cr)N	> 900	Kumar et al, (2004) [26]

Table 3.Reported Curie temperature values for doped III-V materials

1.2.4 Oxide magnetic semiconductors

Ferromagnetic oxides are commonly transparent and suitable for a wide variety of applications in UV photonics and transparent electronics. Most semiconducting oxides are intrinsically $n-$type - Cu_2O is the only known binary $p-$type semiconducting oxide, due to copper vacancies that introduce an acceptor level ~ 0.5 eV above the valence band. Following the initial report by Matsumoto et al [27] of ferromagnetism in cobalt-doped anatase TiO_2 (figure 1.17a and b), magnetic moments have been reported in several oxide semiconductor systems. Dietl et al [16] predicted that $p-$type ZnO doped with 5 at. % Mn should be ferromagnetic at room temperature (figure 1.13), while Sato and Katayama-Yoshida [28] have suggested that V, Cr, Fe, Co and Ni dopants should also produce ferromagnetic ordering. Table 4 summarises the initial reports of ferromagnetism in TiO_2, SnO_2, ZnO, Cu_2O and perovskite materials. Ogale et al [29] recently reported high temperature ferromagnetism in tetragonal SnO_2 doped with Co, with a giant magnetic moment of 7.5 μ_B/Co and a Curie

temperature of 650 K (figure 1.17c and d).

Room temperature ferromagnetism has also been reported in the conducting doped oxide perovskites. $BaTiO_3$, $SrTiO_3$ and $KTaO_3$ single crystals implanted with 3 - 5 at. % Mn or Co display Curie temperatures greater than 300 K [32], while moments of up to 1 μ_B/Co have been measured in Co-doped $La_xSr_{1-x}TiO_3$ thin films, with Curie temperatures up to 450 K [33].

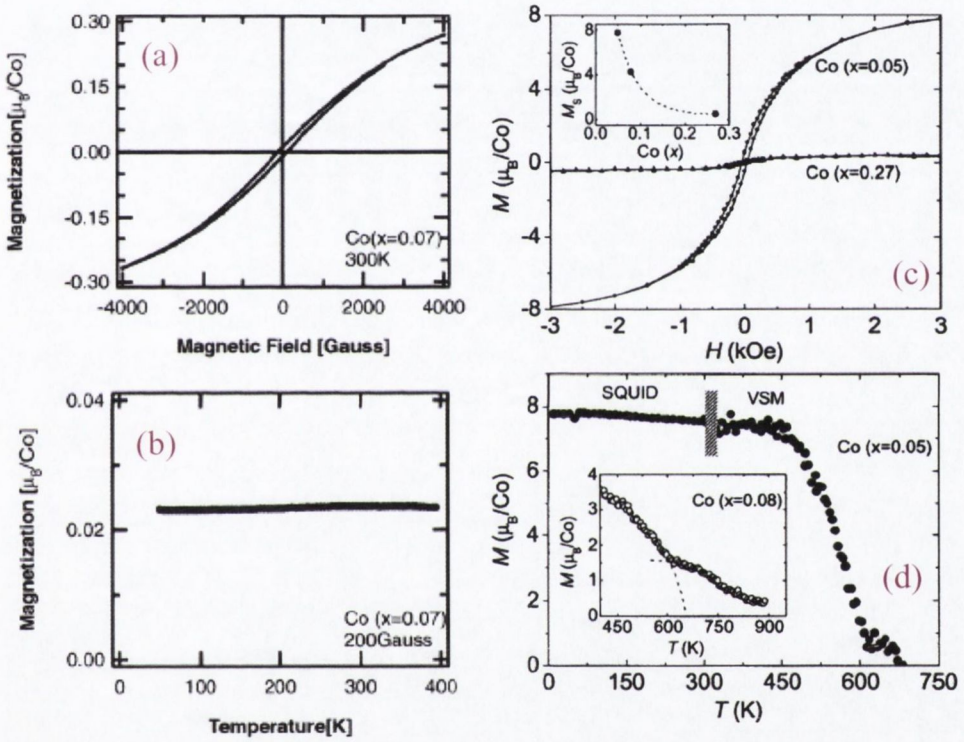


Figure 1.17 Magnetisation curve (a) and temperature dependence of magnetisation (b) of $Ti_{0.93}Co_{0.07}O_2$ thin films [27], (c) the magnetic hysteresis loops for $Sn_{1-x}Co_xO_{2-\delta}$ thin films, where $x = 0.05, 0.27$ at 300 K. The inset shows the dependence of saturation moment, M_s, on Co concentration, x and (d) magnetisation as a function of temperature for a thin film with $x = 0.05$, indicating a Curie temperature of $\sim$ 650 K. The inset show a similar figure for a film with $x = 0.08$ [29].

A remarkable prediction appears in the local density approximation (LDA) calculation by Elfimov et al [34] for CaO with 3 % of Ca vacancies. There are no magnetic cations present, yet they suggest the oxide orders ferromagnetically and has a half-metallic ground

state. A similar prediction was made by Monnier and Delley for CaB_6 with B_6 vacancies [35]. These calculations are based on the idea that two electrons or holes in the defect may have a spin triplet ground state.

	x (at. %), dopant	Moment (μ_B/dopant)	T_C (K)	Reference
TiO_2	1 -2 %, Co	0.3	> 300	Y. Matsumoto et al, (2001) [27]
SnO_2	5 %, Co	7.5	650	S.B. Ogale et al, (2003) [29]
ZnO	5 -15 %, Co	2, x = 10 %	280 -300	K. Ueda et al, (2001) [30]
Cu_2O	5 % Co, 0.5 % Al	0.45 (4.2 K)	> 300	Kale et al, (2003) [31]
$BaTiO_3$	3 - 5 %, Mn or Co	-	$\sim$ 300	Lee et al, (2003) [32]
$SrTiO_3$	3 % Mn, 3 - 5 % Co	-	$\sim$ 300	Lee et al, (2003) [32]
$KTaO_3$	3 - 5 %, Mn or Co	-	$\sim$ 250	Lee et al, (2003) [32]
$La_{1-x}Sr_xTiO_3$	x = 0.5, 7 %, Co	1.0	$\sim$ 450	Zhao et al [33]

Table 4.Initial reports of ferromagnetic oxide semiconductor systems

There are great prospects for transparent, ferromagnetic oxides to develop the future of spin electronics. While there has been extensive research in this area many questions still remain unanswered - how did the giant magnetic moment, in excess of the spin-only moment, arise in Co-doped SnO_2 [29]? What type of ferromagnetic exchange coupling exists in these oxides? Further experiments, with careful analysis, are needed to clarify the situation to determine whether or not oxide dilute magnetic semiconductors can reasonably be used in spin electronic devices.

1.2.5 Group IV based magnetic semiconductors

The simple semiconducting elements are from Group IV of the periodic table, with Si and Ge being the two most important. Carbon (as diamond) is insulating, while tin (as grey tin) is semiconducting and lead is metallic. A silicon-based magnetic semiconductor could be readily integrated with existing semiconductor technology. Dietl et al predicted ferromagnetism with a Curie temperature of $\sim$ 130 K in Mn doped silicon [16], and a recent

report has shown that Co-doped FeSi, a narrow gap semiconductor, is ferromagnetic, with a Curie temperature of 53 K [36].

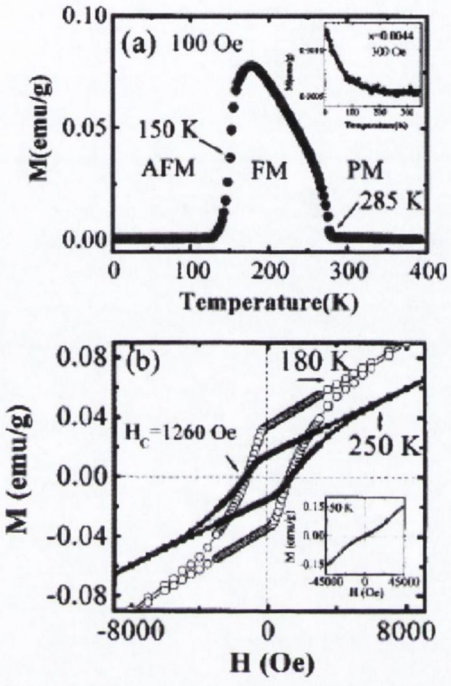


Figure 1.18 (a) Magnetisation as a function of temperature of a $Ge_{0.94}Mn_{0.06}$ sample in a 100 Oe field. The inset shows paramagnetic ordering for a sample with $x = 0.0044$ (b) M-H curves for a $Ge_{0.94}Mn_{0.06}$ single crystal at 180 and 250 K. The inset shows the M-H curve at 50 K [39].

Ferromagnetism with a Curie temperature of $\sim$ 75 K has been predicted in manganese doped germanium [16], and has been experimentally discovered at low temperatures ($<$ 130 K) in insulating Mn-doped Ge thin films [37], and Cr-doped germanium crystals [38] with low dopant concentrations. Curie temperatures up to 285 K have been reported (figure 1.18) [39], while Tsui et al [40] reported that high quality, epitaxial Co and Mn-doped Ge thin films are ferromagnetic with a maximum Curie temperature of 270 K for $Co_{0.12}Mn_{0.03}Ge_{0.85}$, and an average moment of 0.3 μ_B per dopant atom (film concentration was according to $(Co_{ax}Mn_{bx}Ge_{1-x})$). The results are summarised in Table 5.

Dopant	x (at. %)	T_c (K)	μ_B/dopant at 5 K	Reference
Mn	0.6 - 3.5	116 ($x = 3.5$ %)	~ 1.9 ($x = 2$ %)	Park et al [37]
Cr	1	126	0.83	Choi et al [38]
Mn	0.44 - 6.2	285 ($x = 6$ %)	-	Cho et al [39]
Co, Mn	12, 3	270	0.3 (a = 0.7, b = 0.03, $x \sim 8$ %)	Tsui et al [40]
Cr	1	126	0.83	Choi et al [41]
Fe	5	233	-	Choi et al [41]

Table 5.Reported magnetic moments and Curie temperature values for doped Ge, where x is the dopant concentration

1.2.6 Semiconductor spin electronics

Several approaches have been taken to combine semiconductor technology with spin electronics. Malajovich et al [42] have shown that spins can be coherently and effi ciently transferred across an interface between different semiconductor materials by applying an electric field. When E = 0 only a short burst of spins cross the interface from GaAs to ZnSe, where they precess in the opposite direction and decay at a rate characteristic of ZnSe (figure 1.19). When E > 0 spins are "dragged" across the interface, and initially carry information about spin precession in GaAs, but lose that information with time. A spin current is developed due to the continous arrivals of new spins from the GaAs.

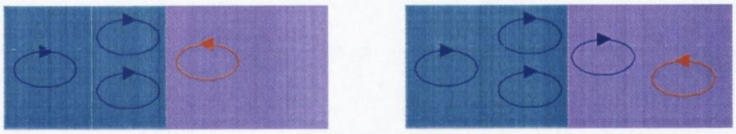


Figure 1.19 (a) Spins transferred from GaAs (blue) to ZnSe (purple) in the presence of a magnetic field but no electric field precess in the opposite direction and decay at a rate characteristic of ZnSe while (b) in the presence of an electric field they initially retain information about spin precession in GaAs which they lose with time, but a spin current can be established with new spins arriving from the GaAs [42]

Direct injection of spin-polarised carriers into semiconductors through a ferromagnetic electrode has proven disappointing, with the spin transport effects reported typically of order a few percent [43][44]. This is likely to be due to ineffi cient transfer at the

metal/semiconductor interface, which is highly diffusive, leading to scattering.

Kato et al [45] have used the relativistic properties of electrons to manipulate their spin. An electron moving through a solid perceives a magnetic field from the atomic electron fields, causing it to precess. By applying a voltage across a layer of GaAs, which was grown on AlGaAs to introduce strain to the layer, they forced the spin-polarised electrons to move with constant velocity. A current flow was established, which is needed to obtain a preferred rotation axis, and they were able to rotate the spins through a turn and a half within 60 μm of GaAs, without a magnetic field.

The most interesting approach of all, however, may be the development of ferromagnetic semiconductors. Successful spin injection from a magnetic semiconductor into a non-magnetic semiconductor has been reported by Ohno et al [46] in the heterostructure device illustrated in figure 1.20. Under forward bias spin-polarised holes from GaMnAs and unpolarised electrons from the n-type GaAs substrate are injected into the InGaAs quantum well, through a space layer of thickness d, producing polarised electroluminescence. This requires no applied magnetic field but only occurs at low temperatures - below the Curie temperature of GaMnAs.

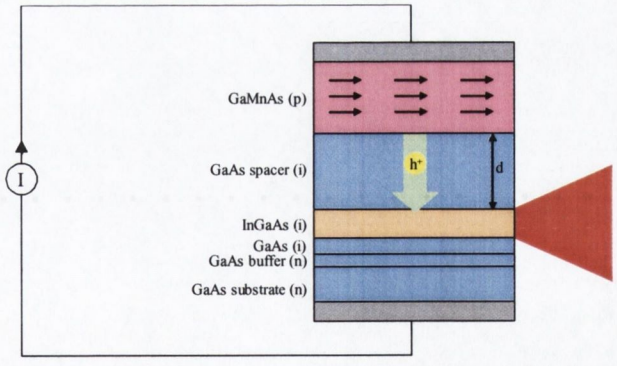


Figure 1.20 The semiconductor heterostructure employed by Ohno et al [46] to demonstrate injection of spin-polarised holes

Ferromagnetic, transparent, semiconducting materials are of interest in themselves

with a multitude of potential applications. The main stumbling block has been achieving Curie temperatures above room temperature, but if this can be overcome, ferromagnetic semiconductors should have a big effect on the future of spin electronics.

1.3 Other novel materials

1.3.1 Carbon-based ferromagnets

In addition to predicting ferromagnetism in II-VI, III-V and oxide materials, Dietl et al [16] suggested that diamond, a wide-gap semiconductor with $E_g = 5.4$ eV, should become a ferromagnet with a high Curie temperature, $T_c \sim 480$ K when doped with 5 at. % Mn (figure 1.13). However, there have been many reports that undoped carbon is ferromagnetic. Ferromagnetism in organic materials was first predicted in the 1960s [47][48], and there have since been a number of reports of weak magnetic moments in carbon determined experimentally, as summarised in Table 6.

Form	σ_s (Am^2kg^{-1})	μ_B/C	T_c K	Reference
Rh-C_{60}	0.09 (RT)	0.0002	$\sim$ 500	T. L. Makarova et al, (2001) [49]
HOPG	0.003 (RT)	0.000006	$>$ 500	P. Esquinazi et al, (2002) [50]
Pyrolysed carbon	36.2 (4.5 K)	0.072		K. Murata et al, (1996) [51]
Graphite-sulphur system	0.02	0.00004		S. Moehlecke et al, (2002) [52]
C/Fe multilayer		0.05		H. Mertins et al, (2004) [53]

Table 6.Summary of reported ferromagnetism in carbon materials, where RT indicates room temperature moments

Ferromagnetism in rhombehdral C_{60} [49] (figure 1.21) produced by a high pressure and high temperature process was discovered accidentally while searching for superconductivity. The material produced exhibited features typical of ferromagnets - saturation magnetisation, hysteresis and it was reported that it could attach to a magnet at room temperature - despite the very small moment of 0.0002 μ_B/C.

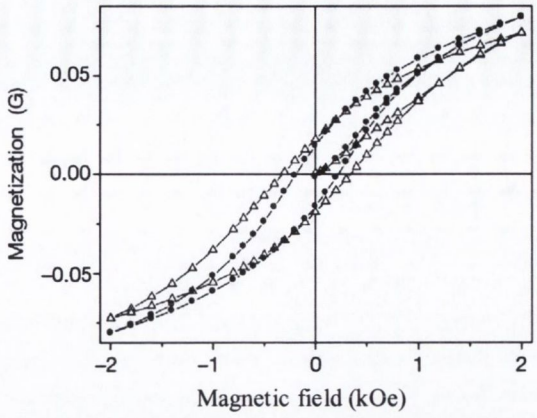


Figure 1.21 Magnetisation hysteresis loops for Rh-C_{60} at room temperature [49]

Ferromagnetism has also been reported in highly oriented pyrolitic graphite, with room temperature saturation magnetisation of 0.003 Am^2kg^{-1} [50], and ferromagnetic hysteresis loops up to 800 K [54]. This material is similar to rhombohedral C_{60}, but with graphene layers instead of spheres of covalently bonded C_{60} molecules.

Amorphous carbon prepared by direct pyrolysis of organic compounds has displayed moments of up to 0.072 μ_B/C [51], depending on the precursor and preparation temperature, as summarised in Table 7. Pyrolitic carbon is highly oriented in structure, and contains a large number of unpaired electrons in the graphite skeleton, which may lead to a spin exchange interactions.

Author	**Precursor**	**Temp (K)**	**Environment**	σ_s **(Am^2kg^{-1})**	μ_B**/C**
Murata et al	Triethylborane	1083	Vacuum	36.2 at 4.5 K	0.0721
Murata et al	Cyclododecane	1223	Vacuum	1.07 at 4.3 K	0.0023
Murata et al	1,2-diaminopropane	1223	Vacuum	10.5 at 4.3 K	0.0225
Kawabata et al	Adamantane	1273	Ar	0.5 at 10 K	0.0011
Katulevskii et al	Phenyldiamine+melamine	873	Vacuum	0.624	0.0013
Araki et al	Guanine	873	Vacuum	0.624	0.0013
Araki et al	TPTA+melamine	873	Vacuum	0.3 at RT	0.0006
Araki et al	TPTA+melamine	1223	Ar + dry air	10.4	0.0224

Table 7.Reported results from pyrolysis experiments

Contact-induced ferromagnetism has been reported for carbon nanotubes on a cobalt or magnetite substrate [55], with a moment of order 0.1 μ_B per contact carbon atom (figure 1.22), while Kletetschka et al [56] found evidence of ferromagnetism in carbonados (polycrystalline diamonds), but concluded that it was mostly associated with surface and open pores, rather than the bulk material.

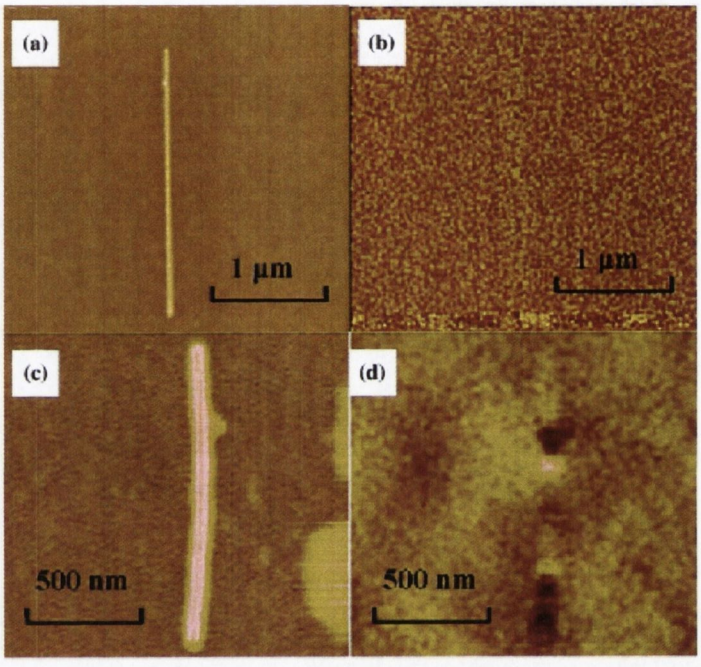


Figure 1.22 (a) Atomic force micrograph (AFM) of a multi-walled carbon nanotube on Si substrate and (b) the corresponding magnetic force micrograph (MFM), (c) is an AFM image of another tube on a Co substrate, and (d) is the corresponding MFM image, where some magnetic contrast is visible [55].

Ferromagnetism with $\sigma_s = 0.02$ $\mathrm{Am^2kg^{-1}}$ has been reported to co-exist with superconductivity in the graphite-sulphur system [52], in line with a theoretical prediction [54] that magnetic and superconducting correlations in graphite may occur. There are also theoretical reports that graphene sheets a few nanometers in width show an unusual density of states, which lead to local moments at the strip edges which are paramagnetic [57], or, with a suitable stacking, antiferromagnetic [58]. There is also a prediction of a ferromagnetic instability

in graphene sheets [59].

Ferromagnetic carbon is certainly a novel idea, but the wealth of reports suggesting that it exists cannot be ignored. However, the weakness and variability of reported moments, in addition to doubts as to the purity of the samples, must be considered.

1.3.2 High-k dielectrics - hafnium dioxide

Hafnium dioxide is a wide band-gap (5.68 eV), insulating material with a high static dielectric constant (ϵ = 23 - 25). It exists in three polymorphs at atmospheric pressure - a low temperature monoclinic phase, a tetragonal phase above 2000 K and a cubic phase above 2870 K. The cubic polymorph can be stabilised at room temperature by the incorporation of suitable metal cations (Ca^{2+}, Y^{3+}, Gd^{3+}) [60]. Recent interest in HfO_2 has stemmed from the suggestion that it could replace SiO_2 as the gate dielectric in complementary metal-oxide semiconductor (CMOS) devices [61].

Rao et al [62] have reported that monoclinic Co-doped HfO_2 thin films have a giant magnetic moment of 6.8 μ_B/Co and a Curie temperature $\sim$ 880 K (figure 1.23). The thin films are deposited by pulsed laser deposition (PLD) at 700 °C on yttria stabilised zirconia (YSZ) substrates in an oxygen atmosphere. The optimum oxygen partial pressure was found to be 1 x 10^{-4} Torr, with reduced moments found in films made at higher or lower pressures. The films were transparent in the ultra violet/visible range of wavelengths (transmission, T, is $\sim$ 65 %), and cobalt-doped samples had a dielectric constant of 18. Coercivity of 5.2 mT was found at room temperature, and cobalt was found to be in the Co^{2+} valence state from electron energy loss spectroscopy (EELS). The films have c-axis orientation and are tilted by about $\sim$ 9.1° with respect to the (001) axis of the substrate (figure 1.23c). The bulk sample had a small moment of 0.055 μ_B/Co.

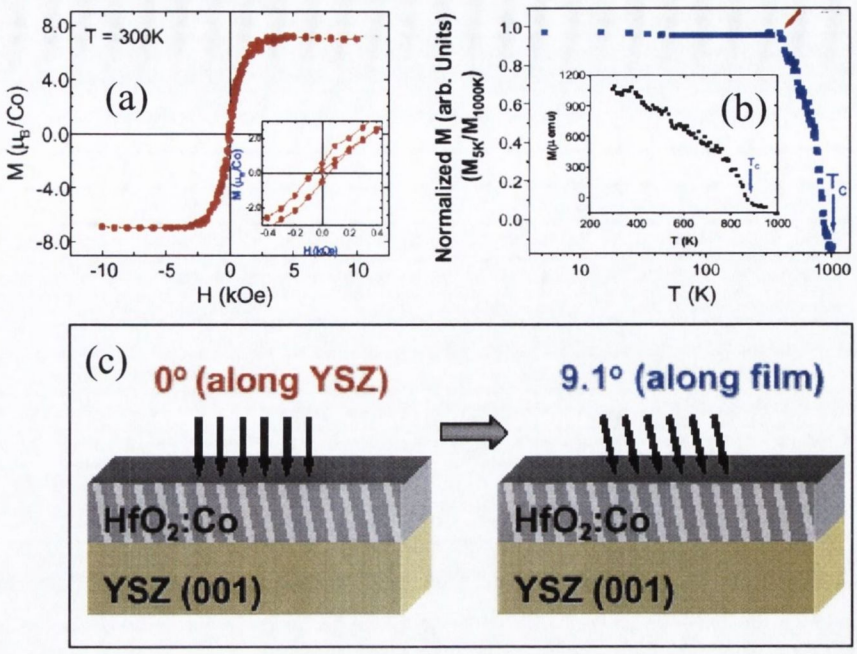


Figure 1.23 (a) M vs H curve for a $Hf_{0.95}Co_{0.05}O_2$ thin film at room temperature, with an inset illustrating the coercivity of the sample, (b) magnetisation as a function of temperature (with $T_c \sim 880$ K) and (c) the c-axis of the films are tilted by 9.1 ° relative to the substrate [62].

The Eu-chalcogenides EuO and EuS are known ferromagnetic insulators (with Curie temperatures of 69 K and 16 K respectively) [63]. They are quite uncommon in general, with spins tending to order antiferromagnetically in insulating solids. It has been suggested that the spin-filter effect from an insulating ferromagnetic tunnel barrier may form the basis of quantum computation in solid state devices [64], and EuS is a candidate material as the spin filter effect in EuS layers was demonstrated in 1967 by Esaki et al [65].

1.3.3 Calcium, Strontium, Barium and Europium hexaborides

The alkaline-earth hexaboride, AB_6, has the CsCl crystal form, with divalent alkaline earth ions and B_6 clusters, and is a semimetal [66]. Hexaborides tend to be boron rich, with metal vacancies. Band calculations [67] and experimental results [68] suggest that CaB_6 is a semiconductor, and so appealing as a future spin-electronics material. Ferromagnetism with

$T_c \sim 600$ K has been reported in $A_{1-x}La_xB_6$ for A = Ca, Sr and Ba, with a maximum moment of 0.07 μ_B/La for $x = 0.005$ [69], although a later study finds that this ferromagnetism is not intrinsic, and likely the result of Fe impurities [70].

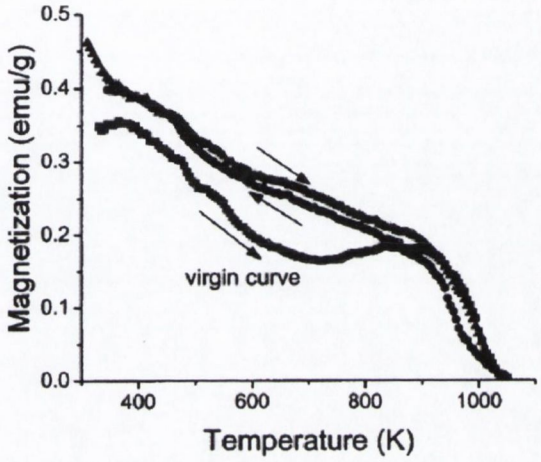


Figure 1.24 The magnetisation curve of CaB_6 in air. The "virgin" curve shows an unexpected increase in magnetisation at $\sim$ 750 K, and a Curie temperature of about 1000 K [71]

Lofland et al [71] found that pure CaB_6 has a Curie temperature of 900 K and a moment of ~ 0.01 μ_B/f.u. This can be increased by heating the samples in air, introducing defects, leading to a T_c of more than 1000 K and increasing the moment by more than 20 % (figure 1.24). It has also been reported that Ca deficient CaB_6 is ferromagnetic up to room temperature, while Ca-rich CaB_6 is not [72], indicating that Ca vacancies are responsible for the ferromagnetism (nominally pure SrB_6 has also been reported to be ferromagnetic [73]). But again, others reports that there is an extrinsic origin of the ferromagnetism in the undoped samples [68]. Theoretical calculations suggest that B_6 vacancies, and not metal vacancies, will lead to ferromagnetism, with a moment of 2.4 μ_B/vacancy [35]. EuB_6 has been reported to order ferromagnetically at 15 K, and may be a half-metallic semimetal [74].

1.4 Impurity phases

In most of the dilute magnetic semiconductors and novel magnetic materials discussed above the reported moments vary greatly with sample preparation and handling, are diffi cult to reproduce, and frequently decrease, or disappear altogether, with time. Controversy surrounds whether or not the ferromagnetic signal is intrinsic to the material, or simply the result of magnetic impurities. Ferromagnetism detected in Co-doped TiO_2 is suspected to come from Co clusters [75], Fe impurities have been shown to be responsible for magnetism in La-doped CaB_6 [70], while the giant magnetic moment observed in Co-doped SnO_2 [29] was found to decrease after high temperature magnetisation measurements and as a function of time [62]. Trace amounts of Fe could explain the magnetic moments measured in most samples - the cosmic abundance of iron is seventeen times that of all the other magnetic elements taken together - and so is diffi cult to eliminate entirely. High resolution elemental analysis and imaging is needed, in addition to demonstrating that the magnetic properties (such as coercivity and Curie temperature) of the samples differs from those of the likely impurity or secondary phases. Reliable, reproducible, intrinsically ferromagnetic materials are needed.

Table 8 lists some of the potential secondary phases, along with their magnetic properties.

Group	Phase	Nature of magnetism	Curie temp. (K)	Néel temp. (K)
Common to all	Cr	Antiferromagnetic		311
	Mn	Antiferromagnetic		100
	Fe	Ferromagnetic	1040	
	Co	Ferromagnetic	1382	
	Ni	Ferromagnetic	630	
II-VI	CrTe	Antiferromagnetic		150
	Cr_3Te_4	Antiferromagnetic		80
	MnAs	Ferromagnetic	310	
	MnSb	Ferromagnetic	560	
	MnTe	Antiferromagnetic		307
	$MnTe_2$	Antiferromagnetic		85
	FeTe	Antiferromagnetic		70
	$FeTe_2$	Antiferromagnetic		83
	$ZnCr_2Se_4$	Antiferromagnetic		20
III-V	Mn_2Ga	Ferromagnetic	690	
	Mn_3Ga	Ferromagnetic	743	
	MnGa	Ferromagnetic	> 300	
	Mn_4N	Ferromagnetic	745	
	MnP	Ferromagnetic	291	
	Fe_2Ga	Ferromagnetic	620	
	Fe_3Ga	Ferromagnetic	760	
	Fe_4N	Ferromagnetic	760	
	FeP	Ferromagnetic	215	
	Fe_2P	Ferromagnetic	278	
	Fe_3P	Ferromagnetic	716	
Borides	FeB	Ferromagnetic	598	
	Fe_2B	Ferromagnetic	1015	
Oxides	CrO_2	Ferromagnetic	390	
	Cr_2O_3	Antiferromagnetic		306
	Mn_3O_4	Ferromagnetic	1440	
		Ferrimagnetic	43	
	$\alpha-$ Fe_2O_3	Ferromagnetic	956	
	$\gamma-$ Fe_2O_3	Ferromagnetic	743	
	Fe_3O_4	Ferrimagnetic	860	
	CoO	Antiferromagnetic		280
	NiO	Antiferromagnetic		525
	$SnMn_2O_4$	Ferrimagnetic	53	
	$Zn_{0.3}Mn_{2.7}O_4$	Ferrimagnetic	31	
	$Zn_{0.5}Mn_{2.5}O_4$	Ferrimagnetic	20	

Table 8.Potential secondary phases in doped semiconductors and their magnetic properties - from the American Society of Metals binary phase diagram tables

References

[1] N. F. Mott, Proc. R. Soc., **153** 699 (1936)

[2] M. L. Roukes, Nature, **411** 747 (2001)

[3] M. Julliere, Physics Letters A, **54** 225 (1975)

[4] R. J. Soulen, J. M. Byers, M. S. Osofsky, B. Nadgorny, T. Ambrose, S. F. Chong, P. R. Broussard, C. T. Tanaka, J. S. Moodera, A. Barry and J. M. D. Coey, Science **282** 88 (1998)

[5] H. Asano, N. Kozuka, A. Tsuzuki and M. Matsui, Appl. Phys. Lett., **85** 263 (2004)

[6] J. M. D. Coey and S. Sanvito, J. Phys. D: Appl. Phys., **37** 988 (2004)

[7] T. Dietl, A. Haury and Y. Merle d'Aubigné, Phys. Rev. B **55** R3347 (1997)

[8] D. Ferrand, J .Cibert, A. Wasiela, C.Bourgognon, S. Tatarenko, G. Fishman, T. Andrearczyk, J. Jaroszyński, S. Koleśnik, T. Dietl, B. Barbara and D. Dufeu, Phys. Rev. B **63** 085201 (2001)

[9] H. Saito, V. Zayets, S. Yamagata and K. Ando, Phys. Rev. Lett. **90** 207202 (2003)

[10] J. Blinowski, P. Kacman and J. A. Majewski Phys. Rev. B **53** 9524 (1996); J. Cryst. Growth **159** 972 (1996)

[11] H. Ohno, H. Munekata, T. Penney, S. von Molnár and L. L. Chang, Phys. Rev. Lett. **68** 2664 (1992)

[12] H. Ohno, J. Vac. Science Technol. B **18** 2039 (2000)

[13] H. Ohno, F. Matsukura and Y. Ohno, Jap. Soc. Appl. Phys. Int. **5** 4 (2002)

[14] H. Ohno, A. Shen, F. Matsukura, A. Oiwa, A. Endo, S. Katsumoto and Y. Iye, Appl. Phys. Lett. **69** 363 (1996)

[15] A. M. Nazmul and S. Sugahara, Phys. Rev. B, **67** 241308 (2003)

[16] T. Dietl, H. Ohno, F. Matsukura, J. Cibert and D. Ferrand, Science **287**, 1019 (2000)

[17] S. von Molnár, H. Munekata, H. Ohno and L. L. Chang, J. Magn. Magn. Mater. **93** 356 (1991)

[18] Y. Satoh, N. Inoue, Y. Nishikawa and J. Yoshina, 3rd Symposium on Physics and Application of Spin-Related Phenomena in Semiconductors, Sendai, Japan 1997, 23 - 25

[19] K. Sato and H. Katayama-Yoshida, Jpn. J. Appl. Phys.,**40** L485 (2001)

[20] S. Sonoda, S. Shimizu, T. Sasaki, Y. Yamamoto and H. Hori, J. Cryst. Growth **1358** 237 - 239 (2002)

[21] M. Hashimoto, Y. Z. Zhou, M. Kanamura and H. Asahi, Sol. State Comm. **122** 37 (2002)

[22] Matsukura et al, Jour. Appl. Phys., **87** 6442 (2000).

[23] N. Theodoropoulou et al, PRL, 89, 107203 (2002)

[24] M. E. Overberg et al, Materials Research Society Fall Meeting, Boston, 2001 J. Vac. Sci. Technol. B **20** 969 (2002)

[25] T. Wojtowicz, W. L. Lim, X. Liu, G. Cywinski, M. Kutrowski, L. V. Titova, K. Yee, M. Dobrowolska, J. K. Furdyna, K. M. Yu, W. Walukiewicz, G. B. Kim, M. Cheon, X. Chen, S. M. Wang, H. Luo, I. Vurgaftman and J. R. Meyer, Physica E, **20** 325 (2004)

[26] D. Kumar, J. Antifakos, M. G. Blamire and Z. H. Barber, Appl. Phys. Lett. **84** 5004 (2004)

[27] Y. Matsumoto, M. Murakami, T. Shono, T. Hasegawa, T. Fukumura, M. Kawasaki, P. Ahmet, T. Chikyow, S. Koshihara and H. Koinuma, Science 291, 854 (2001)

[28] K. Sato and H. Katayama-Yoshida, Jpn. J. Appl. Phys., Part 2, **39** L555 (2000)

[29] S.B. Ogale, R.J. Choudhary, J.P. Buban, S.E. Lofland, S.R. Shinde, S.N. Kale, V.N. Kulkarni, J. Higgins, C. Lanci, J.R. Simpson, N.D. Browning, S. Das Sarma, H.D. Drew, R.L. Greene and T. Venkatesan, Phys. Rev. Lett. 91, 077205 (2003)

[30] K. Ueda, H. Tabata and T Kawai, Appl. Phys Lett. 79 988 (2001)

[31] Kale et al, APL, 82, 2100 (2003)

[32] J. S. Lee, Z. G. Khim, Y. D. Park, D. P. Norton, N. A. Theodoropoulou, A. F. Hebard, J. D. Budai, L. A. Boatner, S. J. Pearton and R. G. Wilson, Solid State Elec., **47** 2225 (2003)

[33] Y. G. Zhao, S. B. Ogale, S. E. Lofland, C. Lanci, J. P. Buban, N. D. Browning, S. Das Sarma, A. J. Millis, V. N. Kulkarni, R. Choudhary, R. L. Greene and T. Venkatesan, preprint

[34] I. S. Elfimov, S. Yunoki and G. A. Sawatzky, Phys. Rev. Lett., **89** 216403 (2002)

[35] R. Monnier and B. Delley, Phys. Rev. Lett., **87** 15, 157204 (2001)

[36] N. Manyala, Y. Sidis, J. F. DiTusa, G. Aeppli, D. P. Young and Z. Fisk, Nature Mater., **3** 255 (2004)

[37] Y. D. Park et al, Science, **295** 651 (2002)

[38] S. Choi et al, Appl. Phys. Lett., **81** 3606 (2002)

[39] S. Cho, S. Choi and S. C. Hong, Phys. Rev. B, **66** 033303 (2002)

[40] F. Tsui, L. He, L. Ma, A. Tkachuk, Y. S. Chu, K. Nakajima and T. Chikyow, Phys. Rev. Lett., **91** 17, 177203 (2003)

[41] S. Choi, S. C. Hong, S. Cho, Y. Kim, J. B. Ketterson, C.-U. Jung, K. Rhie, B.-J. Kim

and Y. C. Kim, Jour. Appl. Phys., **93** 10, 7670 (2003)

[42] I. Malajovich, J. J. Berry, N. Samarth, D. D. Awschalom, Nature, **411** 770 (2001)

[43] J. F. Gregg, W. D. Allen, N. Viart, R. Kirschman, C. Sirisathitkul, J. P. Schille, M. Gester, S. M. Thompson, P. Sparks, V. da Costa, K. Ounadjela and M. Skvarla, J. Magn. MAgn. Mater., **1751** (1997)

[44] A. Hirohata, Y. B. Xu, C. M. Guertler and J. A .C. Bland, J. Appl. Phys. **85**, 5804 (1999)

[45] Y. Kato, R. C. Myers, A. C. Gossard and D. D. Awschalom, Nature, **427** 50 (2004)

[46] Y. Ohno, D. K. Young, B. Beschoten, F. MAtsukura, H. Ohno and D. D. Awschalom, Nature **402** 790 (1999)

[47] H. M. McConnell, J. Chem. Phys., **39** 1910 (1963)

[48] N. Mataga, Theoret. Chim. Acta, **10** 372 (1968)

[49] T. L. Makarova et al Nature **413** 716 (2001)

[50] P. Esquinazi, A. Setzer, R. Hohne, C. Semmelhack, Y. Kopelevich, D. Spemann, T. Butz, B. Kohlstrunk, M. Losche, Phys. Rev. B, **66** 024429 (2002)

[51] K. Murata and H. Ushijima, J. Appl. Phys., **79** 978 (1996)

[52] S. Moehlecke, P. C. Ho, M. B. Maple, Philosophical Magazine B, **82** 1335 (2002)

[53] H.-Ch. Mertins, S. Valencia, W. Gudat, P. M. Oppeneer, O. Zaharko and H. Grimmer, Europhys. Lett., **66** 743 (2004)

[54] Y. Kopelevich et al, J. Low Temp. Phys., **119** 691 (2000)

[55] O. Céspedes, M. S. Ferreira, S. Sanvito, M. Kociak and J. M. D. Coey, J. Phys.: Condens Matter **16** L155 (2004)

[56] G. Kletetschka, P. T. Taylor, P. J. Wasilewski and H. G. M. Hill, Earth Planet. Sci. Letters, **181** 279 (2000)

[57] K. Wakabayashi et al, Physica B **280** 388 (2000)

[58] K. Harigaya, J. Phys. Cond. Matter **13** 1295 (2001)

[59] G. Baskaran and S. A. Jafari, Phys. Rev. Lett., **89** 016402 (2002)

[60] M. Yashima, H. Takahashi, K. Ohtake, T. Hirose, M. Kakihana, H. Arashi, Y. Ikuma, Y. Suzuki and M. Yoshimura, J. Phys. Chem. Solids, **157** 289 (1996)

[61] A. I. Kingon, J. P. Maria and S. K. Streiffer, Nature, **406** 1032 (2000)

[62] M. S. Ramachandra Rao, S. Dhar, S. J. Welz, S. B. Ogale, D. C. Kundaliya, S. R. Shinde, S. E. Lofland, C. J. Metting, R. Erni, N. D. Browning and T. Venkatesan, cond-mat/0405378

[63] J. S. Moodera, X. Hao, G. A. Gibson and R. Meservey, Phys. Rev. Lett., **61** 637 (1988)

[64] D. P. DiVincenzo, J. Appl. Phys., **85** 4785 (1999)

[65] L. Esaki et al, Phys. Rev. Lett., **19** 852 (1967)

[66] A. Hasegawa and A. Yanase, J. Phys. C, **12** 5431 (1979)

[67] H. J. Tromp, P. van Gelderen, P. J. Kelly, G. Brocks and P. A. Bobbert, Phys. Rev. Lett., **87** 016401 (2001)

[68] B. K. Cho, J. S. Rhyee, B. H. Oh, M. H. Jung, H. C. Kim, Y. K. Yoon, J. H. Kim and T. Ekina, Phys. Rev. B, **69** 113202 (2004)

[69] D. P. Young, D. Hall, E. Torelli, Z. Fisk, J. L. Sarrao, J. D. Thompson, H. R. Ott, S. B. Oseroff, R. G. Goodrich and R. Zysler, Nature, **397** 412 (1999)

[70] K. Taniguchi, T. Katsufuji, F. Sakai, H. Ueda, K. Kitazawa and H. Takagi, Phys. Rev.

B, **66** 064407 (2002)

[71] S.E. Lofland, B. Seaman, K. V. Ramanujachary, N. Hur and S. W. Cheong, Phys. Rev. B, **67** 020410(R) (2003)

[72] P. Vonlanthen, E. Felder, L. Degiorgi, H. R. Ott, D. P. Young, A. D. Bianchi and Z. Fisk, Phys. Rev. B, **62** 15 10079 (2000)

[73] H. R. Ott, J. L. Gavilano, B. Ambrosini, P. Vonlanthen, E. Felder, L. Degiorgi, D. P. Young, Z. Fisk and R. Zysler, Physica, **281B & 282B**, 423 (2000)

[74] L. Degiorgi, E. Felder, H. R. Ott, J. L. Sarrao and Z. Fisk, Phys. Rev. Lett., **79** 5134 (1997)

[75] J.-Y. Kim, J.-H. Park, H.-J. Noh, S.-J. Oh, J. S. Yang, D.-H. Kim, S. D. Bu, T.-W. Noh, H.-J. Lin, H.-H. Hsieh and C. T. Chen, Phys. Rev. Lett., **90** 017401 (2003)

Chapter 2

Experimental procedures

2.1 Sample preparation

The samples were either polycrystalline ceramics or thin films produced by pulsed laser deposition from high purity ceramic targets.

2.1.1 Target production

Undoped targets were produced by pressing 1 g of high purity oxide powder into a pellet in a 13 mm diameter hardened stainless steel die under a pressure of about 150 bar in a hydraulic press. They were then removed, placed in a ceramic boat and sintered in a furnace. The sintering conditions used for each material is summarised in the table below. Doped targets were synthesized from stoichiometric amounts of high purity oxide powders which were thoroughly mixed in an agate mortar and pestle under isopropanol for one hour. The powder was then collected, pressed and sintered as for the undoped samples.

	Sintering temperature (°C)	**Duration (hours)**	**Environment**
SnO_2	1150	24	Air
ZnO	900 - 950	12	0.5 bar argon
HfO_2	1200	24	Air
TiO_2: Step 1	700	6	Air
Step 2	1100	24	Air
ITO	1150	24	Air

2.1.2 Pulsed laser deposition

Pulsed laser deposition (PLD) is a flexible thin film deposition technique well suited to growing oxide materials. Reasonable deposition rates can be achieved from ceramic multi-

component targets, although the target material does not necessarily transfer stoichiometrically to the film. A PLD system consists of three basic parts (figure 2.1):

1. A laser
2. Optical lenses, mirrors and apertures to guide the laser beam
3. A vacuum chamber

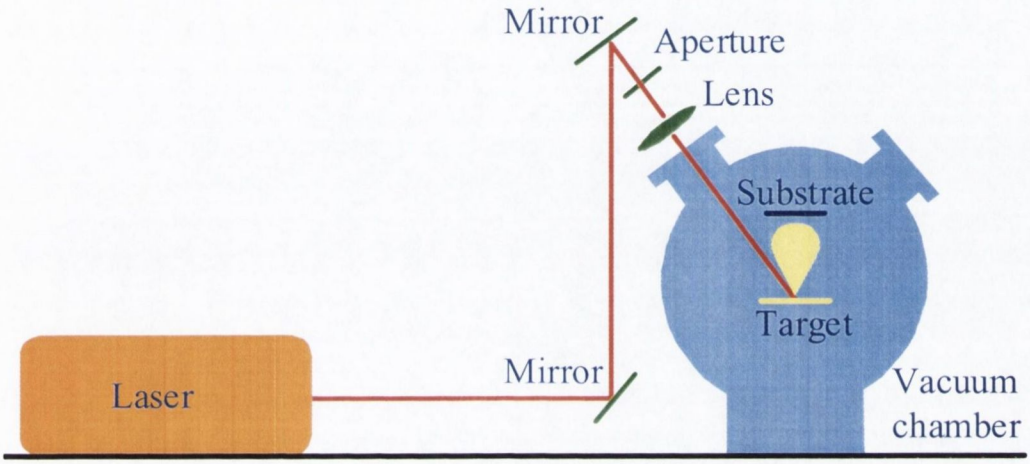


Figure 2.1 An illustration of a PLD system, with laser, optical components and vacuum chamber

The laser beam is guided into the chamber and onto the target by a series of optical componenets - two mirrors to direct the beam, an aperture to select a homogeneous part of the beam and give it a well-defined shape and a lens to focus it onto the target. An energetic plasma is produced which expands away from the target forming a deposit on the substrate. The target is rotated during deposition so that it is ablated uniformly rather than pits being formed. The substrate is attached directly to a SiN heating element with silver paint, and can be heated to a maximum temperature of 950 °C. The base pressure in the chamber is 6 x 10^{-5} mbar and a needle valve can be used to introduce a background gas such as nitrogen or oxygen. Film thickness is monitored by in-situ reflectivity apparatus - a He-Ne laser beam is guided in through a viewport, reflects off the substrate/film and back out through a second viewport where it is guided onto a photodiode. As the film grows the

light intensity recorded by the photodiode varies due to interference between light reflected at the surfaces of the substrate and the growing film. This behaviour can be modelled using the Fresnel equations and a thickness extracted.

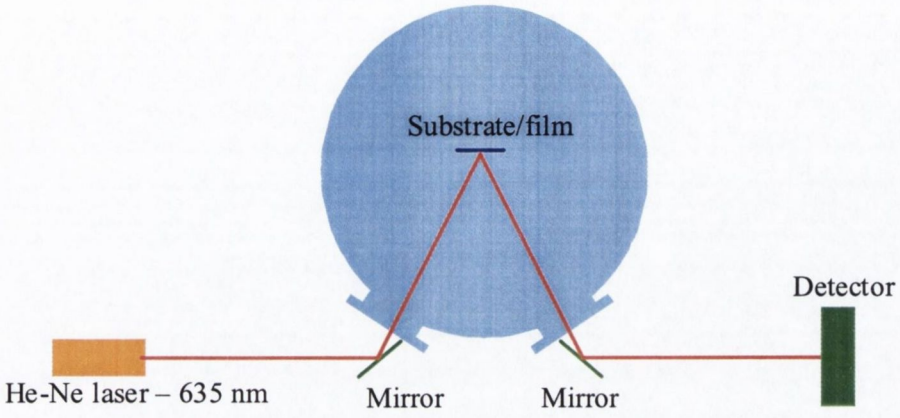


Figure 2.2 The thickness of the film is monitered in-situ by a reflectivity technique as illustrated

The fluence of the laser is given by equation 2.1, and can be changed by adjusting the energy of the laser beam or changing the size of the ablation spot on the target by moving the lens. Thin film composition is particularly sensitive to fluence as it determines the energy of the ionised and neutral species in the plasma. If the fluence is too high it can lead to droplet formation and poor film surface quality.

$$\text{Fluence } (\text{Jcm}^{-2}) = \frac{\text{Energy supplied by the laser (joules)}}{\text{Area of laser spot on the target } (\text{cm}^2)} \tag{2.1}$$

Thin film quality is also sensitive to a variety of other parameters including laser wavelength and repetition rate, substrate temperature, target-to-substrate distance, background gas and pressure. In this thesis, thin films were grown using a KrF excimer laser operating at 248 nm and 10 Hz, with a fluence of 1.8 Jcm $^{-2}$ and a target-to-substrate distance of 35 mm. The oxygen pressure varied from 1 x 10^{-4} to 1 mbar with a substrate temperature between 600 and 900 ° C.

2.2 Phase identification and structural characterisation

2.2.1 X-ray diffraction (XRD)

The wavelength of x-ray radiation is of order a few angstroms - the same as typical interatomic distances in crystalline solids. In 1912 W. L. Bragg recognised that when certain geometric requirements are met, x-rays scattered from a crystalline solid can constructively interfere to produce a diffracted beam. Braggs law, the condition for constructive interference, is given by:

$$n\lambda = 2d\sin\theta \tag{2.2}$$

where n is an integer, λ is the wavelength of the x-ray radiation and θ its angle of incidence, and d is the distance between lattice planes. X-ray diffraction patterns can be analysed to reveal a samples crystal structure and orientation, as well as d, the distance between lattice planes, and lattice parameters a and c. The Joint Committee on Powder Diffraction Standards (JCPDS) maintains a database of diffraction patterns.

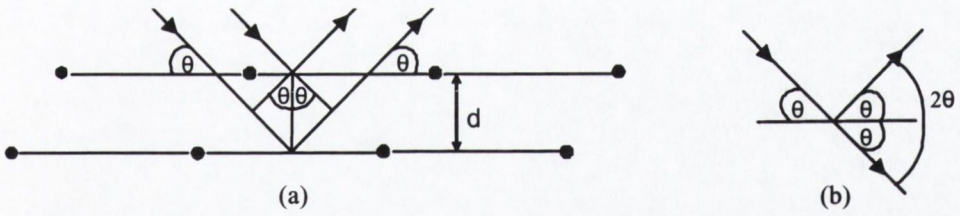


Figure 2.3 (a) A Bragg reflection from a particular set of lattice planes separated by a distance d and (b) θ is just half of the total angle by which the incident beam is deflected

A Siemens D500 diffractometer was used with Cu-K_α radiation of wavelength λ = 1.5406 Å. Powder samples were prepared by placing them flat using vacuum grease on a silicon or glass slide, while films were mounted using double-sided adhesive tape. 2θ was scanned from 20 - 80°, with a step size of 0.02° and a 1 s count time at each step.

2.2.2 X-ray reflectivity

X-ray reflectivity (XRR) was performed in a Philips X-Pert Pro to determine film thickness. XRR is a grazing incidence scattering technique where the incident and scattered beams are at equal angles to the film surface (figure 2.4). Films can be epitaxial, polycrystalline or amorphous.

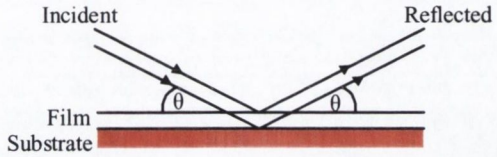


Figure 2.4 Specular reflection of the x-ray beam from the film surface and the film/substrate interface

An interference pattern is formed between reflections from the film surface and from the film/substrate interface (figure 2.5). The thickness is determined from the periodicity of the fringes, the angle at which the intensity begins to drop is indicative of the density and roughness can be estimated from the damping of the fringes and the rate at which the intensity decreases with increasing angle. Software supplied with the Philips machine allows the user to generate a fit to the measured data by varying any of these parameters.

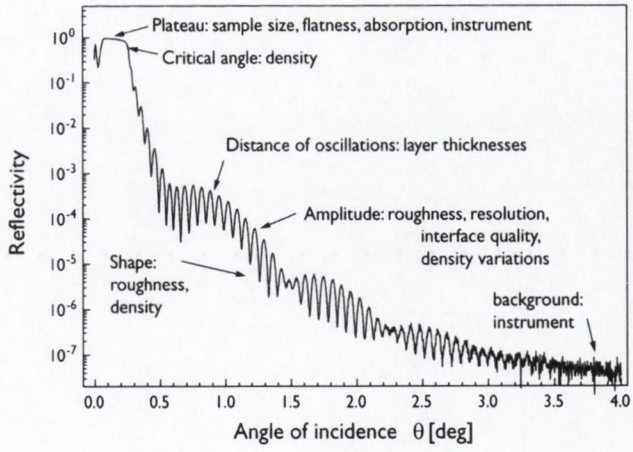


Figure 2.5 A sample x-ray reflectivity curve with its features highlighted and their sources explained (from Philips/Panalytical)

2.2.3 Microscopy

Sample morphology was studied using a Hitachi S - 3500N scanning electron microscope (SEM) in high vacuum mode with sub-micron resolution, in the Centre for Microscopy and Analysis (CMA), Trinity College. SEM involves the detection of secondary or back-scattered electrons following the bombardment of the sample with a beam of highly focused electrons. The electrons, which possess a much greater energy than optical photons, give rise to a much higher magnification and image resolution than an optical microscope.

This unit is also equipped with a PGT-Imix EDAX (energy dispersive analysis of x-rays) facility. This allows the analysis of x-rays emitted when a sample is bombarded with electrons, as illustrated in figure 2.6. These x-ray are characteristic of the elements present. The data is calibrated with a known specimen and the relative concentration of the elements may then be concluded. Light elements such as H, B, C, N and O are diffi cult to detect due to the low energy of their x-rays. This technique is used to determine the chemical composition of compounds and to identify the impurities present which are usually based on analyses of three separate areas of the sample surface.

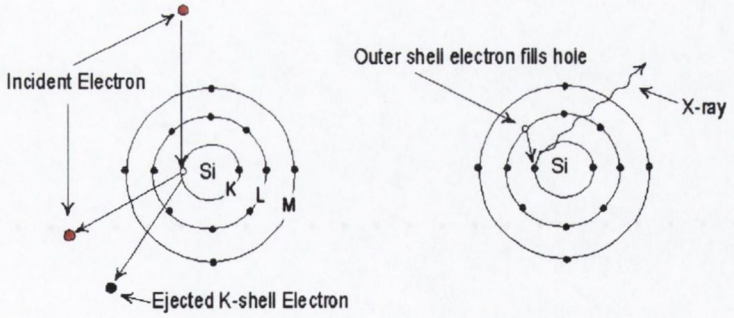


Figure 2.6 The incident electron from the SEM column causes an inner shell (K) electron to be emitted and replaced by an electron from an outer shell (L), also producing an x-ray

The detection limit of the system is $\sim$ 1 wt. %. Therefore when the doping level is low, the system is not quantitatively accurate, and so x is extrapolated from the high

concentration data.

High-resolution images were obtained from a Hitachi H-7000 transmission electron microscope (TEM) in CMA and a second High-Resolution Hitachi TEM in Japan which was also equipped with an EDAX system. In this case, a beam of highly focused electrons interact with atoms in the sample and information is obtained from both deflected and non-deflected transmitted electrons, back-scattered and secondary electrons, and emitted photons. Thin sample cross-sections were prepared by focused ion beam (FIB) milling in TCD.

2.2.4 Optical spectrometry

Optical spectrometry measurements were performed in a dual-beam Cary spectrophotometer. The machine is first balanced by running with the sample holders in place (but no samples) and the transmission detected at both arms set to be equal. A blank substrate is then loaded in one arm as a reference sample, with the film and substrate in the second arm, as shown in figure 2.7. In this way the transmission of the film is obtained, although a correction needs to be made for reflections from the additional interface. Measurements were typically made in the 315 - 1500 nm range (4 - 0.8 eV), although several samples were measured from 200 - 1500 nm.

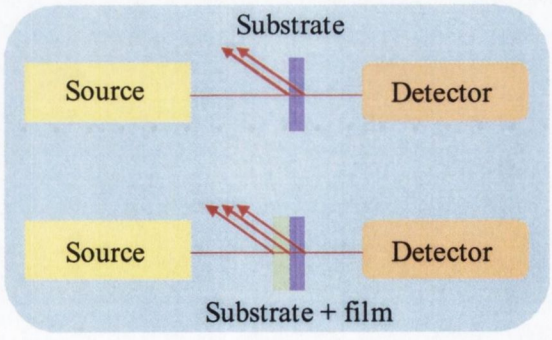


Figure 2.7 Illustration of the dual beam spectrophotometer set-up

2.2.5 Chemical Analysis

Chemical analysis was performed by Activation Laboratories in Ontario, Canada. Their analysis techniques included loss-on-ignition (LOI), Inductively Coupled Plasma Mass Spectrometry (ICPMS), Inductively Coupled Plasma Optical Emission Spectrometry (ICPOES), Neutron Activation Analysis (NAA) and x-ray fluorescence (XRF).

2.3 Magnetic measurements

2.3.1 Thermogravimetric analysis

Thermomagnetic measurements were used to determine the Curie temperature of samples. The samples are placed onto a platinum crucible and the sample space purged with argon. An inhomogeneous magnetic field is applied to the sample which is balanced by a counter weight on a cantilever as illustrated in figure 2.8. The temperature of the sample is increased, which results in the loss of its magnetisation, and the lever tilts towards the counterbalance indicating the Curie temperature of the sample. The sensitivity is suffi cient for ceramics, but not for thin film samples.

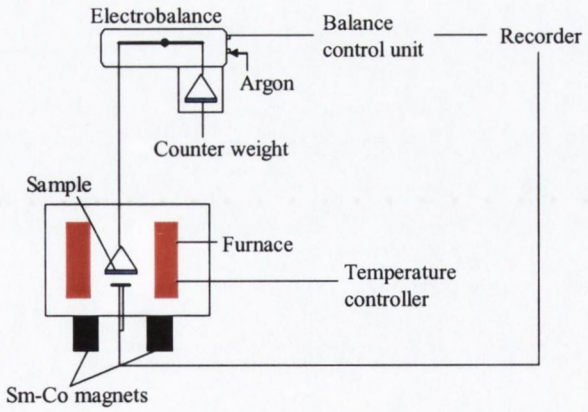


Figure 2.8 Schematic diagram of the thermomagnetic measurement apparatus

2.3.2 Magnetic Force Microscopy (MFM)

MFM images of the samples were made using a Digital Instruments MultiMode AFM/MFM with sub-nanometer resolution. In MFM, a tapping cantilever equipped with a special low-moment or high-moment magnetic tip is first scanned over the surface of the sample to obtain topographic information. The tip is then raised just above the sample surface. The surface topography is scanned while being monitored for the influence of magnetic forces. These influences are measured using the principle of force gradient detection. In the absence of magnetic forces, the cantilever has a resonant frequency f_o. This frequency is shifted by an amount, Δf, proportional to vertical gradients in the magnetic forces on the tip. The shifts in resonant frequency tend to be very small, and are measured by directly tracking shifts in resonant frequency.

2.3.3 Vibrating sample magnetometry

Room temperature vibrating sample magnetometery measurements were performed in a variable field created by two concentric Halbach cylinders. The magnitude of the field was changed by rotating the cylinders so that the vector addition of their magnetisation added to the desired applied field, up to a maximum of 1.1 T. The sample was vibrated at 29.4 Hz along the bore of the cylinders (H $\perp$ bore). This induces a voltage in a set of pick-up coils, also inside the bore, which can be converted into a magnetic moment after calibration with a nickel standard. Figure 2.9 is a schematic diagram of a vibrating sample magnetometer.

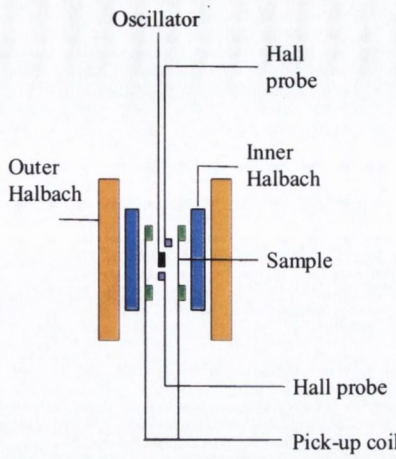


Figure 2.9 Schematic diagram of the vibrating sample magnetometer

2.3.4 Superconducting Quantum Interference Device (SQUID)

A Quantum Design Magnetic Property Measurement System (MPMS) sample magnetometer was used to characterise the magnetic properties of thin films. A superconducting quantum interference device (SQUID) detection system is integrated with a temperature control unit, a high field superconducting magnet and the computer operating system. Liquid helium is necessary for refrigeration of the superconducting components as well as for low temperature measurements. The exceptional sensitivity of the magnetometer makes it ideal for thin film measurements where the signals are too weak for detection in a VSM. Measurements can be made between 1.7 and 800 K in a field of up to 5 T, with a sensitivity of 10^{-11} Am^2.

Measurements used the Reciprocating Sample Option (RSO) where the sample is vibrated parallel to the field direction. Powders were weighed, then placed in gel caps and inserted into a straw for measurement. Thin films were deposited on square substrates. Their corners were broken off using a diamond scribe, leaving an octagonal shape, so that they just fitted into the straws directly.

2.4 Electrical measurements

2.4.1 Four-point resistivity measurements

The definition of resistivity, ρ, is given by equation 2.3 where R is resistance, A is the area of the sample cross section and L is the distance between contacts.

$$\rho = \frac{RA}{L} \tag{2.3}$$

An alternative formula is given by equation 2.4 which is commonly used when considering wafers and thin films measured by the van der Pauw method. Here t is the sample thickness in cm.

$$\rho = \frac{\pi t}{\ln 2} R \tag{2.4}$$

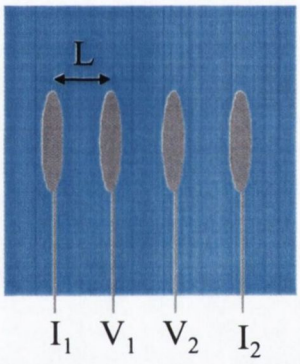


Figure 2.10 Sample (blue) with current (I) and voltage (V) contacts for resistivity measurements

Resistance measurements are performed in the SQUID magnetometer between 5 and 300 K using a specially prepared sample probe. Silver wires are attached to the sample with silver paint to give four in-line equidistant contacts as shown in figure 2.10. A current is applied between the two outer contacts and the voltage measured across the inner contacts to determine the resistance (V = IR). Typically the applied current is between 1 μA and 1 mA, with low current values for high sample resistance and vice versa.

Chapter 3

$Sn_{1-x}M_xO_2$, M = Mn, Fe, Co

3.1 Introduction

SnO_2 is a wide bandgap (3.97 eV) $n-$ type semiconductor. It has the rutile structure as shown in figure 3.1, with a body centred cation surrounded by six oxygen nearest neighbours forming octahedral ligands of oxygen. It takes the $P4_2/mnm$ space group with lattice parameter values of 4.74 Å for a and 3.19 Å for c. The radius of a Sn^{4+} ion is 74 pm and that of O^{2-} is 135 pm. SnO_2 has a molecular weight of 150.71, a density of 6.95 gcm^{-3}, a melting point of 1127 ° C and a boiling point of 1800 - 1900 ° C. The powder is white and thin films are transparent.

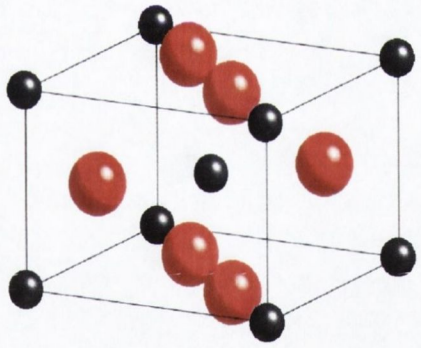


Figure 3.1 The rutile SnO_2 crystal structure with Sn atoms in black and oxygen atoms in red

Thin films have been grown using a variety of techniques including RF sputtering, pulsed laser deposition, pulsed-electron-beam deposition, chemical vapour deposition, spray pyrolysis and sol-gel processing. They are widely used as transparent conducting electrodes in flat-panel displays and solar cells, optoelectronic devices, gas sensing and IR detectors.

Interest in SnO_2 as a magnetic semiconductor has only recently arisen, primarily be-

cause of a report by Ogale et al [1] claiming that cobalt doped SnO_2 is ferromagnetic with a giant magnetic moment of 7.5 μ_B/Co and a Curie temperature of 650 K. Kimura et al [2] had previously reported that Mn-doped SnO_2 is not ferromagnetic. They grew $Sn_{1-x}Mn_xO_2$ thin films ($x \leq 0.34$) by PLD on R-cut sapphire substrates and found that the magnetisation exhibited paramagnetic behaviour. Most dilute magetic semiconductor systems studied to date are $p-$type, but materials such as SnO_2 with $n-$type conduction are also essential for spin electronic devices.

3.2 Bulk material

The oxides $Sn_{1-x}M_xO_2$, with x = 0.001 - 0.05, were synthesised from stoichiometric amounts of high purity (99.99 %) SnO_2 and MO (M = Mn, Fe, Co) powders. They were ground thoroughly in an agate mortar for one hour under isopropanol, then pressed into pellets and sintered for 24 hours at 1150 ° C in air. Table 1 summarises the compositions that were produced. A $Sn_{0.95}Fe_{0.05}O_2$ sample was also prepared using ^{57}Fe-rich α-Fe_2O_3, as well as several undoped samples.

x	Mn	Fe	Co
0.001	✓	×	×
0.003	✓	×	×
0.005	✓	✓	✓
0.010	✓	✓	✓
0.015	✓	✓	✓
0.020	✓	✓	✓
0.025	✓	✓	×
0.030	✓	✓	✓
0.040	✓	✓	✓
0.050	✓	✓	✓

Table 1.List of bulk ceramics of Mn, Fe and Co doped tin oxide produced

X-ray diffraction confirms the formation of a rutile SnO_2 structure in all samples. Figure 3.2 shows the patterns for the undoped sample as well as all three dopants at 5 at.

%, with the reflections indexed on the basis of a tetragonal unit cell.

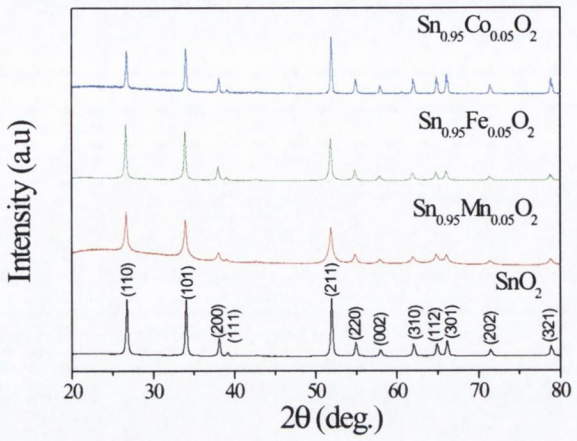


Figure 3.2 X-ray diffraction pattern of undoped SnO_2, and $Sn_{1-x}M_xO_2$ with $x = 0.05$ for M = Mn, Fe, Co

Figure 3.3 illustrates the variation of lattice parameters 'a' and 'c' in $Sn_{1-x}Co_xO_2$ with x. Both saturate at $x \sim 0.02$, indicating the solubility limit for cobalt in SnO_2. Substitution of transition metal ions dilates the lattice and the unit cell volume expansion is about 0.4 % for all samples with $x = 0.05$ (Table 2).

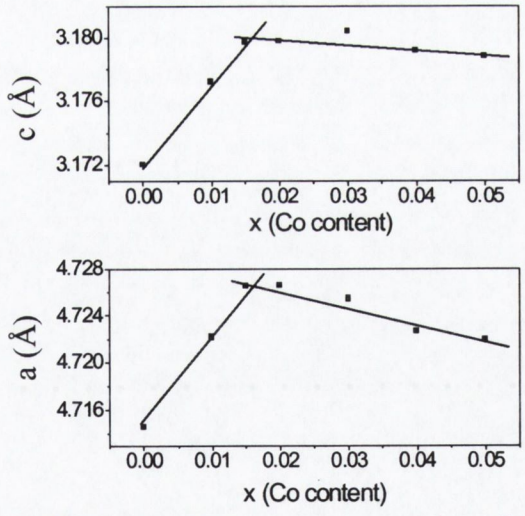


Figure 3.3 Variation of lattice parameters in $Sn_{1-x}Co_xO_2$ with x

Energy dispersive x-ray analysis (EDAX) indicates that all samples show the nominal transition metal concentration. However, elemental mapping of the $x = 0.05$ samples reveals

the presence of small oxide clusters, rich in $3d$ transition metal (figure 3.4a). This secondary phase was identified as $SnCo_2O_4$ in the cobalt doped material (figure 3.4b) and $\alpha-$ Fe_2O_3 in the FeO doped sample by XRD, but no impurity phases were identified by XRD in the Mn doped sample.

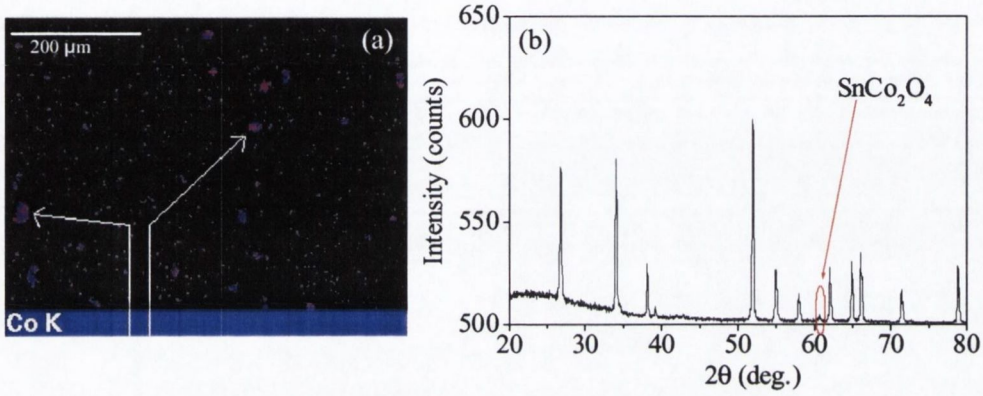


Figure 3.4 (a) Mapping of the $Sn_{0.95}Co_{0.05}O_2$ samples revealed the presence of cobalt clusters while XRD (b) indicates an $SnCo_2O_4$ secondary phase

Figure 3.5a compares magnetisation data for the 5 % doped samples, at 300 K and 5 K. Room temperature saturation magnetization is 0.2 and 1.8 Am^2kg^{-1} for $Sn_{0.95}Mn_{0.05}O_2$ and $Sn_{0.95}Fe_{0.05}O_2$ respectively. The Co-doped samples are paramagnetic at room temperature. The corresponding ferromagnetic moments are 0.11, 0.95 and 0.0 μ_B per Mn, Fe and Co atom. Hysteresis is not observed in any bulk sample. The room temperature ferromagnetism of the Mn and Fe material cannot be attributed to the impurity phases. Possible impurity phases in the Mn doped samples are $SnMn_2O_4$ or Mn_3O_4 with Curie temperatures in the range of 40 – 50 K; they may well be responsible for the increased ferromagnetism at 5 K seen in figure 3.5. In the Fe-doped samples the Sn-doped haematite found by XRD is only very weakly magnetic [3]. Curie temperature measurements were performed in an Alternating Gradient Force Magnetometer on the $Sn_{0.95}Mn_{0.05}O_2$ and $Sn_{0.95}Fe_{0.05}O_2$ samples, with values of 340

K and 360 K found for the Mn and Fe samples respectively (figure 3.5b).

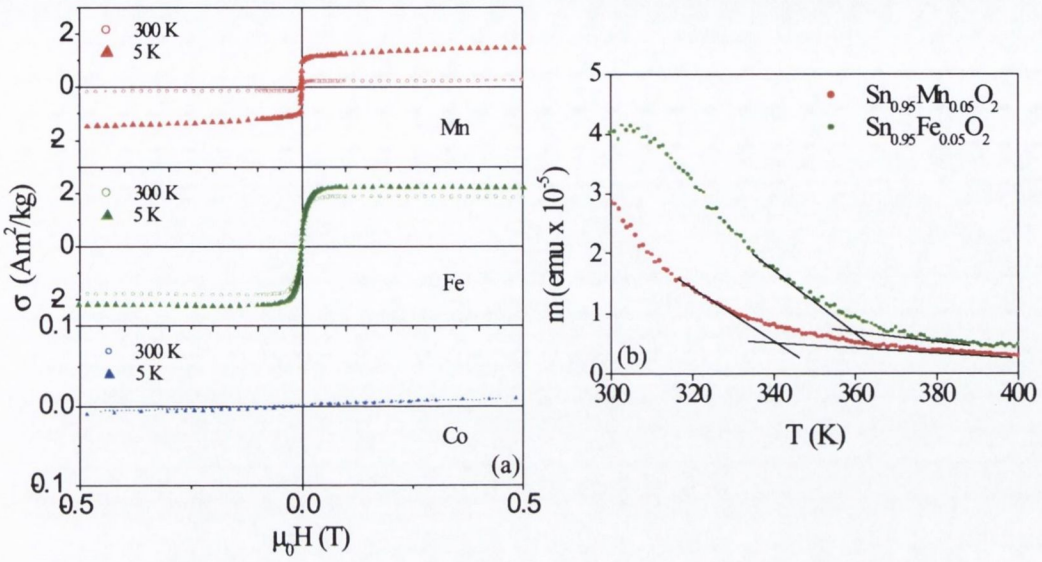


Figure 3.5 (a) Magnetisation of $Sn_{0.95}Mn_{0.05}O_2$, $Sn_{0.95}Fe_{0.05}O_2$ and $Sn_{0.95}Co_{0.05}O_2$ bulk ceramics and (b) the Curie temperature curves for the Mn and Fe doped samples

Table 2 summarises the lattice parameters and magnetic properties of $Sn_{1-x}M_xO_2$ powders where M = Mn, Fe or Co.

Sample	**a** (Å)	**c** (Å)	V (Å^3)	μ_B/M atom	T_c (K)
SnO_2	4.71	3.172	70.5	-	-
$Sn_{0.95}Mn_{0.05}O_2$	4.72	3.181	71.1	0.11	340
$Sn_{0.95}Fe_{0.05}O_2$	4.73	3.181	71.2	0.95	360
$Sn_{0.95}Co_{0.05}O_2$	4.72	3.179	70.9	0.0	-

Table 2.Lattice parameters and magnetic properties of bulk undoped and Mn, Fe and Co doped tin oxide

3.3 Thin films

Thin films were deposited by PLD from all of the targets listed in Table 1, as well as undoped SnO_2. They were grown on R-cut $(1\bar{1}02)$ sapphire substrates at 740 ° C in 1.10^{-4} mbar of oxygen with a 10 minute deposition time. In addition, a series of $Sn_{0.95}Co_{0.05}O_2$ films were grown with deposition times of 1, 3, 5, 10 and 15 minutes with a typical deposition

rate of 10 nm/minute. The undoped sample is transparent, as are the Mn and Co doped films, while Fe doping results in a faint brown tinge. The x-ray diffraction patterns (figure 3.6) show the rutile-structure films to be single phase and well oriented with a (101) texture. The full width at half maximum (FWHM) for a 150 nm thick $Sn_{0.95}Co_{0.05}O_2$ film is 0.72°.

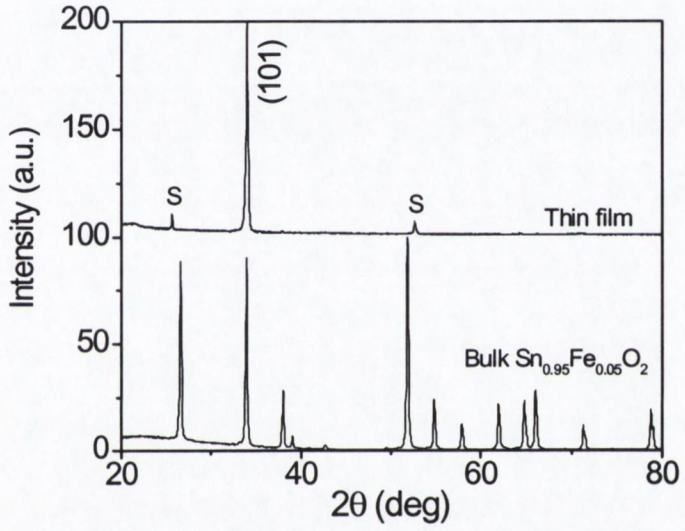


Figure 3.6 X-ray diffraction pattern of a $Sn_{0.95}Fe_{0.05}O_2$ ceramic target and a corresponding thin film. "S" indicates substrate peaks

Lattice parameters cannot be calculated, and only the d_{101} lattice spacing can be inferred which is plotted as a function of concentration in figure 3.7a. The Powder Diffraction File (PDF no. 41-1445) value for d_{101} in SnO_2 is shown as a solid black line, while the measured value for the SnO_2 powder used to make the targets is shown as a red line. The films are strained, elongated perpendicular to the plane of the substrate. The strain does not vary with film thickness, as indicated by figure 3.7b. Neither does d_{101} vary linearly with x (Vegards law).

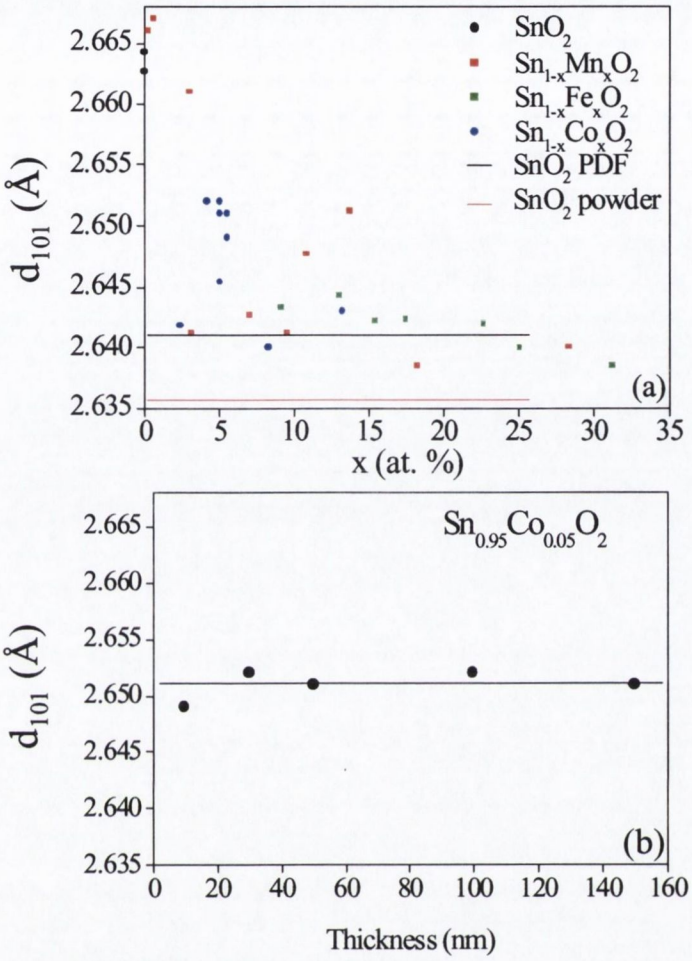


Figure 3.7 (a) The d_{101} lattice spacing for SnO_2 and $Sn_{1-x}M_xO_2$ films, with the Powder Diffraction File (PDF) value of d_{101} indicated with a solid black line and the d_{101} value of SnO_2 powder shown as a red line and (b) d_{101} as a function of thickness in $Sn_{0.95}Co_{0.05}O_2$ thin films

The ionic radius of Sn^{4+} is 74 pm, while those of Mn, Fe and Co for different charge states are shown in Table 3. Manganese most likely takes the Mn^{3+} ($3d^4$) state, cobalt could be Co^{2+} ($3d^7$) or Co^{3+} ($3d^6$), while the radius of the Sn^{4+} ion falls between that of Fe^{3+} ($3d^5$) and Fe^{2+} ($3d^6$). However, we have reported that Mössbauer studies of SnO_2 films doped with ^{57}Fe-rich α-Fe_2O_3 show that the Fe is all high spin Fe^{3+} [4].

	Mn	Fe	Co
2+	91 pm	82 pm	82 pm
3+	70 pm	67 pm	64 pm
4+	52 pm		

Table 3.Ionic radii of Mn, Fe and Co charge states

Unlike the targets, the films show no sign of any micron-scale non-uniformity in the distribution of transition metals in EDAX analysis and elemental mapping. However, the composition of the fims are very different from those of the ceramic targets from which they were made. The nominal composition x' is plotted against the measured composition x determined by EDAX analysis in figure 3.8. Pulsed laser deposition does not maintain the stoichiometry of the target in face of the volatility of SnO_2. The films contain roughly four-five times as much of the $3d$ element as the targets. When x is small EDAX analysis is unreliable, so an extrapolated value of x is used.

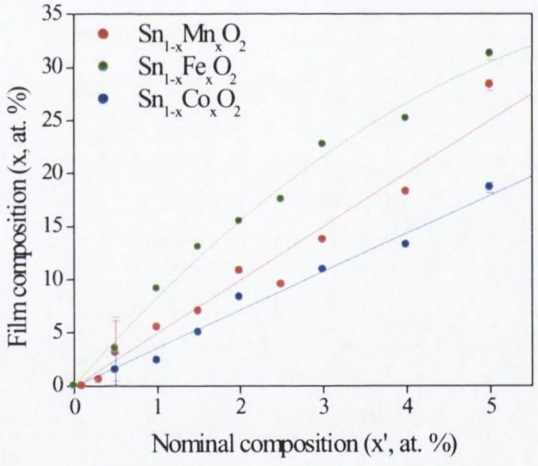


Figure 3.8 Plot of the composition of the film x versus the nominal composition of the target x'

Figure 3.9 is a high resolution TEM image of a cross section of a $Sn_{0.94}Mn_{0.06}O_2$ thin film which is about 65 nm thick on a sapphire substrate with a gold capping layer. Analysis by the EDAX system on the TEM again showed no appreciable compositional variation across the film.

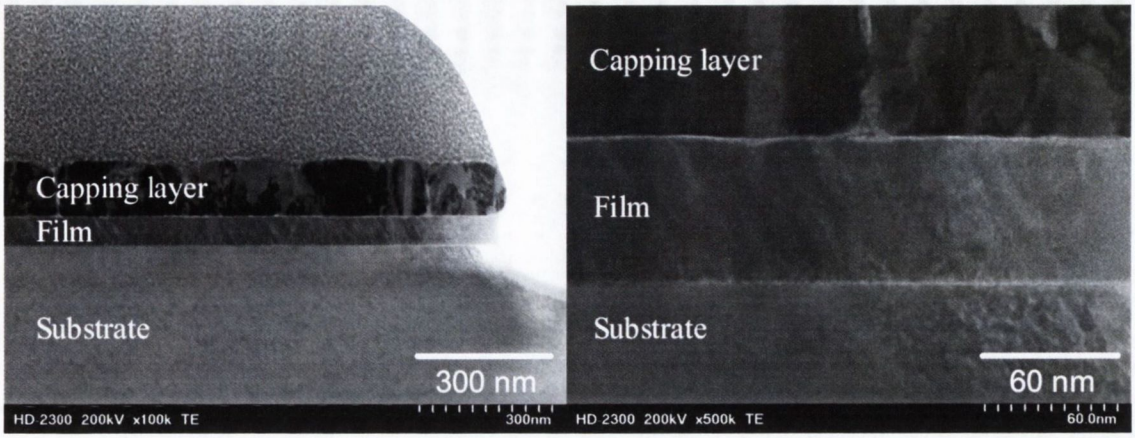


Figure 3.9 Transmission electron microscope images of a $Sn_{0.94}Mn_{0.06}O_2$ thin film

The films are smooth, with no evidence of the droplets often seen in films produced by PLD. In figure 3.9 the peak to peak surface undulation in the $Sn_{0.94}Mn_{0.06}O_2$ film is 1.5 nm. A much thicker (240 nm) $Sn_{0.75}Fe_{0.25}O_2$ film appears featureless in SEM (figure 3.10a), while AFM images of the same film (figure 3.10b) show a blister-like surface topology, with a root mean square roughness of 5 ($\pm$ 0.5) nm, and grains approximately 200 nm in diameter.

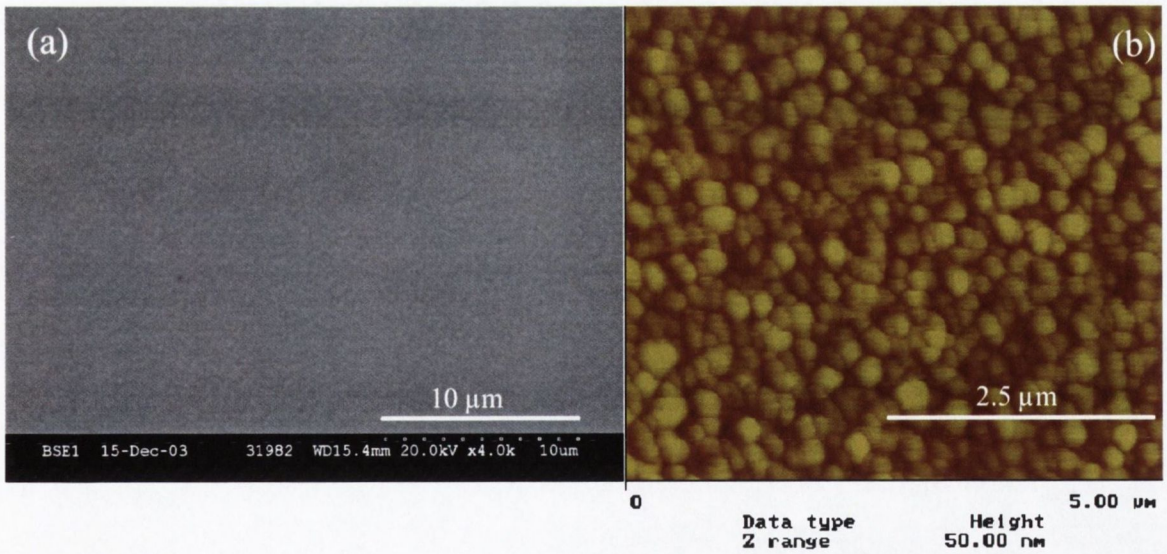


Figure 3.10 (a) An SEM image of the surface of a $Sn_{0.75}Fe_{0.25}O_2$ thin film and (b) an AFM image of the surface of the same film

Film thickness was determined in a number of ways - during deposition by reflectivity

(figure 3.11a,b), by x-ray reflectivity (figure 3.11c), using high resolution microscope images (figure 3.9) or by patterning a line on the film (with the rest of the film protected by resist) and argon-ion milling until the substrate was reached. Films had to be conducting for this to work as there is no end-point detector on the mill - the resistance along the line was checked frequently until it was no longer measurable, and it was then presumed the substrate had been reached.

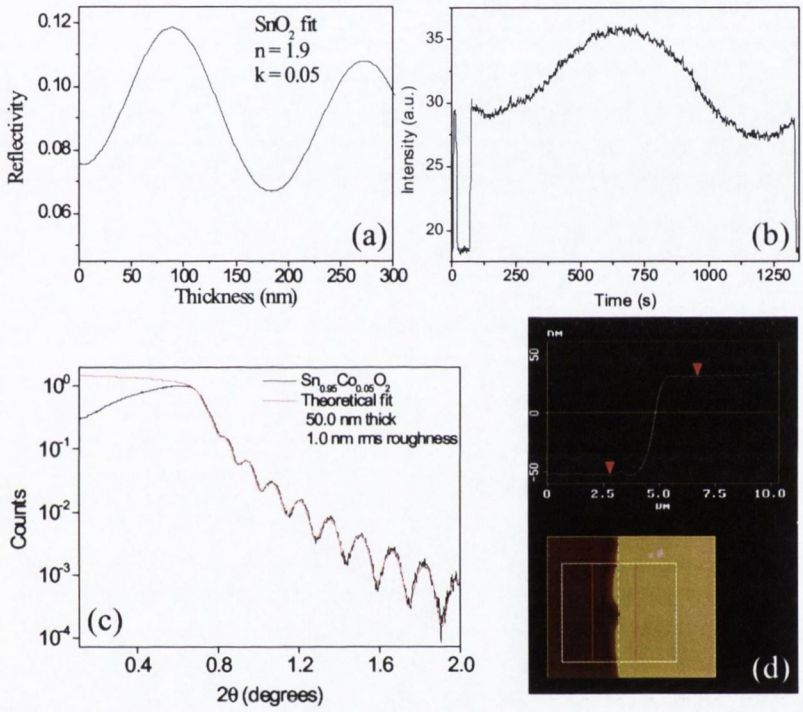


Figure 3.11 (a) shows the calculated reflectivity curve for the growth of SnO_2 on sapphire with the optical constants as shown while (b) is the data recorded during a 20 minute deposition of a $Sn_{0.81}Co_{0.19}O_2$ thin film, indicating that the film is approximately 200 nm thick (c) is the small-angle x-ray reflectivity data and fit for a 50 nm thick $Sn_{0.95}Co_{0.05}O_2$ thin film and (d) is an AFM measurement of the step height in a milled $Sn_{0.87}Fe_{0.13}O_2$ thin film - the film is 84 nm thick

The step height was measured in the AFM (figure 3.11d). In this way the film thickness could be independently confirmed by several methods. Film thickness ranged between 10 and 250 nm.

The absorption band edge appears at $\sim$ 305 nm (4.1 eV) in pure and doped samples

as shown in figure 3.12a and is broadest in the pure sample. Film transmission is about 80 % for all four samples. The oscillations in the data are thickness interference fringes and are not indicative of any structure in the samples. The transmission spectra for the $Sn_{1-x}Fe_xO_2$ series of films is shown in figure 3.12b. Transmission tends to decrease with increasing x for Mn, Fe and Co doping.

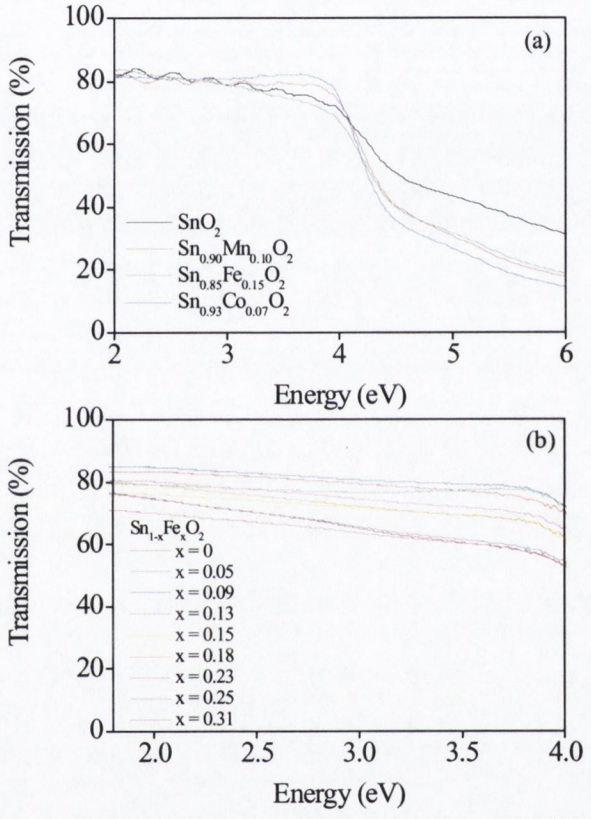


Figure 3.12 (a) Absorption spectra for undoped and doped SnO_2 films and (b) the transmission spectra for the $Sn_{1-x}Fe_xO_2$ series of films

Pure SnO_2 films are conducting at room temperature, as are Co doped samples for all values of x, while Mn and Fe doped films are conducting when $x \leq 0.07$ and $x \leq 0.15$ respectively. The electrical conductivity of undoped SnO_2 is that of a degenerate $n-$type semiconductor. Room temperature resistivity is 7.2 mΩcm with an activation energy of 19.5 meV which drops to 0.2 meV at low temperatures. The activation energy (E_A) is determined

by plotting ln ρ versus 1/T and the resulting slope equals $E_A/2k$, where k is Boltzmanns constant. The cobalt doped films are the only series that are conducting for all values of x, with room temperature resistivity varying from 83 mΩcm for $x = 0.015$ to 9.7 Ωcm for $x = 0.19$. Figure 3.14a shows the resistivity of SnO_2 as well as $Sn_{1-x}Co_xO_2$ films, for $x = 0.02$, 0.11, 0.19, as a function of temperature.

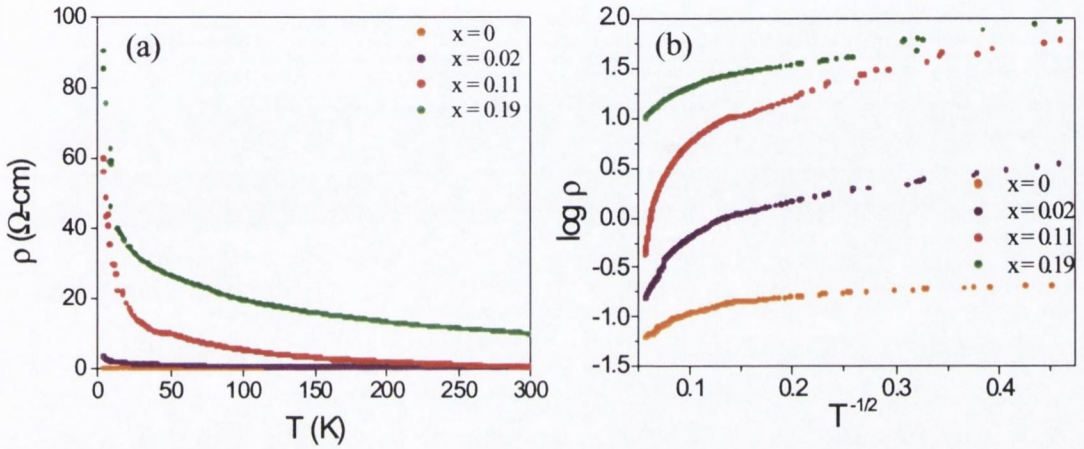


Figure 3.14 Resistivity of the $Sn_{1-x}Co_xO_2$ series plotted (a) on a linear scale and (b) on a logarithmic scale versus $(1/T)^{\frac{1}{2}}$

Resistivity was also plotted on a logarithmic scale versus $T^{-\frac{1}{2}}$ in figure 3.14b following a report by Kennedy et al [5] that resistivity follows a log $\rho \sim T^{-\frac{1}{2}}$ dependence over a wide temperature range in cobalt doped TiO_2 films as a result of cobalt clusters. This behaviour is characteristic of hopping transport in a multiphase system. However, we observed no such resistivity dependence and no evidence of cobalt clusters in our films.

Magnetisation curves were measured for all samples at 5 K and 300 K in the SQUID magnetometer. Figure 3.15 shows room temperature data for Mn, Fe and Co doping for nominal doping concentrations of 5 at. %. All compositions are magnetically ordered at room temperature. Hysteresis is observed in all Fe compounds for $x \geq 0.13$ and in the $x = 0.28$ Mn-doped sample at 5 K, while none is observed in any Co-doped films.

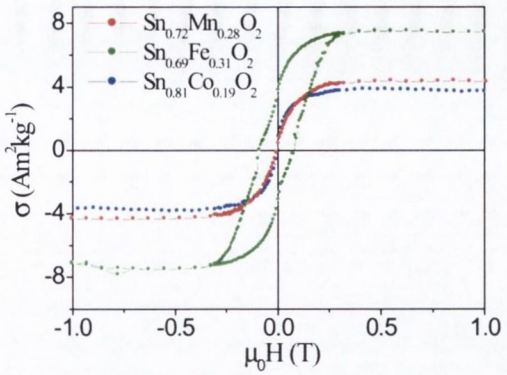


Figure 3.15 Room temperature magnetisation curves of $Sn_{0.72}Mn_{0.28}O_2$, $Sn_{0.69}Fe_{0.31}O_2$ and $Sn_{0.81}Co_{0.19}O_2$ thin films

While the field is applied perpendicular to the plane of the films in figure 3.15, several measurements were made in the parallel configuration, revealing large and unexpected anisotropy of the saturation magnetisation. Figure 3.16 shows the data for films made from $Sn_{0.98}M_{0.02}O_2$ (M = Mn, Fe or Co) targets, with the moment always being largest in the perpendicular direction.

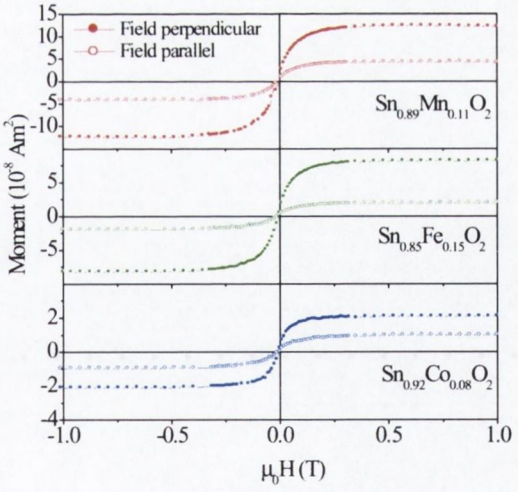


Figure 3.16 Magnetisation plots of $Sn_{0.89}Mn_{0.11}O_2$, $Sn_{0.85}Fe_{0.15}O_2$ and $Sn_{0.92}Co_{0.08}O_2$ thin films measured perpendicular and parallel to the field

Figure 3.17a is a plot of the magnetisation data (measured in the perpendicular direc-

tion) expressed as moment per transition metal cation. Despite the scatter there is a distinct trend - the moment increases steadily as x is reduced, reaching values comparable to the spin-only values when $x < 2$ % - in one case we found a moment of 20 μ_B/Mn when x = 0.003 . In figure 3.17b the moment is plotted per unit substrate area and extrapolates (with considerable scatter) to a non-zero value of 150 - 200 $\mu_B \mathrm{nm}^{-2}$.

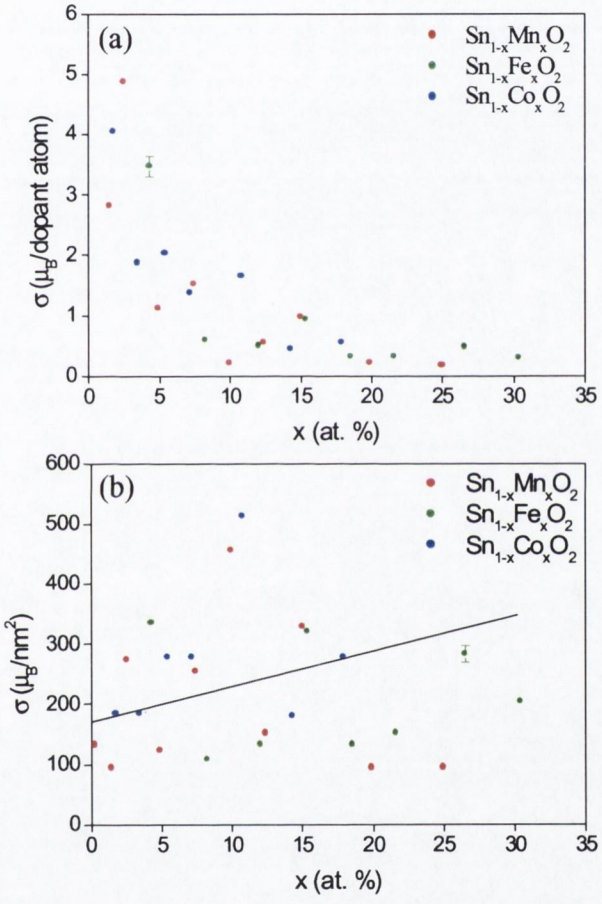


Figure 3.17 (a) The magnetic moment per transition metal ion for thin films of $Sn_{1-x}M_xO_2$ with M = Mn, Fe or Co and (b) the magnetic moment expressed per unit substrate area, with representative error bars

The fall-off in moment with increasing x in figure 3.17a can be rationalised in terms of a random distribution of cobalt ions over the cation sites in the rutile lattice. Isolated ions contribute the full moment m, pairs and most groups of four are antiferromagnetically

coupled and make no net contribution, triplets contribute m/3. Large antiferromagnetically-coupled clusters of N atoms will make a contribution $m/N^{1/2}$.

A program was written to test this model - dopant atoms are placed in sites in a rutile lattice randomly selected by the computer. When all the dopant atoms are placed according to the chosen value of x, the program then steps its way through the lattice identifying isolated atoms, pairs and clusters. If a dopant atom is encountered all of its nearest neighbour sites are checked for more dopant atoms - if one is found then all of its nearest neighbours are checked and so on. Once a dopant atom has been identified it is marked so as not to count it again. Moments were then assigned as above, depending on cluster size. The model reproduces the trend in figure 3.17, provided the transition metal distribution is weighted in favour of nearest-neighbour pairs. When the program can randomly dope the lattice the probability, P, of an incoming dopant atom being placed in a nearest neighbour site of another dopant atom is given by

$$P = \frac{\text{Number of available sites with a nearest neighbour dopant atom}}{\text{Total number of available sites}} \tag{3.1}$$

To increase the chances of dopant atoms clustering P is multiplied by a constant a, which is greater than one. The computer then "rolls a dice" to give a number between 1 and 100. If this number is less than or equal to $P.a$, the incoming dopant atom is placed in a random site with a nearest neighbour dopant atom.

Figure 3.18 shows the fit where the full moment m'is 3 μ_B (the spin-only value for Co^{2+}) with the incoming dopant atom five times more likely to have a dopant atom nearest neighbour than in the random doping situation ($a = 5$). While the shape of the fit echoes that of the data, it sits too low to fully account for the observed ferromagnetism.

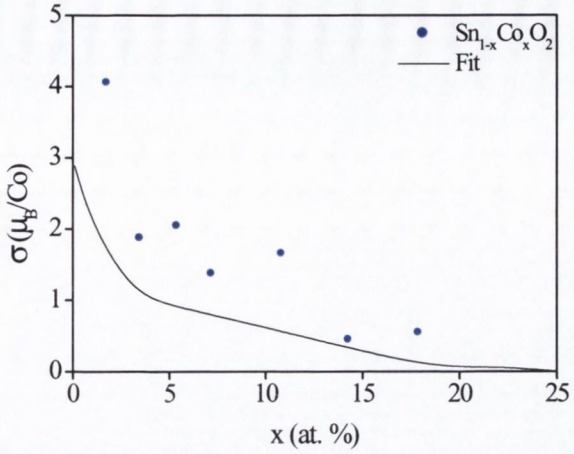


Figure 3.18 Moment per dopant atom, with a theoretical fit to cobalt using a maximum moment of 3 μ_B/Co

However, figure 3.17b shows that the moment per unit substrate area extrapolates to a value of 150 - 200 $\mu_B \text{nm}^{-2}$. This suggests a contribution to the magnetic moment from a source which is in addition to the effect of Co doping. It may be that defects introduced at the film/substrate interface are involved somehow in producing the ferromagnetic signal. In figure 3.19 this constant value of 150 $\mu_B \text{nm}^{-2}$ is added to the fit shown in figure 3.18, producing a better fit to the data.

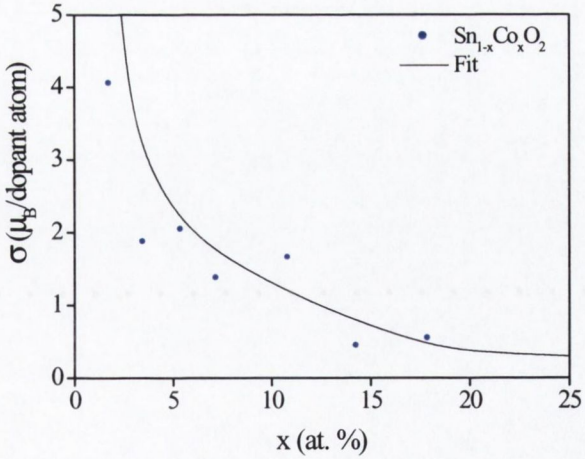


Figure 3.19 The computational fit using a maximum moment of 3 μ_B/Co plus an additional constant contribution of 150 $\mu_B \text{nm}^{-2}$ from interface defects

Figure 3.20a shows that the moment of $Sn_{0.81}Co_{0.19}O_2$ films is independent of thickness,

while figure 3.20b plots the room temperature moment per cobalt atom as a function of thickness. The moment is largest for the thinnest film and drops with increasing thickness.

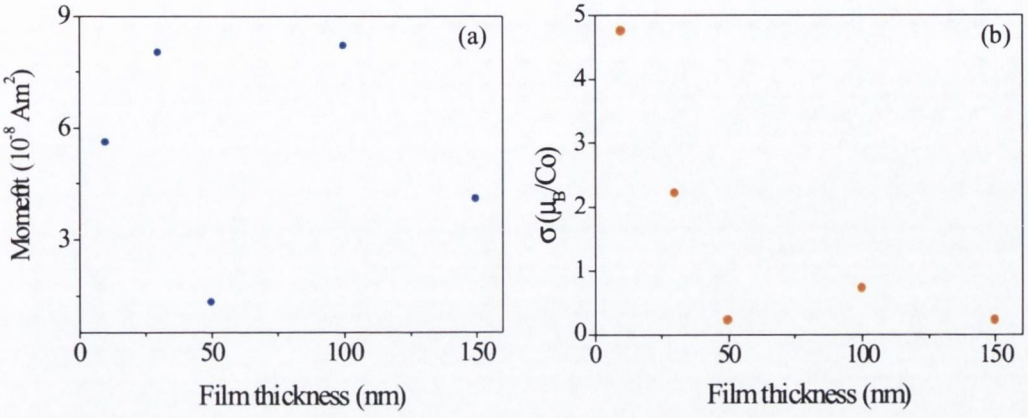


Figure 3.20 (a) The film moment plotted as a function of thickness and (b) the moment per cobalt atom plotted as a function of thickness in a $Sn_{0.81}Co_{0.19}O_2$ film

Figure 3.21a shows the magnetisation curves of a $Sn_{0.86}Fe_{0.14}O_2$ thin film at 5, 150, 300 and 400 K, where the saturation magnetisation remains almost constant. The Curie temperature obtained from a thermomagnetic scan in a field of 150 mT was 610 ± 10 K, as shown in figure 3.21b.

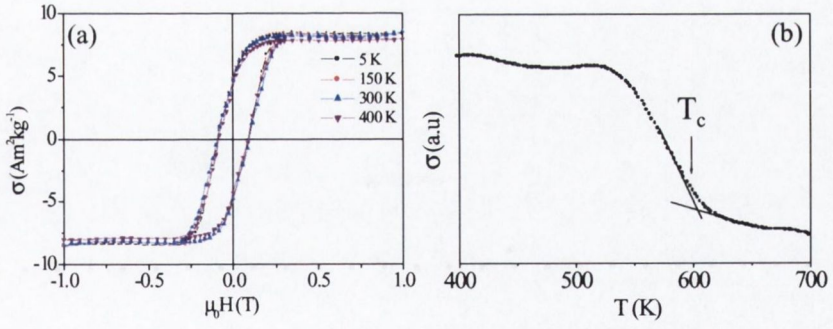


Figure 3.21 (a) Magnetisation curves at 5, 150, 300 and 400 K for a $Sn_{0.86}Fe_{0.14}O_2$ thin film and (b) the Curie temperature transition in the same film as measured in the SQUID

Figure 3.22a is an atomic force microscope image of a $Sn_{0.75}Fe_{0.25}O_2$ thin film, while (b) is a magnetic force microscope image of the same area, corrected for surface topology.

The magnetic contrast appears to decorate the topology, consistent with uniform in-plane magnetisation of the films.

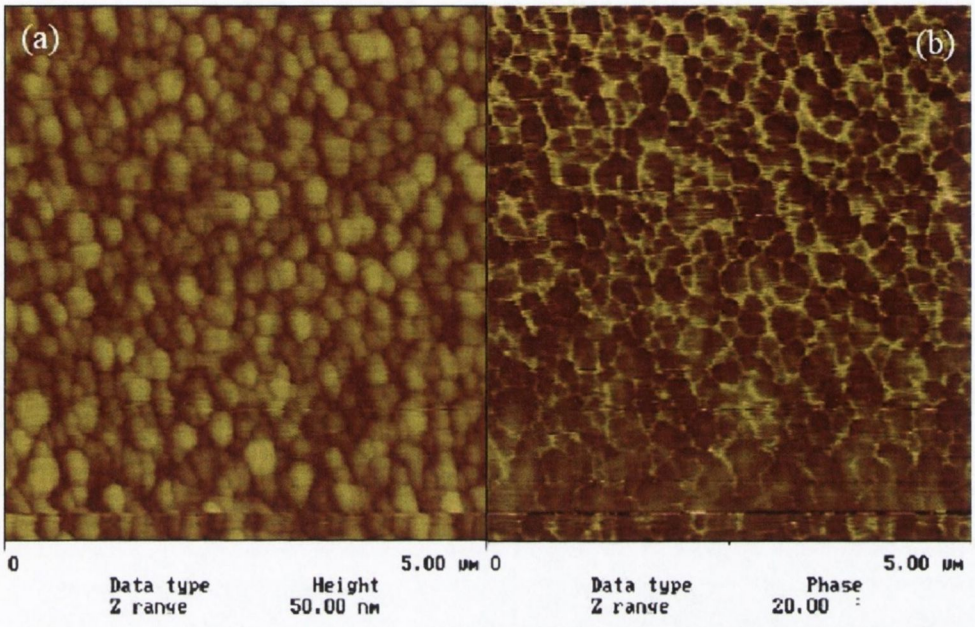


Figure 3.22 (a) Atomic force microscope image of a film of composition $Sn_{0.75}Fe_{0.25}O_2$ and (b) magnetic force microscope image of the same area corrected for surface topology

3.4 Indium-tin oxide (ITO)

In_2O_3 is a transparent $n-$type conducting oxide. It has a cubic structure and a direct bandgap of 3.75 eV. Films of In_2O_3 are superior to other transparent conductors, largely due to their high mobility - 10 - 75 $cm^2V^{-1}s^{-1}$ at a carrier density of $\sim$ 10 ^{19}- 10^{20} cm^{-3}. $In_{2-x}Sn_xO_3$ with varying Sn concentration has been well studied [6], and In_2O_3 with 5 - 10 wt. % of Sn concentration exhibits high carrier density, low resistivity and reasonable mobility [7]. A moment of 0.8 μ_B/Mn has recently been reported in 5 % Mn-doped ITO films [8].

An undoped ITO target was made by mixing 90 wt. % In_2O_3 and 10 wt. % SnO_2

powders, and two cobalt doped targets were made with 2 and 3 wt. % CoO substituted for SnO_2. The targets were sintered in the same as way as SnO_2 targets - for 24 hours in air at 1150 °C. Thin films were deposited on R-cut sapphire substrates at 400 °C. The films were highly conducting but did not exhibit any ferromagnetism.

3.5 Discussion

Similarly to Ogale et al [1] we have found giant magnetic moments per dopant atom in transition metal doped SnO_2. In figure 3.23 our data and theirs (orange points) are plotted together. However, they have found that their films are in a metastable state and that the moments diminish with time [9], unlike our films which are more stable.

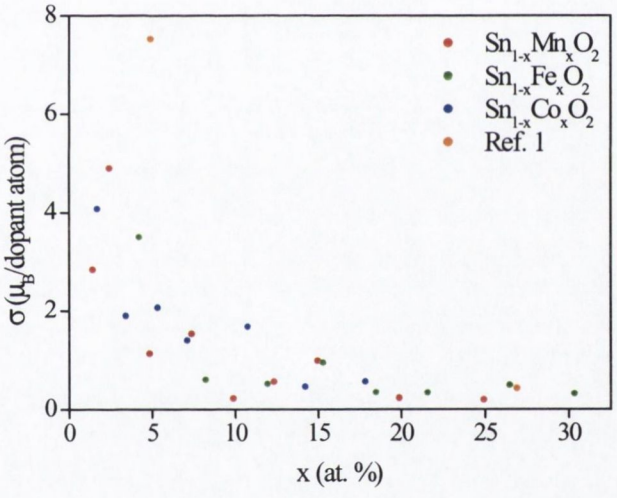


Figure 3.23 Magnetic moments per dopant atoms in $Sn_{1-x}M_xO_2$ (M = Mn, Fe, Co) with data from [1] included as orange points

No evidence of clustering or secondary phase formation has been found by x-ray diffraction, elemental mapping and energy dispersive analysis of x-rays on SEM or TEM equipment, or using Kennedy et als [5] method of plotting a log $\rho \sim T^{-\frac{1}{2}}$(or T^{-1} or $T^{-\frac{1}{4}}$) dependence, indicative of clustering or a multiphase system. Even if secondary phases are still present,

the low concentration moments that we have measured far exceed those of all known ferromagnetic phases (figure 3.17a). The pure metals Fe and Co have moments of 2.2 and 1.7 μ_B per atom, while we have found moments of up to 20 μ_B/Mn, 3.5 μ_B/Fe and 4.1 μ_B/Co. Of the possible ferromagnetic secondary phases listed in Table 8 of Chapter 1, most have low Curie temperatures ($T_c \sim 50$ K), but even γ-Fe_2O_3, with a Curie temperature of 743 K, has only a moment of 1.25 μ_B/Fe, while Fe_3O_4 clusters could not produce the hysteresis measured in the Fe-doped samples.

The upturn in moment at low concentrations in all three systems suggests that the high temperature ferromagnetism has an intrinisic origin - it is unlikely that ferromagnetic impurity phases would result in the same behaviour in the Mn, Fe and Co systems. However, the strongest evidence of intrinsic ferromagnetism in these films comes when their properties clearly differ from those of any conventional ferromagnetic material - in this case the moment per 3d cation which exceeds the spin only value, and the anisotropy of the magnetisation. No known room temperature ferromagnets approach this level of anisotropy at room temperature. Hysteresis observed at room temperature in Fe-doped films further supports the intrinsic ferromagnetic behaviour.

Some data suggests that lattice defects at the film/substrate interface may give rise to the observed ferromagnetism. When the magnetic moment is plotted as moment per unit substrate area versus x, figure 3.17b, the data extrapolates at $x = 0$ to a non-zero moment value of 150 - 200 μ_B nm^{-2}. There is no systematic concentration dependence of moment. The computational model fits the data well when an additional contribution from lattice defects is included. If lattice defects are involved, they may also be responsible for the anisotropy in the magnetisation. However, TEM studies have not yet revealed any interface

abnormalities.

High temperature ferromagnetism is not expected in oxide semiconductors with small amounts of 3d transition metal dopants because the magnetic doping level is below the cation percolation threshold x_p ($x_p = 0.25$ in the body-centred tetragonal rutile structure) needed for long-range order based on superexchange or double exchange interactions. If the ferromagnetism is intrinsic a new model is needed to explain it, where the carrier mediated ferromagnetic exchange interaction must also be effective whether or not the carriers are delocalised, given that Mn and Fe doped samples are ferromagnetic when they are conducting or insulating depending on x.

Before any model can be developed much more data is needed - are giant magnetic moments found in any other oxide systems? Do they exhibit the same levels of anisotropy in the magnetisation? What types of defects contribute to the ferromagnetism - oxygen vacancies? Lattice dislocations? As a preliminary test an undoped SnO_2 film was heated at 900 °C in air for 2 hours. After the heat treatment the film was no longer conducting, indicating that there had been oxygen vacancies present which were responsible for the films conductivity but that they had now been filled.

References

[1] S.B. Ogale, R.J. Choudhary, J.P. Buban, S.E. Lofland, S.R. Shinde, S.N. Kale, V.N. Kulkarni, J. Higgins, C. Lanci, J.R. Simpson, N.D. Browning, S. Das Sarma, H.D. Drew, R.L. Greene and T. Venkatesan, Phys. Rev. Lett. 91, 077205 (2003)

[2] H. Kimura et al, Appl. Phys. Lett., **80** 94 (2002)

[3] A. H. Morrish, Canted Antiferromagnetism: Haematite, Chap. 12, World Scientific, Singapore (1994)

[4] J. M. D. Coey, A. P. Douvalis, C. B. Fitzgerald and M. Venkatesan, Appl. Phys. Lett., **84** 1332 (2004)

[5] R. J. Kennedy, P. A. Stampe, E. Hu, P. Xiong, S. von Molnár and Y. Xin, Appl. Phys. Lett., **84** 2832 (2004)

[6] H. L. Hartnagel, A. L. Dawar, A. K. Jain and C. Jagadish, *Semiconducting Transparent Thin Films* (Institute of Physics, Bristol, U. K. 1995)

[7] V. Vasu and A. Subrahmanyam, Thin Solid Films, **193/194** 696 (1990)

[8] J. Philip, N. Theodoropoulou, G. Berera, J. S. Moodera and B. Satpati, Appl. Phys. Lett., **85** 777 (2004)

[9] M. S. Ramachandra Rao, S. Dhar, S. J. Welz, S. B. Ogale, D. C. Kundaliya, S. R. Shinde, S. E. Lofland, C. J. Metting, R. Erni, N. D. Browning and T. Venkatesan, cond-mat/0405378

Chapter 4

Transition metal doped ZnO

4.1 Introduction

ZnO is a wide, direct bandgap (3.35 eV) $n-$type semiconductor, but $p-$type conductivity has been successfully induced by co-doping Ga and N [1]. It has a hexagonal (wurtzite) crystal structure as shown in figure 4.1, with the $P6_3mc$ space group and lattice parameters $a = 3.25$ Å and $c = 5.12$ Å. The radius of the Zn^{2+} ion is 83 pm and that of O^{2-} is 135 pm. ZnO has a molecular weight of 81.37, a density of 5.61 gcm^{-3} and a melting point of 1975 °C. The powder is white and thin films are transparent.

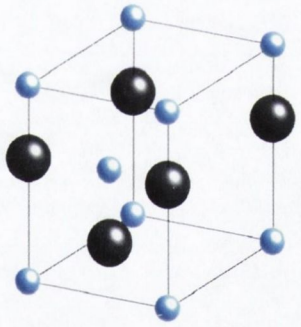


Figure 4.1 The hexagonal (wurtzite) crystal structure, with Zn atoms in blue and O atoms in black

Thin films of ZnO are generally grown on (0001) sapphire, due to the small lattice mismatch between film and substrate ($\sim$ 2 %), by RF magnetron sputtering, molecular beam epitaxy, pulsed laser deposition, metal-organic chemical vapour deposition or sol-gel methods, resulting in c-axis oriented films.

Dietl et al [2] predicted room temperature ferromagnetism in $p-$type ZnO doped with 5 % Mn (figure 1.13), and first principles calculations by Sato and Katayama-Yoshida [3]

showed that doping V, Cr, Fe, Co and Ni would lead to ferromagnetic ordering without any additional carrier doping. They also found that Ti and Cu doping would result in a paramagnetic state, while for Mn doping a ferromagnetic state was induced by hole doping.

Transition metal doped ZnO has been extensively studied experimentally, following the initial report in 2001 by Ueda et al [6], who found a moment of up to 2 μ_B/Co in $Zn_{0.9}Co_{0.1}O$ thin films, with a Curie temperature between 280 and 300 K. Figure 4.2 is a compendium of results from published data of the concentration dependence of ferromagnetic moments for V, Mn, Fe, Co and Ni doping in bulk and thin film forms. There is no discernible trend, with properties varying greatly for samples of the same nominal composition prepared by different methods or by different groups. High solubility limits have been reported for Mn (35 % [4]), Co (up to 40 % [5]) and Ni (25 % [6]) in ZnO depending on the growth conditions, but despite the high doping levels, a study of $Zn_{0.75}Co_{0.25}O$ films by Rode et al [7] revealed no evidence for phase segregation.

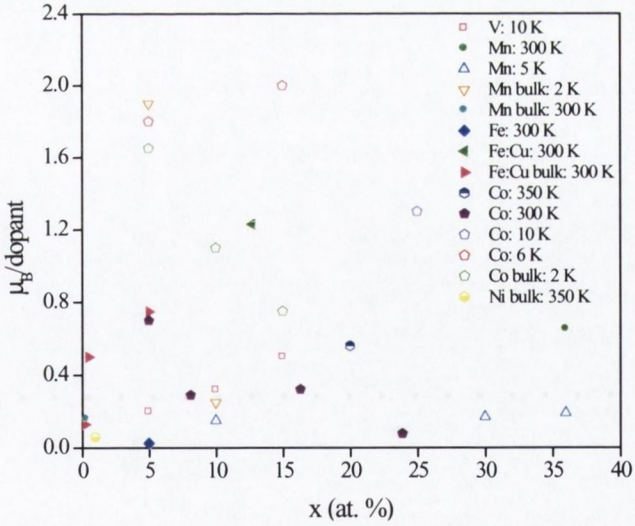


Figure 4.2 Magnetic moment per transition metal ion in V, Mn, Fe, Co and Ni doped ZnO

Curie temperatures above room temperature have been reported for a variety of 3d transition metal dopants - greater than 350 K in V [8] and Co [9] doped ZnO, greater than

room temperature for Mn [10] and Ni [11] doping and 550 K in Fe:Cu co-doped ZnO [12].

As with doped SnO_2, no clear connection between between the magnetic properties and electronic structure had been shown, and doubts that doped ZnO is truly intrinsically ferromagnetic persisted. While there have been many reports that Co-doped ZnO is ferromagnetic, Jin et al [13] found no indication of ferromagnetism in films grown by laser molecular beam epitaxy. Ueda et al [6] reported room temperature ferromagnetism in Co-doped ZnO films grown by pulsed laser deposition, however its reproducibility was less than 10 %. In order to probe the origin of high temperature ferromagnetism in $Zn_{1-x}M_xO$ we have examined the systematic variation of the magnetism i) as a function of transition metal concentration and film thickness for M = Co, ii) as a function of transition metal M at fixed concentration $x = 0.05$ and iii) as a function of oxygen pressure during film growth for $x = 0.05$ and M = Co.

4.2 Structure and composition

Ceramic $Zn_{1-x}M_xO$ targets were prepared from stoichiometric amounts of high purity (99.99 %) ZnO and MO or M_2O_3 powders. The oxide powders were ground under isopropanol for one hour, pressed into pellets and sintered at 900 °C for 12 hours in 0.5 bar of argon. Table 4.1 lists the compositions which were prepared.

x at. %	Sc	Ti	V	Cr	Mn	Fe	Co	Ni	Cu
1	×	×	×	×	×	×	✓	×	×
2	×	×	×	×	×	×	✓	×	×
3	×	×	×	×	×	×	✓	×	×
4	×	×	×	×	×	×	✓	×	×
5	✓	✓	✓	✓	✓	✓	✓	✓	✓
7.5	×	×	×	×	×	×	✓	×	×
10	×	×	×	×	×	×	✓	×	×
12.5	×	×	×	×	×	×	✓	×	×
15	×	×	×	×	×	×	✓	×	×

Table 1.List of transition metal doped ZnO targets produced by a solid state reaction technique

X-ray diffraction confirms the formation of the hexagonal (wurtzite) structure in all samples. Figure 4.3 shows the patterns of undoped ZnO and $Zn_{0.95}Co_{0.05}O$ powders, with the reflections indexed on the basis of the hexagonal wurzite unit cell. Energy dispersive x-ray analysis (EDAX) indicates that samples show the nominal transition metal concentration. XRD and EDAX both indicate that the targets are single phase materials.

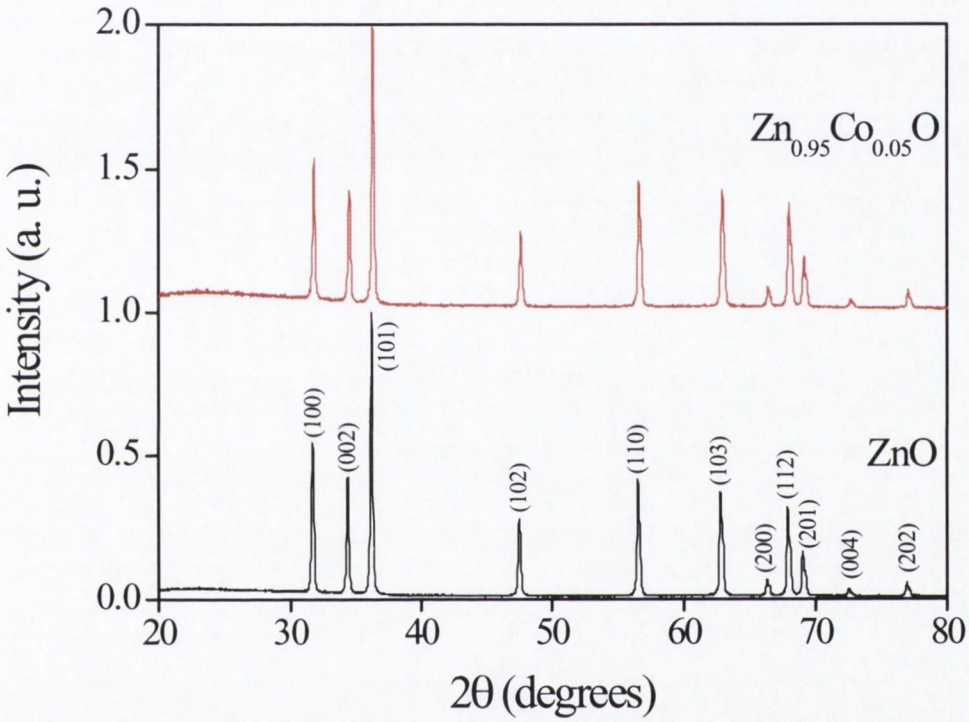


Figure 4.3 X-ray diffraction pattern of ZnO and $Zn_{0.95}Co_{0.05}O$ powders

The $Zn_{1-x}Co_xO$ ceramics are weakly magnetic, with a moment of 0.025 μ_B/Co for $Zn_{0.95}Co_{0.05}O$ as seen in figure 4.4a. Cobalt doped ZnO ceramics are conducting, with room temperature resistivity values $\sim$ 100 mΩcm. Figure 4.4b shows the resistivity curves of $Zn_{1-x}Co_xO$, $x = 0.05$, 0.10, 0.15, as a function of temperature.

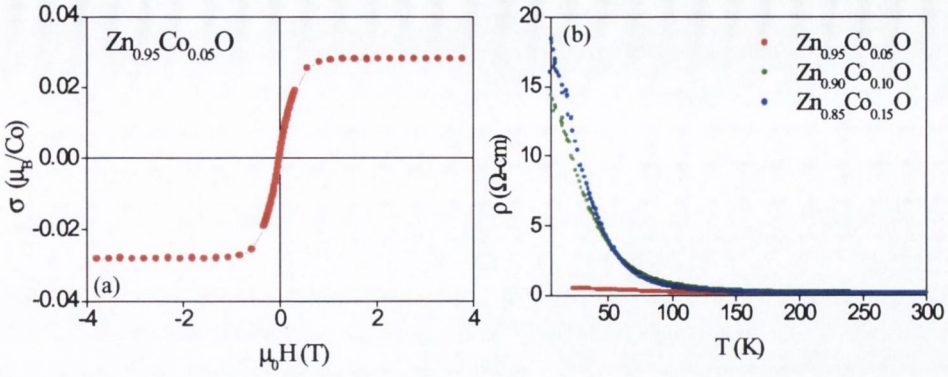


Figure 4.4 (a) The magnetisation curve of the $Zn_{0.95}Co_{0.05}O$ ceramic and (b) resistivity curves of $Zn_{1-x}Co_xO$ ceramics, $x = 0.05$, 0.10 and 0.15, as a function of temperature

4.3 Thin films

4.3.1 $Zn_{1-x}Co_xO$

Thin films of $Zn_{1-x}Co_xO$, $x = 0$ - 0.15, were deposited by PLD. They were grown on R-cut sapphire substrates at 600 °C in 1.10^{-4} mbar of oxygen with a 10 minute deposition time. In addition, a series of $Zn_{0.95}Co_{0.05}O$ films were grown with deposition times of 1, 3, 5, 10 and 15 minutes, with a deposition rate of approximately 40 nm/minute. ZnO and $Zn_{0.95}Co_{0.05}O$ films were also grown in a range of oxygen pressures - 0.1, 0.5, 1, 10, 100 and 1000 μbar of oxygen - with 10 minute deposition times.

The undoped samples are transparent, while Co doping results in a green tinge which becomes more pronounced at higher doping levels. The film compositions were determined by EDAX analysis for films prepared from targets with nominal composition x' as shown in figure 4.5a. The relationship between x' and x is almost linear, with x being about 30 % greater than x'. As with doped SnO_2, PLD does not maintain the stoichiometry of the targets but their substitution is better than for SnO_2 because the melting point of host and

dopant are closer. The effect of repeated depositions from the same $Zn_{0.95}Co_{0.05}O$ target and different deposition times, figure 4.5b (orange), and oxygen pressure during deposition, figure 4.5b (green), on x was also examined. x is relatively invariant with deposition time and repeated depositions, but varies considerably with different oxygen pressures.

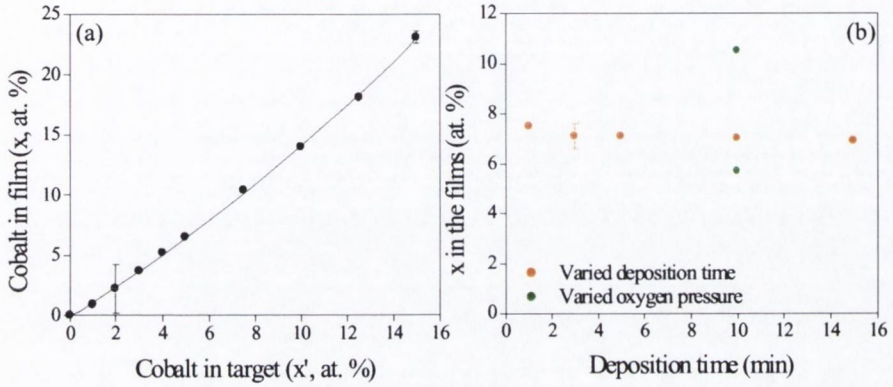


Figure 4.5 (a) A plot of x as measured in the films versus x', the nominal target value and (b) the variation of x with deposition time (orange) and oxygen pressure (green) from a $Zn_{0.95}Co_{0.05}O$ target

The x-ray diffraction patterns show the wurtzite films to be single phase and well-oriented with a (110) texture. Figure 4.6 is the diffraction pattern of ceramic $Zn_{0.95}Co_{0.05}O$ and a corresponding thin film, where 'S' indicates substrate peaks.

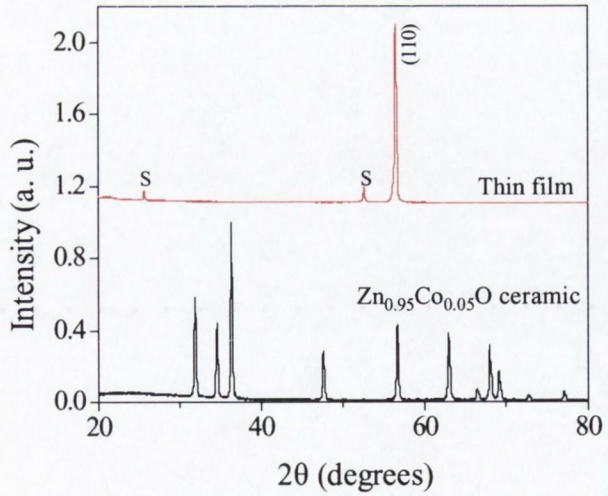


Figure 4.6 X-ray diffraction pattern of a $Zn_{0.95}Co_{0.05}O$ ceramic target and a corresponding thin film.

The position of the 110 reflection was examined as a function of cobalt concentration x

(figure 4.7a), film thickness (figure 4.7b) and the oxygen pressure during deposition (figure 4.7c). All three plots are shown on the same scale for clarity, and the solid line indicates the d position of the (110) peak measured in the pure ZnO powder used to make the ceramics.

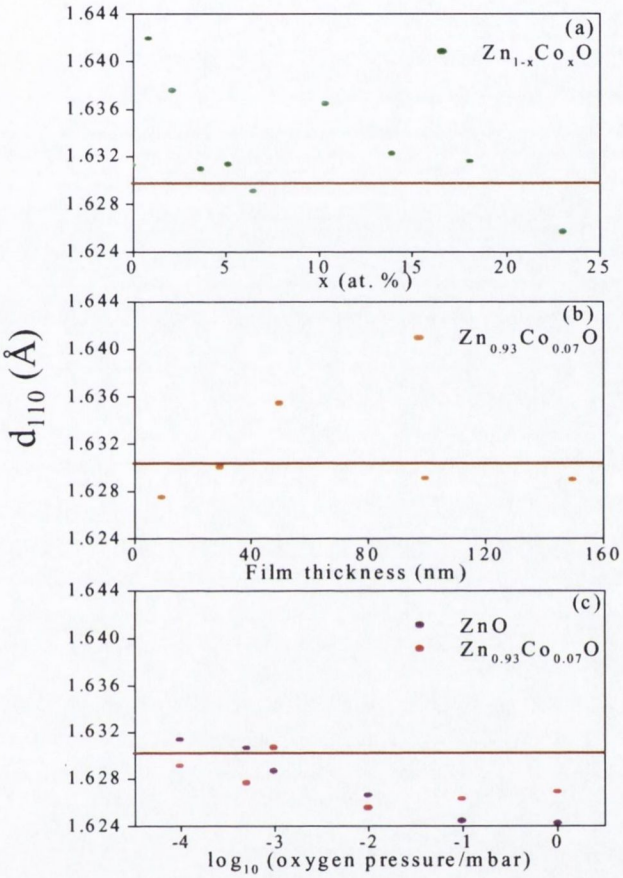


Figure 4.7 The d_{110} lattice spacing in $Zn_{1-x}Co_xO$ films as a function of (a) x, (b) film thickness and (c) oxygen pressure during deposition. In all cases the solid line is the d_{110} position in pure ZnO powder

The 'd' position of the (110) peak (d_{110}) in the ZnO film is close to that of the pure powder as shown in figure 4.7a. Much of the data for Co doped ZnO is also close to the bulk value, although there is a slight decrease in d_{110} with increasing x and the values for x < 4 % are high. The Zn^{2+} ion, with a radius of 83 pm, is practically the same size as the Co^{2+} ion at 82 pm, and so a little lattice contraction can be expected with Co substitution.

The cobalt is almost certainly in the 2+ state, as the Co^{3+} ion has a radius of 64 pm, which should lead to much more pronounced lattice strain.

The value of d_{110} in $Zn_{0.93}Co_{0.07}O$ films, figure 4.7b, is close to that of bulk ZnO suggesting little strain in the films, and is relatively invariant with thickness. In figure 4.7c d_{110} decreases with increasing oxygen pressure during deposition in both the ZnO and $Zn_{0.93}Co_{0.07}O$ film series. Films produced at low pressures are closest to the bulk value, while zinc deficiency at higher pressures strains the films.

The thicknesses of the ZnO films were determined using in-situ reflectivity equipment (4.8a and b) and small angle x-ray reflectivity (4.8c). Figure 4.8a illustrates the calculated reflectivity curve for ZnO while 4.8b is data recorded during the growth of a $Zn_{0.93}Co_{0.07}O$ film. The film in 4.8b was deposited under normal conditions for 15 minutes as part of the series of films grown with different deposition times. It is approximately 640 nm thick, indicating a growth rate of $\sim$ 43 nm a minute. The film grown with a three minute deposition time was found to be 125 nm thick, growing at a rate of 42 nm a minute and similar deposition rates were obtained for the other films - the deposition rate is unaffected by deposition time.

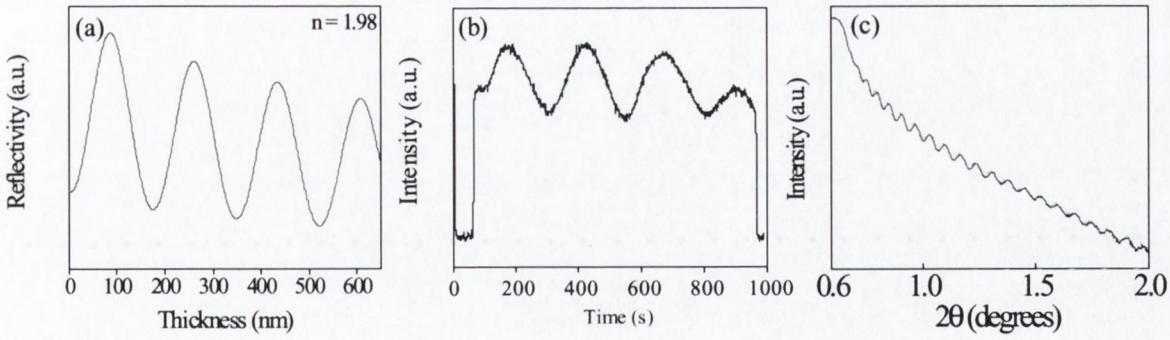


Figure 4.8 (a) Calculated reflectivity curve for ZnO growth, (b) reflectivity data recorded during a 15 minute deposition of a $Zn_{0.93}Co_{0.07}O$ film, which is $\sim$ 640 nm thick and (c) a typical small angle x-ray reflectivity plot of an 80 nm thick film

Optical transmission spectra for $Zn_{1-x}Co_xO$ (x = 0, 0.07, 0.14, 0.23) thin films are

compared in figure 4.9. The band edge appears at 3.27 eV in the undoped sample, while the band edge of the doped samples shift to progressively lower energies with x - the well known Moss-Burstein effect [14][15]. The red shift with increasing cobalt content could be attributed to the $sp-d$ exchange interactions between the band electrons and the localized d electrons of the Co^{2+} ions [16]. Also, as the cobalt content increases, so does the absorption band intensity. Transitions seen in the spectra of the cobalt-doped samples at 1.88, 2.04 and 2.2 eV have long been identified with $d-d$ absorption levels of Co^{2+} ions in tetrahedral oxygen coordination [17][18], assigned as $^4A_2 \longrightarrow {}^2E\ (^2G)$ and $^4A_2 \longrightarrow {}^4T_1(^4P)$ transitions.

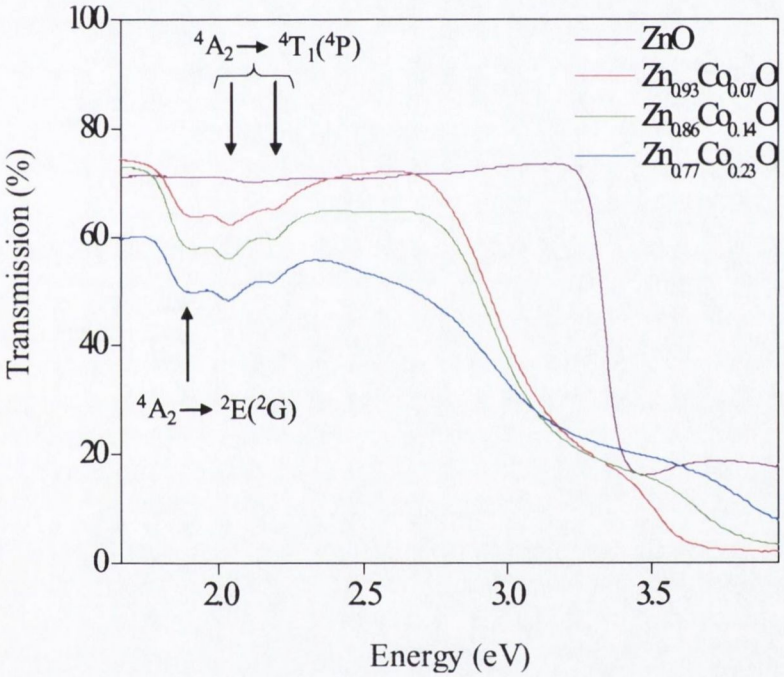


Figure 4.9 Optical transmission spectra of $Zn_{1-x}Co_xO$ (x = 0, 0.07, 0.14 and 0.23) thin films that are approximately 180 nm thick

In figure 4.10 the transmission spectra of ZnO (a) and $Zn_{0.93}Co_{0.07}O$ (b) films grown in different oxygen pressures are shown. There is little variation in the behaviour of the ZnO films with oxygen pressure - the band edge is static and sharp, with the only unusual feature being a drop in the transmission of the film grown at the highest oxygen pressure

(1000 μbar). In figure 4.10b the spectrum of the ZnO film grown in 0.1 μbar of oxygen is also plotted for comparison. The transitions due to Co^{2+} ions are most pronounced in the film grown in 10 μbar of oxygen, and its band edge is sharply shifted to a lower energy than the pure sample. In all other cases the band edge is quite diffuse and is shifted to higher energies than the undoped sample.

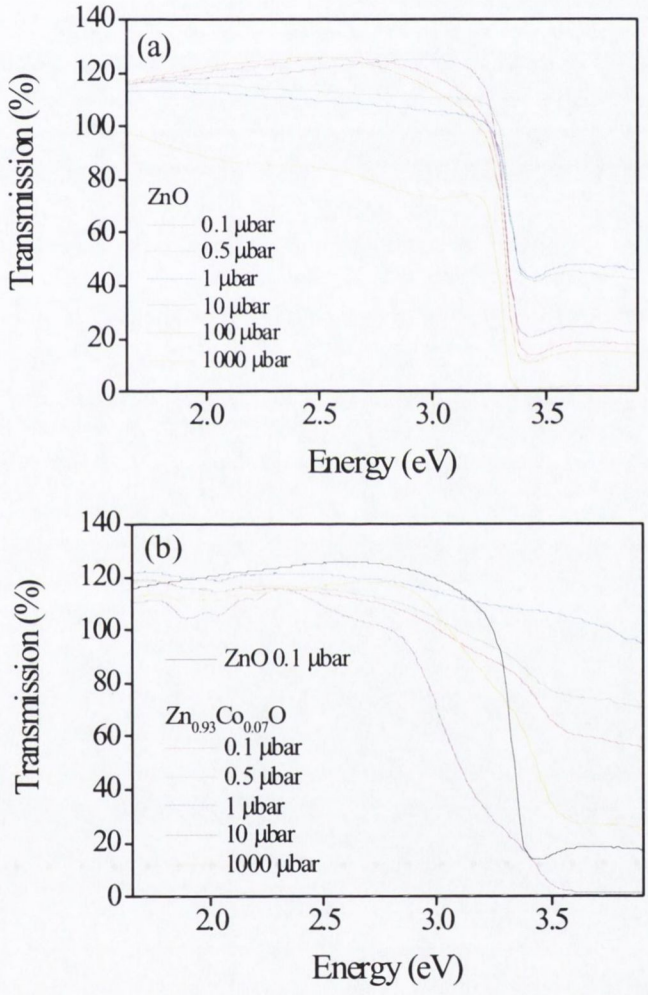


Figure 4.10 Optical transmission spectra of (a) ZnO and (b) $Zn_{0.93}Co_{0.07}O$ films grown at different oxygen pressures

All pure ZnO films are conducting, although there is a 100-fold increase in resistance

between films deposited at 1.10^{-4} mbar and 1 mbar of oxygen. Cobalt doped ZnO films are conducting for all values of x and films grown from a $Zn_{0.95}Co_{0.05}O$ target are conducting when deposited in less than 100 μbar of oxygen.

Room temperature resistivity values for samples grown at 1.10^{-4} mbar vary from 10 mΩcm for the undoped sample to 117 Ωcm when $x = 0.07$ and 279 Ωcm when $x = 0.14$ as shown in figure 4.11a. Resistivity was also plotted on a logarithmic scale versus $T^{-\frac{1}{2}}$ in figure 4.11b as with the $Sn_{1-x}Co_xO_2$ data. While in this case resistivity does seem to follow a $\log \rho \sim T^{-\frac{1}{2}}$ dependence, it occurs in all samples - including the undoped film. In cannot, therefore, be interpreted in terms of cobalt clusters in the films.

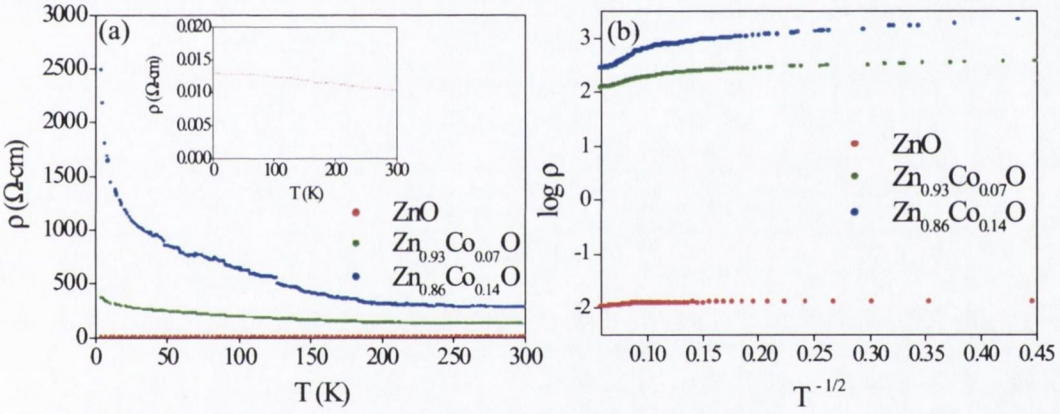


Figure 4.11 Resistivity of the $Zn_{1-x}Co_xO$ series (a) resistivity ρ vs temperature, with the undoped ZnO film shown in the insert on an expanded scale and (b) on a log ρ vs $(1/T)^{1/2}$

All cobalt-doped ZnO films are ferromagnetic at room temperature, with coercivity of 2 - 3 mT. Figure 4.12a shows the variation of the cobalt moment as a function of x for films grown in 1.10^{-4} mbar of oxygen. The largest moment measured is 5.9 μ_B/Co compared to the spin-only moment $m_{spin} = 3\ \mu_B$ of high-spin Co^{2+}. Figure 4.12b shows the moment plotted per unit substrate area, and as with doped SnO_2, it extrapolates to a non-zero value of 150 - 200 μ_B nm^{-2}, which may be the result of interface defects.

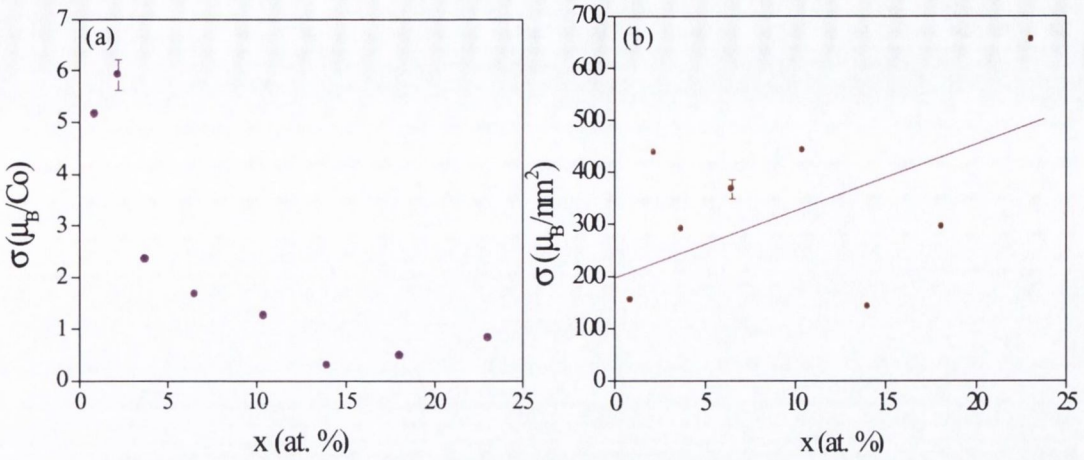


Figure 4.12 (a) The average cobalt moment at room temperature versus x and (b) the magnetic moment per unit substrate area versus x

Again, similar to doped SnO_2, the moment drops as x increases, which can be understood in terms of a random distribution of cobalt ions over the cation sites in the wurtzite lattice. Isolated ions contribute the full moment, pairs and most groups of four are antiferromagnetically coupled and make no net contribution, triplets contribute $m_{spin}/3$. Large antiferromagnetically-coupled clusters of N atoms will make a contribution of $m_{spin}/\sqrt{N}$. The program used is described in chapter 3, and modified for a hexagonal crystal structure.

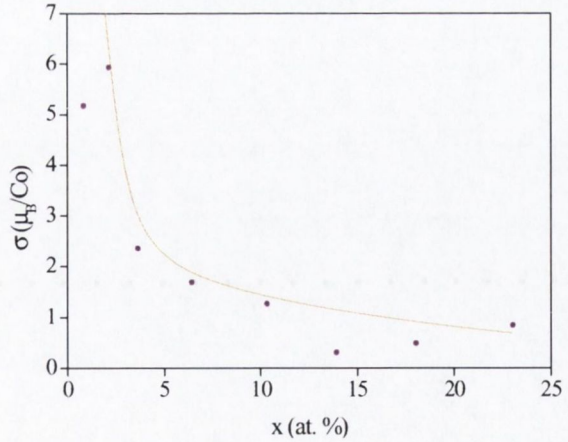


Figure 4.13 The moment per cobalt atom as a function of x with the fit from the model described above shown as a solid line

Figure 4.13 shows the moment per cobalt as a function of x with the program fit

overlaid as a solid line. In this case $a = 5$, and a moment of $m_{spin} = 3\ \mu_B$ is used plus an additional constant contribution of 200 μ_B nm^{-2} from the interface defects. The model fits the data well.

The moment per cobalt atom in $Zn_{0.93}Co_{0.07}O$ films is plotted as a function of film thickness in figure 4.14a. The moment per cobalt atom decreases with increasing film thickness, but the moment of the film (4.14b) is relatively unaffected by thickness. Figure 4.14c plots the Co moment as a function of oxygen pressure during deposition, assuming a constant value of $x = 0.07$, and drops almost linearly with increasing oxygen pressures.

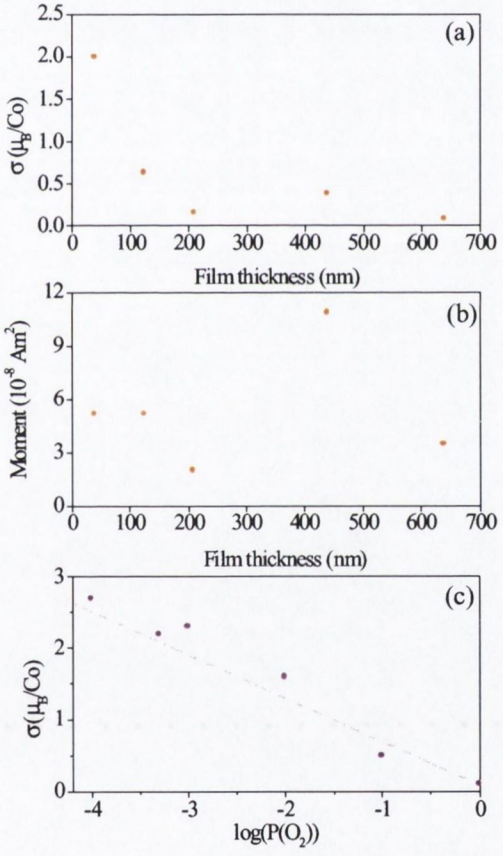


Figure 4.14 (a) The moment per cobalt atom in $Zn_{0.93}Co_{0.07}O$ thin films plotted as a function of film thickness, (b) the film moment as a function of thickness and (c) the moment per cobalt atom as a function of the oxygen pressure during deposition

Measurements of the anisotropy of the magnetisation were made, with the films mounted

parallel or perpendicular to the field in the SQUID magnetometer. The results for a $Zn_{0.93}Co_{0.07}O$ thin film deposited at 1.10^{-4} mbar of oxygen for 10 minutes is shown in figure 4.15. In this case the moment is largest in the parallel direction (orange), unlike cobalt-doped SnO_2 where it was greatest in the perpendicular direction.

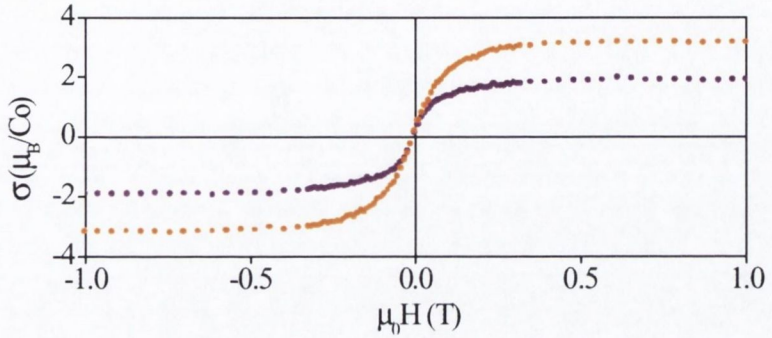


Figure 4.15 Anisotropy of the magnetisation in a $Zn_{0.93}Co_{0.07}O$ thin film. Purple indicates measurements made perpendicular to the substrate and orange indicates parallel to the substrate

Finally, the $Zn_{0.93}Co_{0.07}O$ thin film deposited in 1 mbar of oxygen was heated to 700 °C in vacuum. Figure 4.16 shows its magnetisation curves before and after the heat treatment. The moment more than doubles with the treatment, suggesting that ferromagnetism may be related to oxygen vacancies.

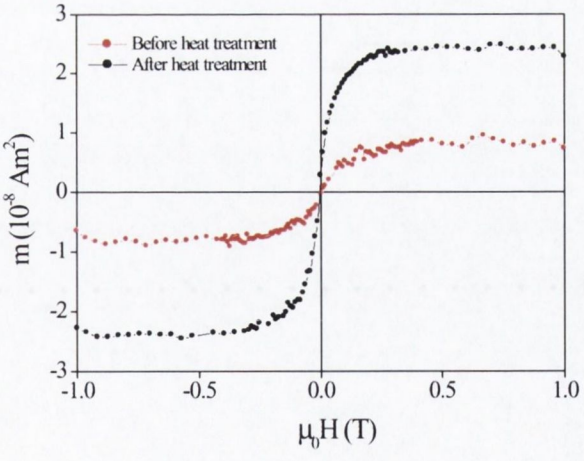


Figure 4.16 Magnetisation curves of the $Zn_{0.93}Co_{0.07}O$ film deposited in 1 mbar of oxygen before and after a post-deposition heat treatment

4.3.2 $Zn_{1-x}M_xO$, M = Sc - Cu

Thin films were deposited by PLD from the $Zn_{0.95}M_{0.05}O$ ceramic targets where M = Sc, Ti, V, Cr, Mn, Fe, Co, Ni, Cu and Zn. As with the cobalt doped films above, they were grown on R-cut sapphire substrates at 600 °C in 1.10^{-4} mbar of oxygen with a ten minute deposition time. Films were $\sim$ 80 nm thick. The Mn-doped film has a bright yellow/orange colour, and the Co-doped sample is green. The film compositions were determined by EDAX analysis as shown in figure 4.17. There is a very large scatter, with $x = 0.18$ measured in the Ti-doped film, and $x < 0.01$ in the Cu-doped film (EDAX analysis confirmed the nominal Cu content in the target).

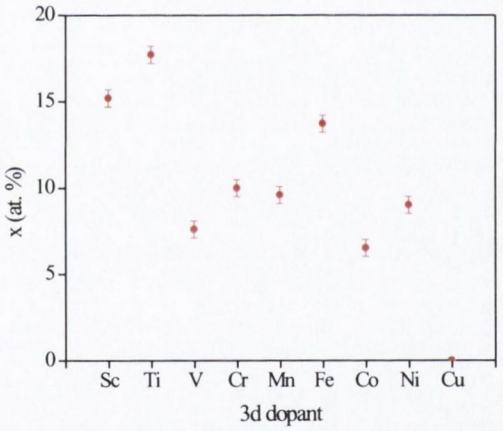


Figure 4.17 The concentration x of transition metal atoms (M) in films grown from $Zn_{0.95}M_{0.05}O$ ceramic targets

X-ray diffraction patterns again confirm a strong (110) texture. The lattice spacing of the 110 reflection (d_{110}) is plotted for each transition metal dopant in figure 4.18, with the powder ZnO value shown as an orange line and the undoped ZnO film value as a navy line. d_{110} for dopants at the beginning of the series (Sc, Ti and V) are quite low, the Mn value is very high and towards the end of the series (Fe, Co, Ni and Cu) values are a little low, but

close to the powder value.

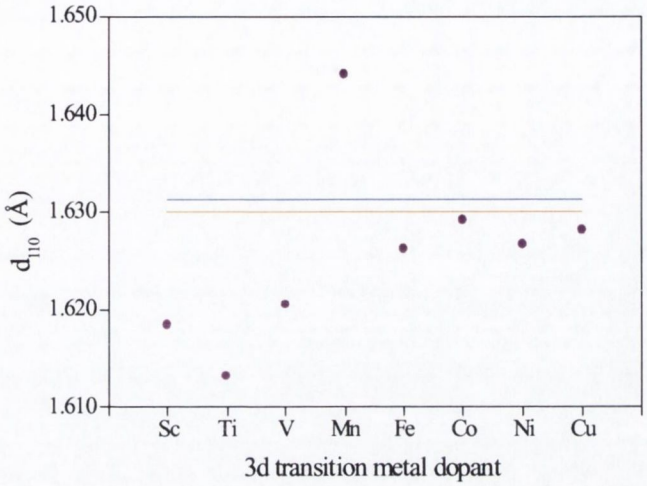


Figure 4.18 d_{110} in $Zn_{1-x}M_xO$ thin films as a function of transition metal dopant. The powder value is shown as an orange line, and the pure ZnO film value is marked with a navy line

The ionic radii of the $3d$ transition metal ions is listed in Table 2 for different charge states. The Sc^{3+} ion has a radius of 83 pm, the same as the Zn^{2+} ion, and so its substitution is not expected to distort the ZnO lattice. However, even though the doping level is high ($x \sim 0.15$) the d_{110} value of the $Zn_{0.85}Sc_{0.15}O$ film is low, suggesting some strain in the film.

	Sc	**Ti**	**V**	**Mn**	**Fe**	**Co**	**Ni**	**Cu**	**Zn**
1+								96	
2+		80	72	91	82	82	78	72	83
3+	83	69	65	70	67	64	62		
4+			61	52					
5+			59						

Table 2.Ionic radii in pm of transition metals with different charge states

The Ti^{2+} ion is unstable, and so Ti is almost certainly in the 3+ (69 pm) charge state. The d position of the 110 reflection is low for the Ti-doped film, because the Ti^{3+} ion is much smaller than Zn^{2+}, and with $x \sim 0.18$ there is considerable lattice contraction. The vanadium ion charge states range from 2+ to 5+. d_{110} is again low, and probably due to

a slightly smaller ion (V^{3+}- V^{2+} is also unstable) substituting on the Zn sites. The effect is less pronounced than for Ti doping as the doping level is much lower ($x \sim 0.08$). d_{110} is very high for Mn-doping, consistent with Mn taking the 2+ charge state (radius Mn^{2+} > radius Zn^{2+}) and a relatively high doping level ($x \sim 0.10$). d_{110} is quite close, if a little low, compared to the ZnO powder value for Fe-doping despite the high doping levels ($x \sim 0.14$) suggesting it takes the 2+ charge state, which is marginally smaller than the Zn^{2+} ion. Cobalt is almost certainly in the 2+ state, with d_{110} very close to the powder ZnO value, and a moderate doping level ($x \sim 0.07$). The Ni d_{110} value is a little low with $x \sim 0.09$, and so the ion is probably Ni^{2+}. The charge state on the Cu ion is probably 2+ with a radius of 72 pm as the d_{110} value is just a little smaller than the powder and undoped film values for ZnO, and the lattice distortion is consistent with a small amount of Cu in the film.

ZnO films doped with Sc, Mn, Co, Ni and Cu are conducting, while Ti, V, Cr and Fe doped films are insulating. However, a V-doped ZnO film grown on R-cut sapphire with a thin ($\sim$ 10 nm) ZnO buffer layer is conducting.

Figure 4.19 shows the transmission spectra for the transition metal doped ZnO films. The band edge of the undoped sample appears at 3.27 eV, with the band edge of the Ni-doped film following it closely. The band edges of the Sc, Fe, Co, Mn, V and Ti doped films move to progressively larger energies, while the band edge in the Cu-doped film appears earlier than the pure ZnO films, at about 3.23 eV. Transmission is greatest in the Fe, Co, Ni and Sc-doped samples, and is less than 80 % in all other films. In the case of Ni, and to a smaller extent Co, the transmission exceeds 100 %. This is most likely due to a measurement or alignment error, but it is possible that the film could act as an anti-reflective coating, increasing transmission.

While clear transitions are seen in the $Zn_{1-x}Co_xO$ optical spectra (figure 4.9), nothing quite so obvious is seen here, although these films are considerably thinner. The V, Cr, Mn, Co and Ni doped films all have steadily decreasing transmission in the approach to the band edge, unlike the other films, which approach the edge with almost constant transmission values.

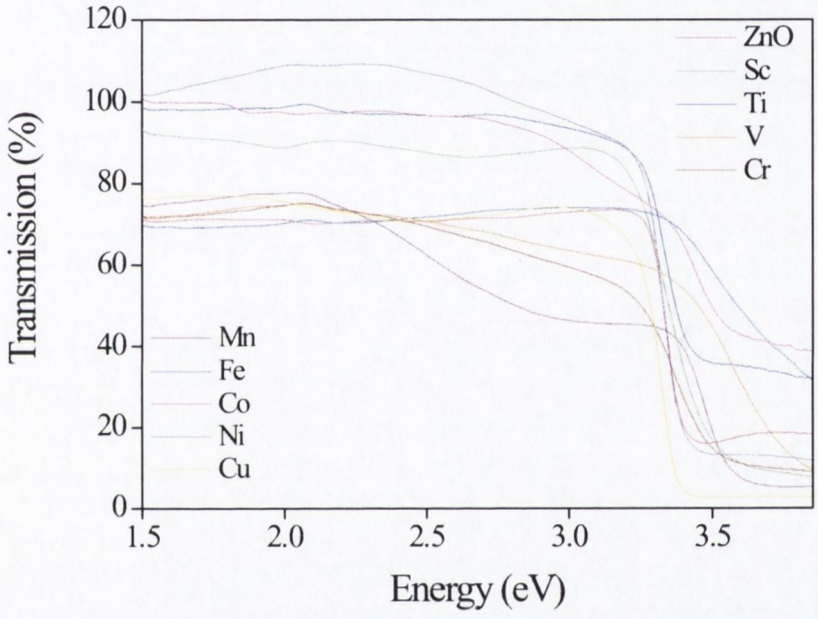


Figure 4.19 The transmission spectra of transition metal doped ZnO films

The variation of the magnetic moment across the transition-metal doped ZnO series is illustrated in figure 4.20, for both the perpendicular (purple) and parallel (orange) directions at room temperature. There are maxima at the beginning of the $3d$ series at Ti and V, and towards the end of the series at Co. No moment greater than the experimental uncertainty ($< 0.1\ \mu_B$) was observed for Cr, Mn and Cu.

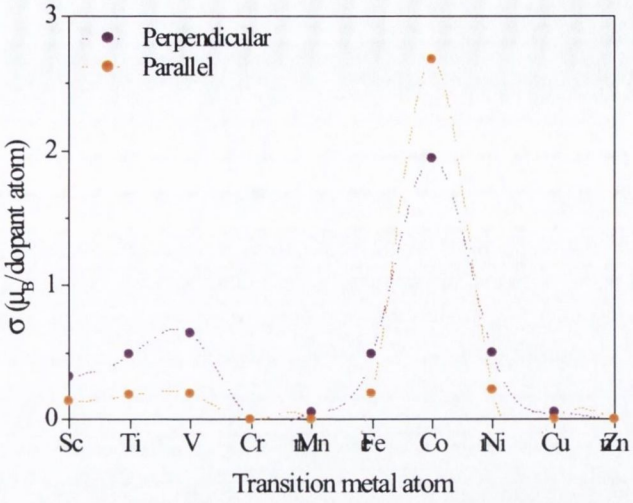


Figure 4.20 The variation of the magnetic moment across the transition-metal doped ZnO series as measured in the perpendicular (purple) and parallel (orange) directions

All transition metal doped ZnO films are ferromagnetic at room temperature with the exception of Cr, Mn and Cu. The magnetisation is greatest when measured in the perpendicular direction for all films except Co-doped ZnO (figure 4.15). Figure 4.21 illustrates the anisotropy of the magnetisation in Sc and V-doped ZnO films.

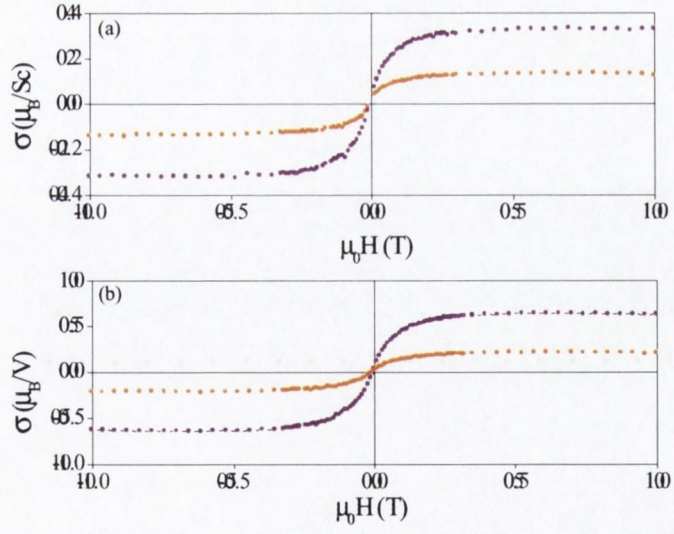


Figure 4.21 Anisotropy of the magnetisation in (a) Sc-doped and (b) V-doped ZnO films with purple indicating measurements in the perpendicular direction and orange the parallel direction

ZnO films on R-cut sapphire show an enormous in-plane anisotropy, with two- and

four-fold symmetry. The moment per cobalt for the $Zn_{0.93}Co_{0.07}O$ film is 1.9 μ_B when the field is applied perpendicular to the plane of the film, but it varies from 2.6 to 0.8 μ_B in the plane, with the largest value measured with the field parallel to the edge of the substrate, and the smallest along a diagonal which coincides with the c-axis of ZnO films - figure 4.22. The ZnO c-axis lies parallel to the substrate [12$\bar{1}$] axis [19].

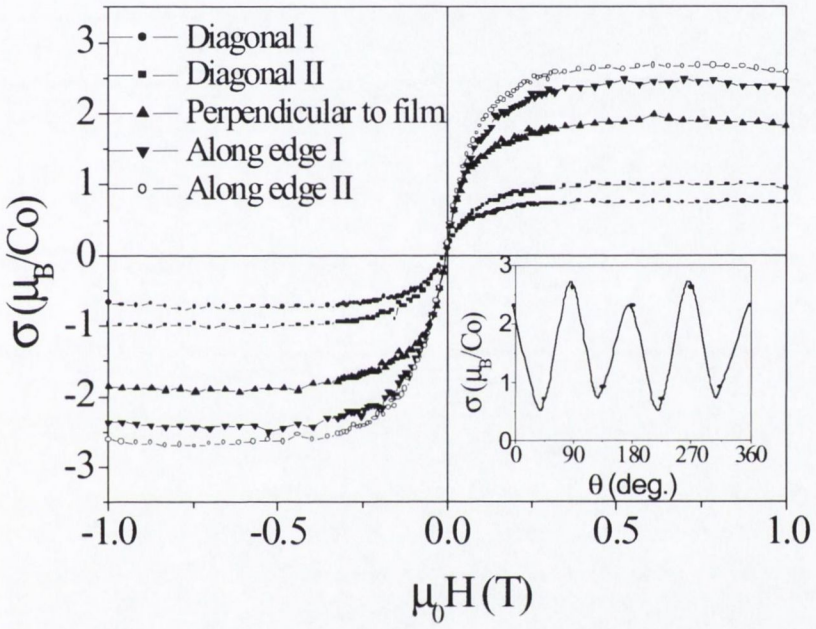


Figure 4.22 Magnetization curves of a $Zn_{0.93}Co_{0.07}O$ film with the magnetic field applied perpendicular to the plane of the film, or in-plane in different directions. The in-plane anisotropy is shown in the insert.

4.3.3 Multilayer structures

A $Zn_{0.93}Co_{0.07}O$ (10 nm)/ZnO (10nm)/ $Zn_{0.93}Co_{0.07}O$ (40 nm) multilayer structure was grown on an R-cut sapphire substrate as illustrated in figure 4.23a. Figure 4.23b shows its magnetisation curve where only a small coercivity of 2 mT was found instead of two phases with different coercivities arising from differing thicknesses of the $Zn_{0.93}Co_{0.07}O$ layers.

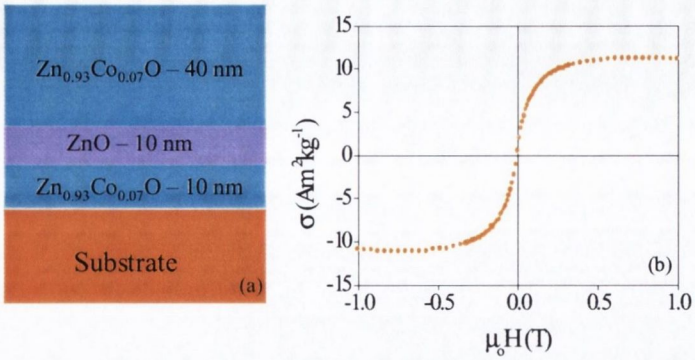


Figure 4.23 (a) A $Zn_{0.93}Co_{0.07}O$ (10 nm)/ZnO (10nm)/ $Zn_{0.93}Co_{0.07}O$ (40 nm) multilayer structure grown on a sapphire substrate and (b) its magnetisation curve

4.4 Discussion

Although no secondary phases have been observed by XRD or EDAX mapping, the strongest evidence that transition metal doped ZnO is a homogeneous and single phase material comes from optical transmission spectra of Co-doped ZnO films. The spectra show that cobalt enters the ZnO structure as Co^{2+} rather than forming metallic clusters.

In many ways, the data for Co-doped ZnO echoes the results from the SnO_2 chapter. In both cases:

1. The moment per dopant atom at low concentrations exceeds the spin-only moment
2. The moment falls quickly as x increases (or approaches the percolation threshold)
3. If the moment is plotted per unit substrate area it extrapolates to a non-zero value, 150 - 200 $\mu_B \mathrm{nm}^{-2}$
4. The moment is relatively unaffected by film thickness
5. The magnetisation curves exhibit large and unexpected anisotropy

So we now know that giant magnetic moments and anisotropy are not limited to doped SnO_2. To further our understanding of the behaviour of these materials $Zn_{0.93}Co_{0.07}O$ films were grown in oxygen pressures ranging from 0.1 μbar to 1000 μbar. It has been reported

that carriers in ZnO are associated with oxygen vacancies or interstitial zinc atoms [20][21], and we found some evidence to support this - we found that the moment dropped and the films became insulating as the oxygen pressure was increased - that the ferromagnetism is destroyed as the carriers and their associated defects are eliminated. Heating the $Zn_{0.93}Co_{0.07}O$ film deposited in 1 mbar film at 700 ° C in vacuum leads to an increase in moment.

However, more questions are raised when ZnO is doped with atoms from across the transition metal series - ferromagnetism is observed in Sc-doped ZnO. Neither Zn^{2+} ($3d^{10}$) or Sc^{3+} ($3d^{0}$) are magnetic ions, and the 3d level of zinc lies well below that of scandium [22] and so no electron transfer to scandium is envisaged. Although we now have a new phenomenon, it may support the theory that interface defects play a part in producing the ferromagnetism in these materials. Undoped SnO_2 and ZnO films are not ferromagnetic, but perhaps doping with particular, not necessarily magnetic, ions allow the defects to be 'switched on'. However, the nature of these defects is still unclear. Oxygen vacancies may trap one or two electrons, forming F^+ or F centres respectively. Calculations by Monnier and Delley [23] illustrated that a neutral B_6 vacancy could develop a moment of 2.4 μ_B/vacancy. Divalent cations replace zinc, but trivalent ones act as electron dopants or else create zinc vacancies (V^o centres). A calculation by Elfimov et al [24] for CaO gives some insight into how the moment associated with a lattice defect arises. They show that a neutral Ca vacancy leads to compensating holes on the surrounding oxygen atoms and demonstrate that these cation vacancies order ferromagnetically.

Another question arises from the anisotropy in the magnetisation of the Co-doped films - why are they the only ones to have the greatest moment when measured in the parallel, rather than perpendicular, direction?

Dietl [2] and Sato and Katayama-Yoshida [3] had predicted ferromagnetic ordering in V, Cr, Mn, Fe, Co and Ni doped ZnO, and that Ti and Cu doping would result in a paramagnetic state. We have found that Ti doping produces ferromagnetic ordering, but that Cr, Mn ($<$ 0.01 μ_B) and Cu doping do not. Their calculations fail to take into account the effects of interface defects.

References

[1] M. Joseph, H. Tabata and T. Kawai, Jpn. J. Appl. Phys., Part 2 **38** L2505 (1999)

[2] T. Dietl, A. Haury and Y. Merle d'Aubigné, Phys. Rev. B **55** R3347 (1997)

[3] K. Sato and H. Katayama-Yoshida, Jap. J. Appl. Phys., **39** L555 (2000)

[4] T. Fukumura, Z. Jin, A. Ohtomo and H. Koinuma, Appl. Phys. Lett. **75** 3366 (1999)

[5] J. H. Kim, H. Kim, D. Kim, Y. E. Ihm and W. K. Choo, Physica B **327** 304 (2003)

[6] K. Ueda, H. Tabata and T. Kawai, Appl. Phys. Lett., **79** 988 (2001)

[7] K. Rode, A. Anane, R. Mattana et al, J. Appl. Phys. 93 7676 (2003)

[8] H. Saeki, H. Tabata and T. Kawai, Solid State Commun., **120** 439 (2001)

[9] H. J. Lee, S. Y. Jeong, C. R. Cho and C. H. Park, Appl. Phys. Lett., **81** 4020 (2002)

[10] T. Fukumura, Z. Jin, M. Kawasaki, T. Shono, T. Hasegawa, S. Koshihara and H. Koinuma, Appl. Phys. Lett., **78** 958 (2001)

[11] P. V. Radovanovic and D.R. Gamelin, Phys. Rev. Lett. 91 157202 (2003)

[12] S. J. Han, J. W. Song, C. H. Yang, S. H. Park, J. H. Park, Y. H. Jeong and K. W. Rhie, Appl. Phys. Lett., **81** 4212 (2002)

[13] Z. Jin, T. Fukumura, M. Kawasaki, K. Ando, H. Saito, T. Sekiguchi, Y. Z. Yoo, M. Murakami, Y. Matsumoto, T. Hasegawa and H. Koinuma, Appl. Phys. Lett., **78** 3824 (2001)

[14] E. Burstein

[15] K. J. Kim and Y. R. Park, Appl. Phys. Lett., **81** 1420 (2002)

[16] J. Diouri, J. P. Lascaray and M. El Amrani, Phys. Rev. B 31 7995 (1985)

[17] P. Koidl, Phys. Rev. B **15** 2493 (1977)

[18] S. W. Lim, D. K. Hwang and J. M. Myoung, Solid. State Commun., **125** 231 (2003)

[19] Y Yoshino, K. Inoue, M. Takeuchi and K. Ohwada, Vacuum, **51** 601 (1998)

[20] A. P. Roth, J. B. Webb and D. F. Williams, Phys. Rev. B **25** 7836 (1982)

[21] A. F. Kohan, G. Ceder, D. Morgan and C. G. Van de Walle, Phys. Rev. B **61** 15019 (2000)

[22] J. A. Wilson, Adv. Phys., **21** 143 (1972)

[23] R. Monnier and B. Delley, Phys. Rev. Lett., **87** 15, 157204 (2001)

[24] I. S. Elfimov, S. Yunoki and G. A. Sawatzky, Phys. Rev. Lett. **89** 216403 (2002)

Chapter 5

HfO_2

5.1 Introduction

HfO_2 is a wide band gap (5.7 eV) insulating oxide. It exists in three structural polymorphs - the room temperature monoclinic phase in figure 5.1 transforms to a tetragonal phase at $\sim$ 2000 K and to a cubic phase at $\sim$ 2870 K. The monoclinic phase has a, b and c lattice parameters of 5.29, 5.18 and 5.12 Å respectively, and the space group $P2_1/c$. HfO_2 is isostructural with ZrO_2 and has a melting point of $\sim$ 3070 K and a boiling point of 5670 K, a molecular weight of 210.49 and a density of 9.68 gcm^{-3}. The radius of a Hf^{4+} ion is 84 pm and that of O^{2-} is 135 pm. HfO_2 has a high static dielectric constant of 25. The powder is white and thin films, which have been grown by PLD, chemical vapour deposition, atomic layer deposition and chemical solution deposition, are transparent.

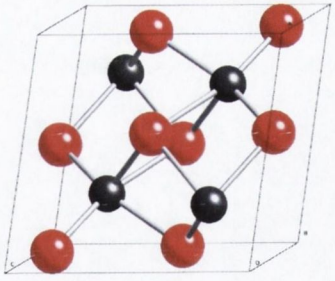


Figure 5.1 The monoclinic HfO_2 structure, with the Hf atoms in black and the oxygen atoms in red

Recent interest in HfO_2 has stemmed from the suggestion that it could replace SiO_2 as the gate dielectric in complementary metal-oxide semiconductor (CMOS) devices [1]. The SiO_2/Si interface provides the best oxide/Si interface quality, which is one of the reasons SiO_2 has proven so popular as a gate dielectric. Improvement in the performance of these

devices has been achieved through miniaturisation, but a fundamental limit has now been reached. When the SiO_2 layer is very thin ($\sim$ 1 nm) the leakage current between the gate and the substrate is unacceptably high. Thin HfO_2 films of the same thickness grown on Si demonstrate much lower leakage currents and its high thermal stability make it ideal given the post-deposition annealing which is inevitable in current CMOS fabrication processes [2][3][4].

According to an unpublished report by Rao et al [5] HfO_2 may be a promising material for spin electronic and magneto-optic applications. They found that monoclinic Co-doped HfO_2 thin films have a giant magnetic moment of 6.8 μ_B/Co with a Curie temperature of $\sim$ 880 K. Their films were deposited by PLD on lattice-matched yttria-stabilised zirconia (YSZ) substrates in an oxygen background. The optimum oxygen partial pressure was found to be 1 x 10^{-4} Torr, with reduced moments found in films made at higher or lower pressures. The films were transparent in the ultra violet/visible range of wavelengths (T $\sim$ 65 %), and cobalt-doped samples had a dielectric constant of 18. Coercivity of 5.2 mT was found at room temperature, and cobalt was found to be in the Co^{2+} valence state from electron energy loss spectroscopy (EELS). The films have c-axis orientation and are tilted by about $\sim$ 9.1° with respect to the (001) axis of the substrate. A bulk sample had a small moment of 0.055 μ_B/Co.

It has been suggested that the spin-filter effect from an insulating ferromagnetic tunnel barrier may be exploited for quantum computation in solid state devices [6]. EuO and EuS are ferromagnetic insulators with Curie temperatures of 69 K and 16 K respectively, and the spin-filter effect has been demonstrated in EuS layers by Esaki et al [7] in 1967. However, spin electronic devices will need to operate at room temperature and above, and so Co-doped

HfO_2 with a Curie temperature which is greater than 800 K has excellent prospects.

In this chapter we study pure and doped HfO_2, with emphasis on the undoped material, which very surprisingly turns out to be ferromagnetic at room temperature.

5.2 Undoped HfO_2

5.2.1 Bulk material

Two different hafnium dioxide powders were used to produce targets - both from Sigma-Aldrich - one of which was nominally 98 % pure and the second nominally 99.95 % pure. The powders were pressed into pellets and sintered at 1200 °C in air for 24 hours. XRD shows that the powder is in the monoclinic phase, as expected, in 5.2a. HfO_2 powder is diamagnetic, as seen in the magnetisation curve of figure 5.2b. The diamagnetic susceptibility of HfO_2 was measured on an 80 mg sintered pellet made from the higher purity powder. The room-temperature value is - 1.6 10^{-9} m^3kg^{-1}.

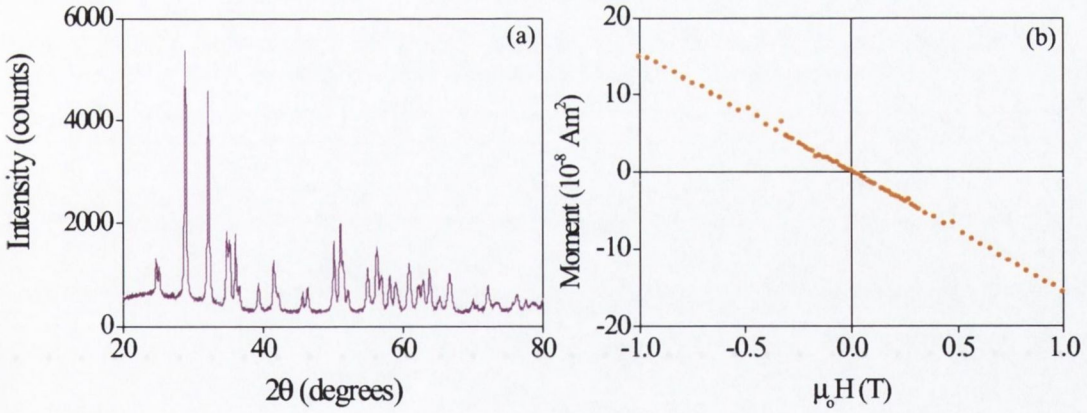


Figure 5.2 (a) The XRD pattern of pure HfO_2 crystallised in the monoclinic structure and (b) the room temperature magnetisation curve of undoped HfO_2 powder

Zirconium was the major metallic impurity identified by the manufacturers. However, SEM/EDAX analysis of the powder shows that indium is the main impurity in the 98 %

pure powder (0.2 at. %), with zirconium levels in both powders < 0.1 at. %. The second powder was supposed to be 99.9999 % pure excluding zirconium. In both cases the Fe, Co and Ni were found to be below the detection limit of EDAX (0.1 wt.%).

5.2.2 Films

Thin HfO_2 films were deposited by PLD onto R-cut and C-cut sapphire and Si substrates at 750 °C in 1.10^{-4} mbar of oxygen with deposition times ranging from 2.5 to 22.5 minutes. One film was also grown on R-cut sapphire in 1 mbar of oxygen. Silicon substrates were treated in HF to remove the oxide layer before deposition. The films are insulating and transparent.

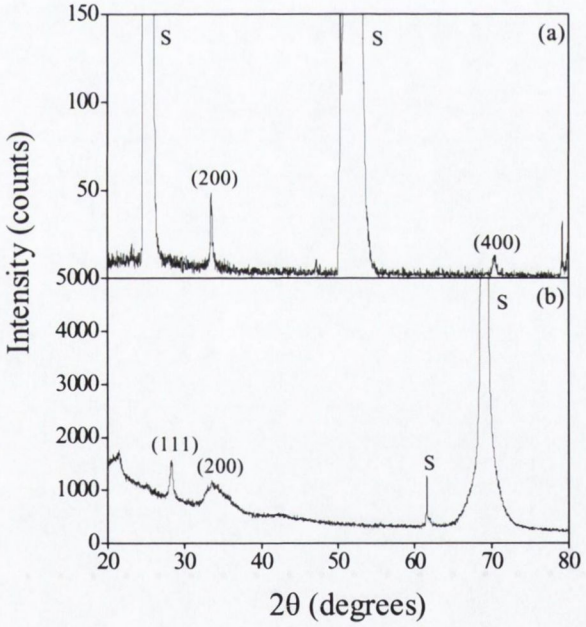


Figure 5.3 The XRD patterns of HfO_2 films on (a) R-cut sapphire and (b) (100) silicon

Films grown on R-cut sapphire have a (200) texture in the monoclinic structure as shown in figure 5.3a. On silicon the orientation is less clear, with the (111) monoclinic reflection indexed, and a broad bump around the (200) position.

SEM images show that the films grown on R-cut sapphire in 1.10^{-4} mbar of oxygen have a rougher, more dimpled surface (figure 5.4a) than the sample grown in 1 mbar of oxygen (figure 5.4b).

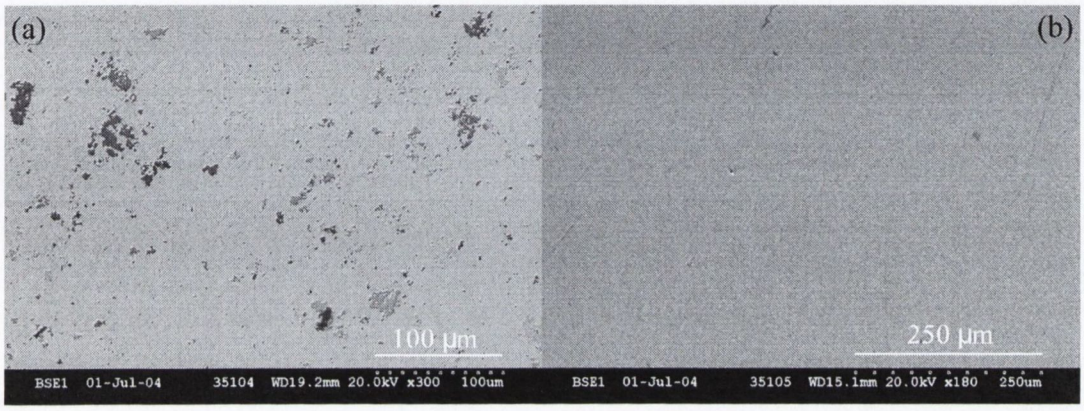


Figure 5.4 SEM images of HfO_2 films grown on R-cut sapphire in (a) 1.10^{-4} mbar of oxygen and (b) 1 mbar of oxygen

EDAX analysis indicates that up to 2 at. % Fe is found in films made from the 98 % pure powder, while in films made from the 99.95 % pure powder the Fe content lies below the detection limit.

Film thicknesses lie between 13 and 400 nm, as determined by reflectivity, small angle x-ray reflectivity and SEM imaging of the thick films, as shown in figure 5.5 a, b and c respectively. The film in 5.5a was grown on C-cut sapphire and is $\sim$ 370 nm thick, the film in 5.5b was grown on R-cut sapphire and is $\sim$ 80 nm, while the image in 5.5c is of a film on R-cut sapphire which is approximately 240 nm thick. Roughness was generally less than 0.2 nm.

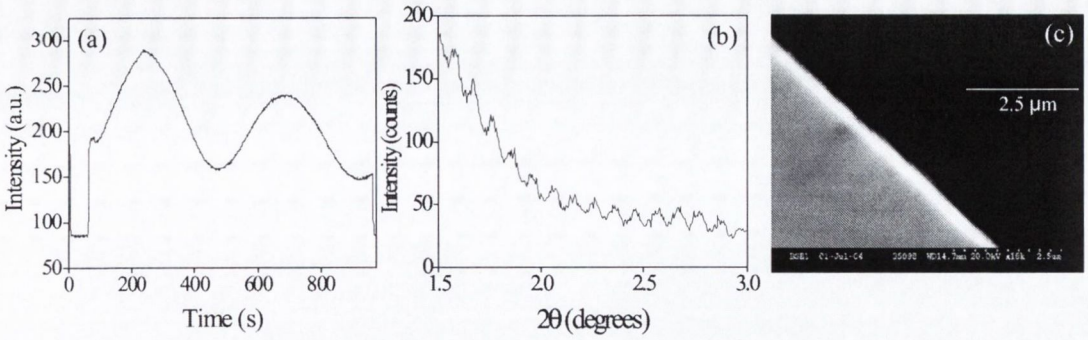


Figure 5.5 Thickness of HfO_2 thin films as determined by (a) in-situ reflectivity, (b) small angle x-ray reflectivity and (c) SEM imaging

Nanoscale analysis of the films in STEM showed that no iron was present at the detection limit (0.1 wt. %). In figure 5.6 images of a HfO_2 film on C-cut sapphire can be seen at different magnifications. The film is about 22 nm thick (figure 5.6a). A defect layer < 1 nm thick can be seen at the film/substrate interface in 5.6b, while structures of order 13 nm can be identified in the bulk of the film.

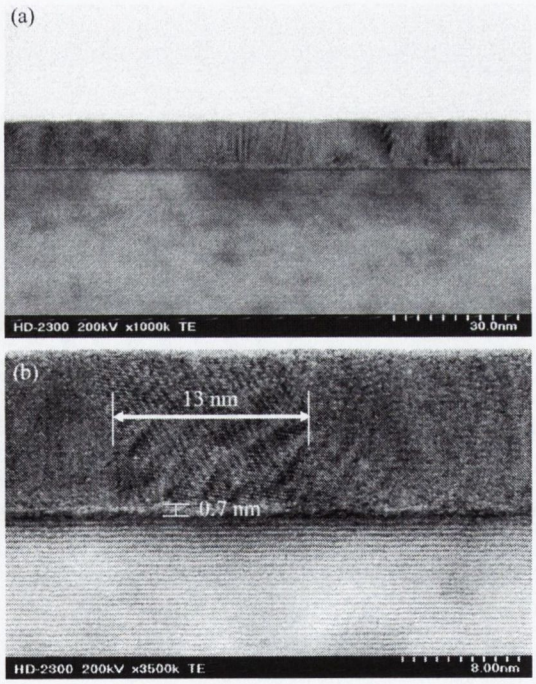


Figure 5.6 STEM images of a HfO_2 film on C-cut sapphire at different magnifications

Optical transmission spectra were recorded for films grown on double-side polished R-

cut sapphire with a 15 minute deposition time in 1.10^{-4} and 1 mbar of oxygen as shown in figure 5.7. The band edge appears at $\sim$ 5.7 eV for films grown at low pressures, while the edge shifts to higher energies in the film grown at a higher pressure. Transmission is high ($\sim$ 80 %) in all cases.

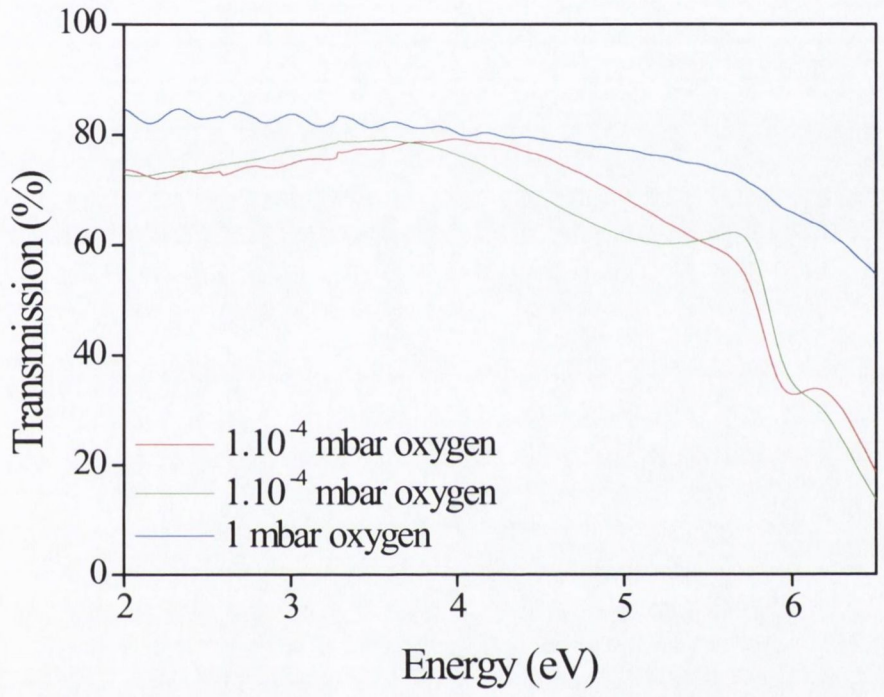


Figure 5.7 Optical transmission spectra of two HfO_2 films grown in 1.10^{-4} mbar (red and green) of oxygen and another grown in 1 mbar of oxygen (blue). All films are on R-cut sapphire.

Unexpectedly, the HfO_2 films are ferromagnetic and show coercivity of 2 - 5 mT at room temperature. The first curve in figure 5.8 shows the diamagnetism of a blank R-cut sapphire substrate subjected to the same thermal cycle in the deposition chamber as one with a thin film deposited on it. The susceptibility - 4.8 10^{-9} m^3kg^{-1} agrees with the accepted value for sapphire, - 4.6 10^{-9} m^3kg^{-1}. The second curve in figure 5.8 shows data for a HfO_2 film on R-cut sapphire. The ferromagnetic signal remaining after subtraction of the linear

diamagnetic background is shown in the third curve. The background slope is defined by data in the range 3 - 5 T. Because of their relative masses, the diamagnetic signal from the substrate is three orders of magnitude greater than the diamagnetic signal of the thin film deposited on it. Hence the diamagnetism of the HfO_2 films is not measurable, nor is any high field slope above 3 T.

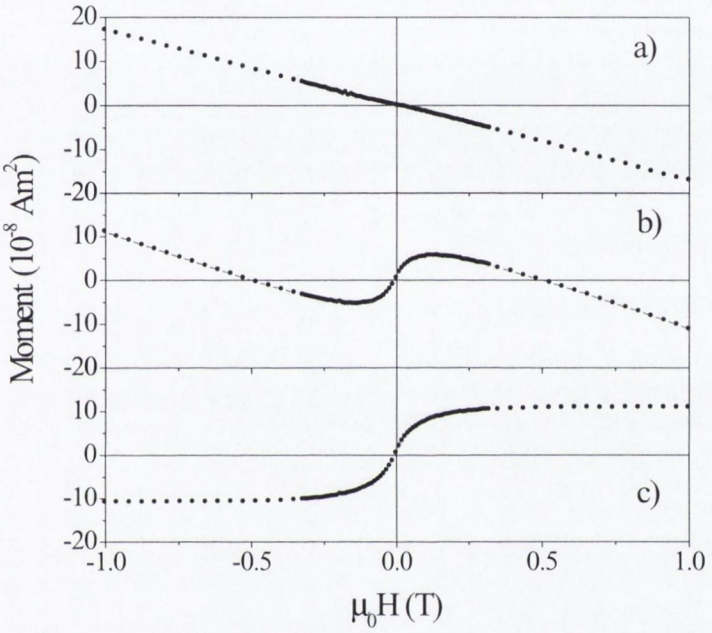


Figure 5.8 Magnetization curves of a) a blank R-cut sapphire substrate, b) the substrate with an 82 nm film of HfO_2 and c) data for HfO_2 after subtracting the background diamagnetism of the substrate

Figure 5.9 shows the room temperature magnetisation curves for films grown on R-cut and C-cut sapphire and Si (100) substrates. The moment is greatest in the film on C-cut sapphire, and corresponds to $\sim 0.15\ \mu_B$ per HfO_2 formula unit. Pronounced anisotropy in the magnetisation is observed, with a larger moment measured in the perpendicular direction for films on R- or C- cut sapphire and greatest in the parallel direction for films grown on Si (100).

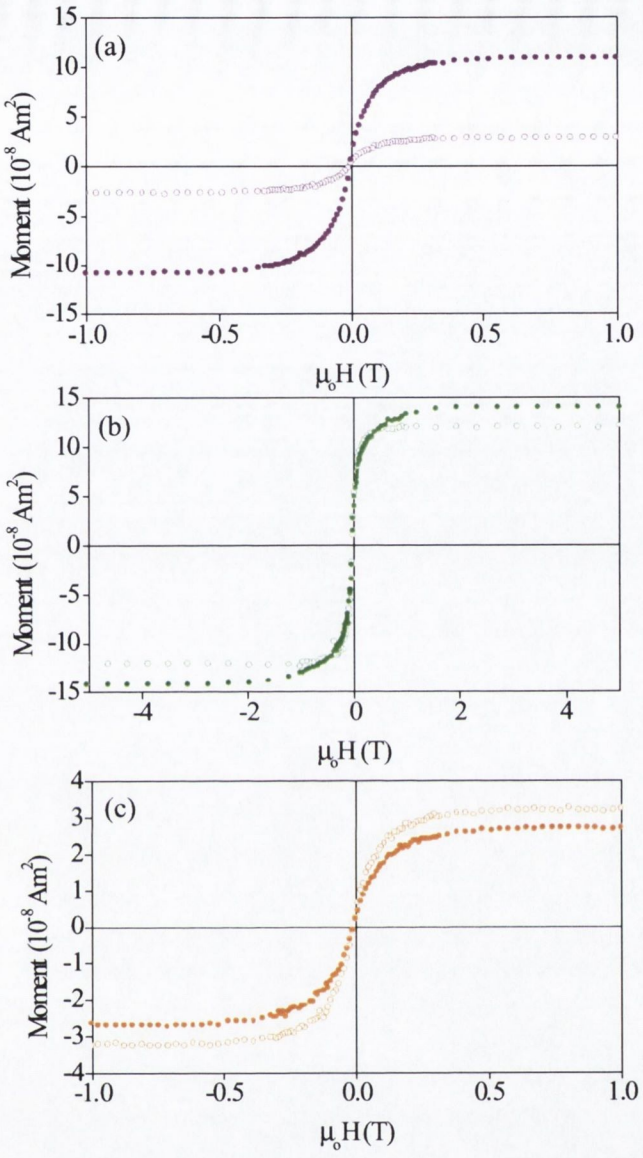


Figure 5.9 Magnetisation curves for HfO_2 films on (a) an R-cut sapphire substrate, (b) on C-cut sapphire and (c) a Si (100) substrate. Open circles indicate measurements made in the parallel direction and closed, the perpendicular direction

In figure 5.10 the moment is plotted per unit substrate area versus film thickness for all three substrates. The moments vary from 50 - 315 $\mu_B \text{nm}^{-2}$ and the film deposited in 1 mbar of oxygen falls in the middle of this range with a moment of 250 $\mu_B \text{nm}^{-2}$.

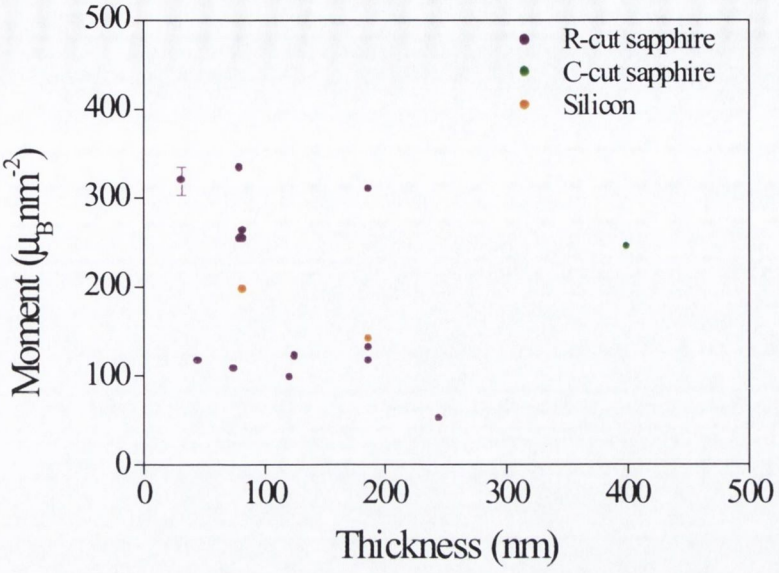


Figure 5.10 The moment per unit area plotted for all films on R-cut and C-cut sapphire and Si (100)

Table 1 summarizes typical data obtained for HfO_2 films deposited from different targets in different circumstances.

No	Composition	Substrate	Thickness (nm)	σ_{perp} (10^{-9} Am^2)	σ_{par} (10^{-9} Am^2)	σ_{av} (10^{-9} Am^2)
1	HfO_2	R-Al_2O_3	80	108	27	81
2	HfO_2	R-Al_2O_3	82	90	36	72
3	HfO_2	R-Al_2O_3	31	73	65	70
4	HfO_2	Si	187	27	32	29
5	HfO_2	C-Al_2O_3	13	345	292	327
6	HfO_2	C -Al_2O_3	13	83	70	78
7	HfO_2	C-Al_2O_3	51	140	120	133
8	$Hf_{0.94}Sc_{0.06}O_2$	R-Al_2O_3	~ 90	11	-	11
9	$Hf_{0.97}Ti_{0.03}O_2$	R-Al_2O_3	~ 90	12	-	12
10	$Hf_{0.80}Ta_{0.20}O_2$	R-Al_2O_3	~ 90	10	-	10
11	$Hf_{0.98}Co_{0.02}O_2$	R-Al_2O_3	~ 80	30	-	30

Table 1 - Magnetic properties of HfO_2 films deposited in different conditions, with measurements taken in the perpendicular and parallel directions

In light of the unexpected results from HfO_2 films, the powder was re-examined. Figure

5.11a shows the magnetisation curve of the as-received sample (as in figure 5.2b), which is diamagnetic. This powder was then heated in vacuum at 750 °C for two hours and re-measured. A small moment develops after the heat treatment in vacuum corresponding to a moment $\sigma = 1.9\ 10^{-3}$ Am^2kg^{-1} or 7.10^{-5} μ_B per formula unit (figure 5.11b), which can be eliminated by reheating the powder at 750 °C for 30 minutes in air (5.11c). The main defects introduced by heating hafnia in vacuum are like to be oxygen vacancies [8].

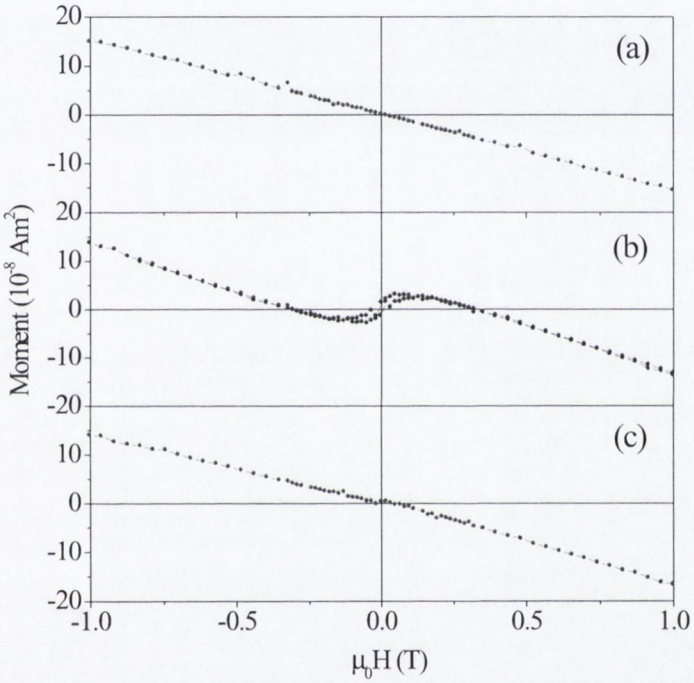


Figure 5.11 Magnetization curves of HfO_2 powder measured a) as received, b) after heating at 750 °C in vacuum and c) after reheating the same sample at 750 °C in air.

5.3 Doped HfO_2 thin films

Targets were also prepared with 5 at. % Sc, Ti and Ta and 0.5 - 5 at. % Co, and thin films prepared on R-cut sapphire as for the undoped sample. In figure 5.12 the transition metal concentration in films made from $Hf_{0.95}M_{0.05}O_2$ targets is plotted, with $x \sim 20$ % in

the Ta-doped film.

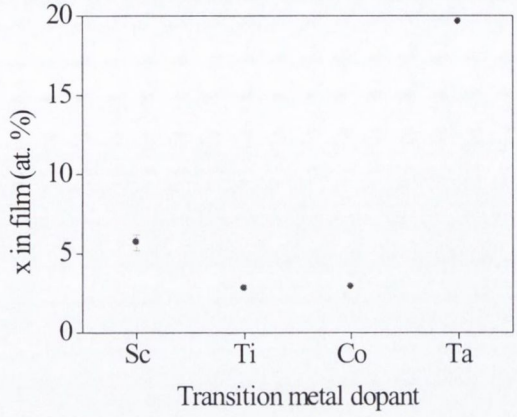


Figure 5.12 Transition metal concentration in films made from $Hf_{0.95}M_{0.05}O_2$ targets

Doped films are also ferromagnetic, with coercivities of up to 23 mT found in a $Hf_{0.96}Co_{0.04}O_2$ film. The moment per unit substrate area is plotted in figure 5.13a for films made from $Hf_{0.95}M_{0.05}O_2$ (M = Sc, Ti, Co and Ta) targets and in figure 5.13b the moment is plotted for the $Hf_{1-x}Co_xO_2$ series. It can be seen that the moment does not scale with Co content in figure 5.13b, on the contrary, it seems to fall with cobalt doping.

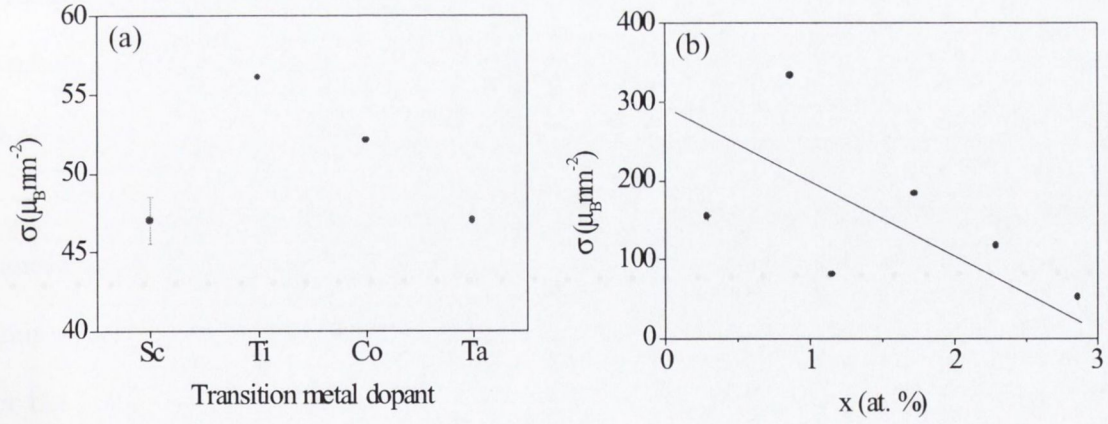


Figure 5.13 The moment per unit substrate area (a) for films made from $Hf_{0.95}M_{0.05}O_2$ (M = Sc, Ti, Co, Ta) targets and (b) for the $Hf_{1-x}Co_xO_2$ series

5.4 Discussion

Rao et al [5] found a moment of up to 6.8 μ_B/Co in $Hf_{0.95}Co_{0.05}O_2$. We have chosen to plot our data as moment per unit substrate area, but when converted, a moment of 13.4 μ_B/Co is found in the $Hf_{0.99}Co_{0.01}O_2$ film. So we too find a 'giant moment' per cobalt atom.

However, we find that undoped HfO_2 is ferromagnetic at room temperature. The ions are Hf^{4+} [Xe] $4f^{14}$ and O^{2-} [Ne] and have closed shell configurations with no unpaired electrons - a similar case to Sc-doped ZnO (Sc^{3+} [Ar], Zn^{2+} [Ar] $3d^{10}$) where we found a moment of 0.3 μ_B/Sc. It is generally accepted that magnetic order in insulators requires cations with partially-filled shells of d or f electrons - so how could HfO_2 possibly be ferromagnetic?

As in all of the systems studied so far the magnetisation is very anisotropic, with $m_\perp \sim 0.8$ - 2.5 $m_{\parallel}$, the Curie temperature exceeds 500 K, with the moment changing little from 5 K to 400 K and the moment varies little with film thickness. However, undoped SnO_2 and ZnO are not ferromagnetic. The fact that undoped HfO_2 powder develops a moment when heated in vacuum and loses it when heated in air suggests that oxygen vacancies play a role in the ferromagnetism in bulk samples. However, the moment of the film deposited in 1 mbar of oxygen (250 $\mu_B nm^{-2}$) is not any smaller than those deposited in 1.10^{-4} mbar of oxygen.

The magnetisation of the films cannot be explained by magnetic impurities. The nanoscale analysis of the films in the STEM showed that no iron was present at the detection limit (0.1 wt. %). Approximately 100 times more iron than this would be needed to account for the magnetisation of some of the films.

Again, as in the SnO_2 and ZnO systems, the moment per unit substrate areas is $\sim$ 200 $\mu_B nm^{-2}$ on average. This supports the theory that the ferromagnetism is related to lattice

defects, but while doping is needed to "switch them on" in SnO_2 and ZnO, it is not necessary in HfO_2.

References

[1] A. I. Kingon, J. P. Maria and S. K. Streiffer, Nature **406** 1032 (2000)

[2] G. D. Wilk, R. M. Wallace and J. M. Anthony, Appl. Phys. Lett., **74** 2854 (1999)

[3] G. D. Wilk, R. M. Wallace and J. M. Anthony, J. Appl. Phys., **87** 484 (2000)

[4] B. H. Lee, L. Kang, R. Nieh, W. J. Qi and J. C. Lee, Appl. Phys. Lett., **76** 1926 (2000)

[5] M. S. Ramachandra Rao, S. Dhar, S. J. Welz, S. B. Ogale, D. C. Kundaliya, S. R. Shinde, S. E. Lofland, C. J. Metting, R. Erni, N. D. Browning and T. Venkatesan, cond-mat/0405378

[6] D. P. DiVincenzo, J. Appl. Phys., **85** 4785 (1999)

[7] L. Esaki et al, Phys. Rev. Lett., **19** 852 (1967)

[8] A. S. Foster, F. Lopez-Gejo, A. L. Shluger and R. M. Nieminen, Phys. Rev. B 65 174117 (2002)

Chapter 6

Discussion - dilute magnetic oxides

6.1 Introduction

Room temperature ferromagnetism in an oxide semiconductor was first reported in 2001 for cobalt doped TiO_2 by Matsumoto et al [1]. High temperature ferromagnetism is not expected in these materials because the magnetic doping level is far below the cation percolation threshold x_p needed for long-range order based on superexchange or double exchange interactions. However, for the last three years there have been recurrent reports of high-temperature ferromagnetism in dilute magnetic oxides. A compendium of results on the concentration dependence of the ferromagnetic moments in the most extensively studied systems - $3d$ transition metal doped TiO_2 (a) and ZnO (b) - is shown in figure 6.1. This literature review reveals no discernible trends, with properties varying greatly for samples of the same nominal composition prepared by different methods or by different groups.

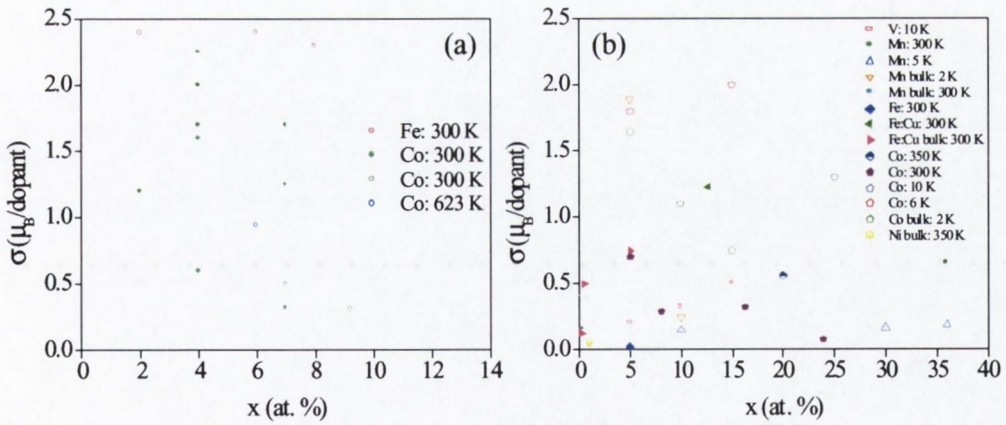


Figure 6.1 Magnetic moment per transition metal cation in (a) TiO_2 doped with Fe or Co (rutile - open circles; anatase - closed circles) and (b) ZnO doped with V, Mn, Fe, Co or Ni

These reports were greeted with scepticism, and the belief that the data somehow

reflected the presence of secondary ferromagnetic phases rather than intrinsic long range ferromagnetism in these oxides. Careful examination of samples of anatase $Ti_{1-x}Co_xO_2$ films ($0.04 \leq x \leq 0.10$) has revealed the presence of clusters of metallic cobalt [2] which are at least partially-responsible for the observed ferromagnetism. Whether ferromagnetism in transition metal doped TiO_2 is carrier mediated or extrinsic still remains questionable.

Ueda et al [3] first reported ferromagnetic behaviour in Co-doped ZnO with T_c between 280 and 300 K. The reproducibility, however, was less than 10 %. Hence the realisation of ferromagnetic long range order in Co-doped ZnO was at first controversial. However, there is spectroscopic evidence that divalent cobalt substitutes for zinc on the tetrahedral sites of the ZnO wurtzite structure [4]. In general the reported moments never exceeded 2.5 μ_B/dopant atom, until a giant moment of 7.5 μ_B/Co with a Curie temperature of 650 K was reported in cobalt doped SnO_2 thin films ($x = 0.05$) [5], and a moment of 6.8 μ_B/Co with a Curie temperature of 880 K was found in insulating cobalt doped HfO_2 films ($x = 0.05$) [6]. This was entirely unexpected as the moments exceed the spin-only moment of cobalt (3 μ_B for Co^{2+}:$3d^7$).

If these materials are truly intrinsically ferromagnetic they may revolutionise the field of spin electronics - but until a clear connection between their magnetic properties and electronic structure can be demonstrated, doubts will persist. To further our understanding of this phenomenon we decided to undertake a systematic study of three systems:

1. $Sn_{1-x}M_xO_2$, where M = Mn, Fe or Co, $0 \leq x \leq 0.3$

2. $Zn_{1-x}M_xO$ for M = Sc - Cu where $x = 0.05$ nominally, and $Zn_{1-x}Co_xO$ where $0 \leq x \leq 0.25$

3. $Hf_{1-x}Co_xO_2$ where $0 \leq x \leq 0.03$, and $Hf_{1-x}M_xO_2$ where M = Sc, Ti and Ta and x

= 0.05 nominally

6.2 Results

6.2.1 Giant moments

We find that dilute magnetic oxides are ferromagnetic, that giant moments per dopant atom are found in all three systems when x is small, and most surprisingly, that undoped HfO_2 is ferromagnetic. No magnetic moment is observed in undoped SnO_2 or ZnO films, although giant moments of up to 20 μ_B/Mn (x= 0.003), 3.5 μ_B/Fe (x = 0.043) and 4.1 μ_B/Co (x = 0.018) are found in $Sn_{1-x}M_xO_2$ (M = Mn, Fe or Co), which fall as the dopant concentration increases as seen in figure 6.2.

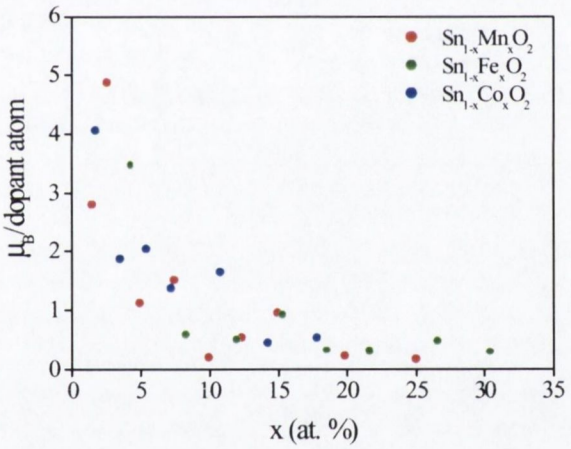


Figure 6.2 The moment per dopant atom in $Sn_{1-x}M_xO_2$ (M = Mn, Fe or Co) thin films

A similar trend is seen in $Zn_{1-x}Co_xO$ (figure 6.3a), with a giant magnetic moment of 5.9 μ_B for x = 0.022, while the variation of the magnetic moment across the transition-metal doped ZnO series (with moments measured with the field perpendicular (purple) or parallel (orange) to the plane of the film) is illustrated in figure 6.3b. There are maxima at the beginning of the 3*d* series at Ti and V, and towards the end of the series at Co. No moment

greater than the experimental uncertainty ($< 0.1\ \mu_B$) was observed for Cr, Mn and Cu.

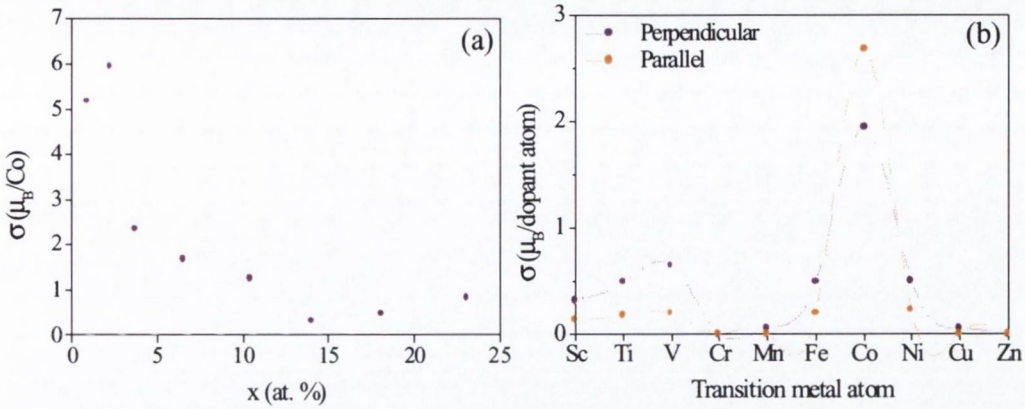


Figure 6.3 (a) The variation of the moment per cobalt atom with concentration in $Zn_{1-x}Co_xO$ and (b) the variation of the moment across transition metal doped ZnO when measured in the perpendicular (purple) or parallel (orange) directions

Undoped HfO_2 thin films deposited on various substrates (R-cut and C-cut sapphire, Si (100)) exhibit ferromagnetic behaviour at room temperature. The magnetic moment is of order 0.15 μ_B/formula unit as shown in figure 6.4. However, it is misleading to express the moment in this way, because it does not increase in proportion to the film thickness (figure 5.10).

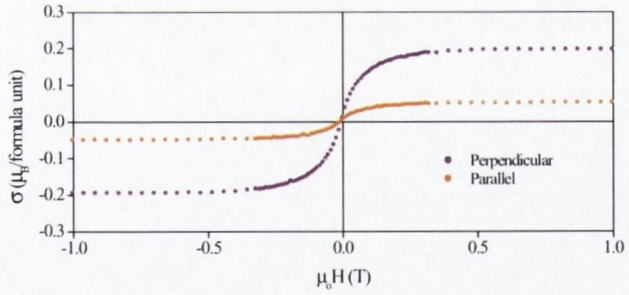


Figure 6.4 Magnetization curves for an HfO_2 film measured with the field perpendicular (purple) or parallel (orange) to the plane of the R-cut sapphire substrate

And finally, the moment per dopant atom falls with increasing x in $Hf_{1-x}M_xO_2$ thin films on R-cut sapphire where M = Sc, Ti, Co or Ta, as seen in figure 6.5. A moment greater than 20 μ_B/Co is found in the $Hf_{0.997}Co_{0.003}O_2$ film, where the significant magnetic contribution from undoped HfO_2 was not taken into account.

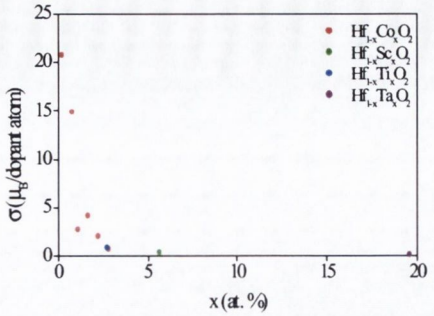


Figure 6.5 The moment per dopant atom as a function of x in $Hf_{1-x}M_xO_2$ thin films on R-cut sapphire where M = Sc, Ti, Co and Ta

In figure 6.6 our data is plotted as a moment per unit substrate area for (a) transition metal doped SnO_2, (b) ZnO, (c) undoped HfO_2 on different substrates and (d) doped HfO_2. *There is no systematic concentration or thickness dependence of the moment in any case, and in all cases the moment extrapolates to 150 - 200* $\mu_B nm^{-2}$ *at* $x = 0$. The lack of proportionality of magnetic moment and film thickness suggests an origin at the film surface or the interface with the substrate, rather than in the bulk.

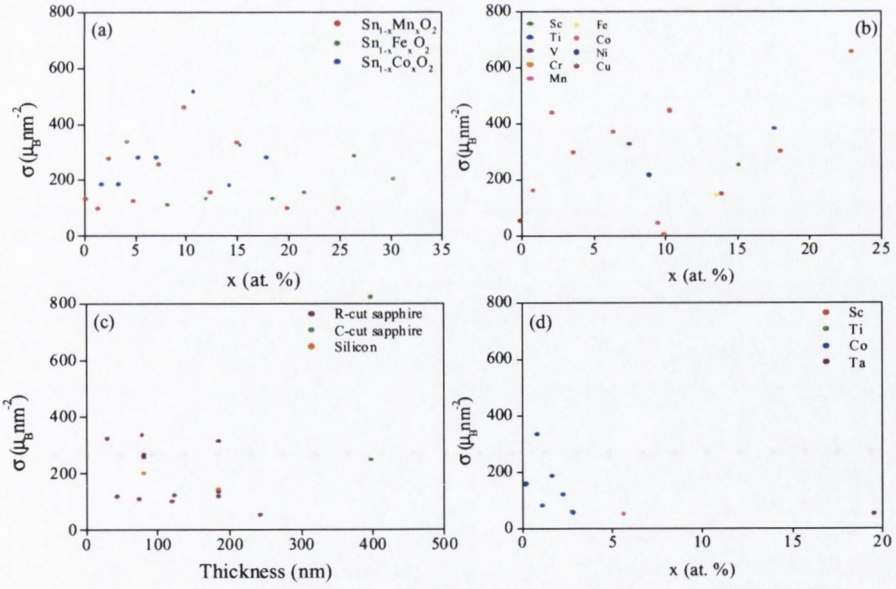


Figure 6.6 The moment per unit substrate area versus x in (a) Mn, Fe and Co doped SnO_2, (b) transition metal doped ZnO, (c) undoped HfO_2 on a variety of substrates as a function of thickness and (d) transition metal doped HfO_2 versus x

To summarise, the magnetisation in transition metal doped SnO_2, ZnO and HfO_2 thin

films consists of a component from the transition metal ion not expected to exceed its spin only value and a component like that in the undoped HfO_2 films which is though to arise from lattice defects.

In all three cases the average moment expressed per transition metal cation for films of a given thickness falls progressively with increasing x. The fall-off in moment with increasing x can successfuly be rationalised, for example in cobalt doped SnO_2 and ZnO, in terms of a random distribution of cobalt ions over the cation sites in the lattice. Isolated ions contribute the full moment m, pairs and most groups of four are antiferromagnetically coupled and make no net contribution, triplets contribute m/3. Large antiferromagnetically-coupled clusters of N atoms will make a contribution $m/\sqrt{N}$. The model reproduces the trend in figures 6.2 and 6.3a, provided the distribution is weighted in favour of cobalt nearest-neighbour pairs - as seen in figure 6.7 a and b. But clearly it is limited by the spin-only value of Co^{2+} of 3 μ_B and cannot account for the very lage moments found at small x.

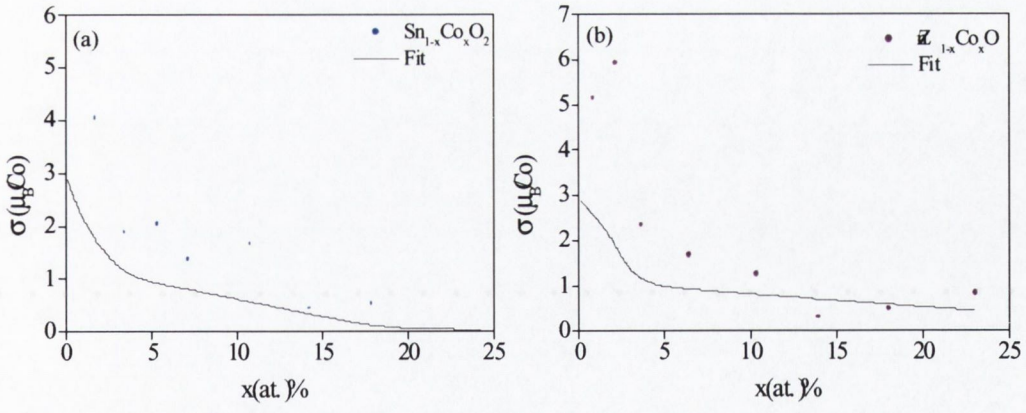


Figure 6.7 The moment per dopant atom as a function of x in (a) $Sn_{1-x}Co_xO_2$ thin films with the fit shown as a black line and (b) $Zn_{1-x}Co_xO$ thin films, with the fit to the data using a spin-only moment of 3 μ_B for Co^{2+} shown as a solid line

6.2.2 Anisotropic saturation magnetisation

Figure 6.8 shows the anisotropy of the magnetization measured on thin films of undoped HfO_2 and transition metal (Mn, Fe, Co) doped SnO_2 films.

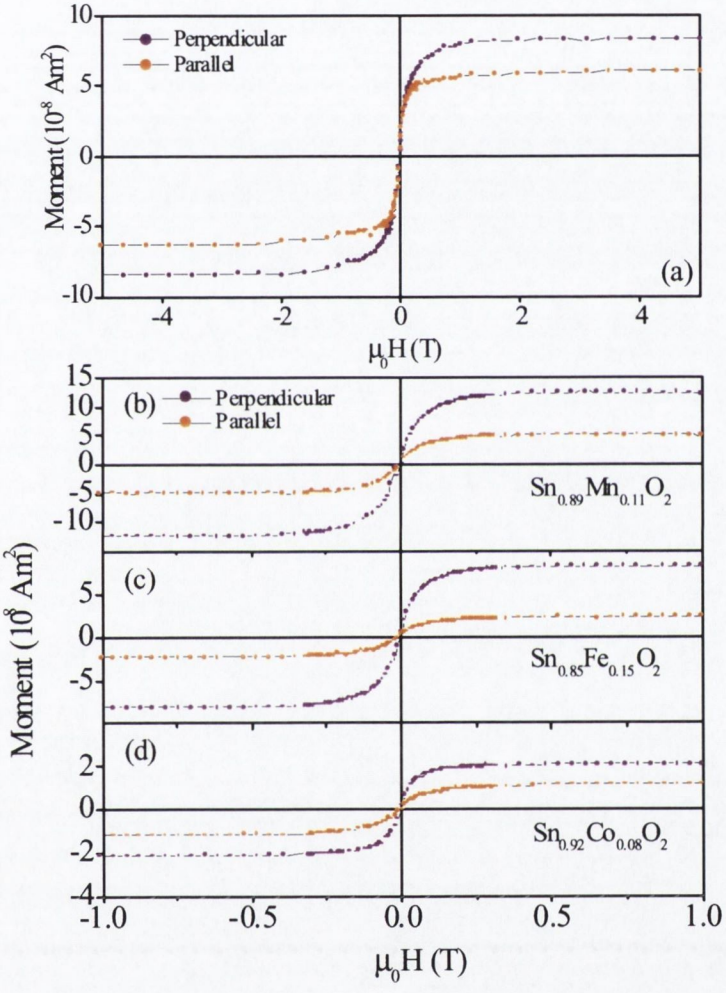


Figure 6.8 (a) Anisotropy of magnetisation in a HfO_2 film and (b), (c) and (d) anisotropy of magnetisation in transition metal doped SnO_2 films

The moment can be as much as three times as great when the field is applied perpendicular to the film as it is when the field is in-plane. The sign of the anisotropy depends on

the substrate. Huge anisotropy is also observed in Co-doped and V-doped ZnO films where significant variations in anisotropy are found within the plane of the substrate [7] due to a preferred in-plane orientation of the film on R-cut sapphire. No such in-plane anisotropy was observed in HfO_2 or transition-metal-doped SnO_2 films.

6.2.3 Hysteresis

The magnetization curves of these oxide films usually show little hysteresis. It is only at doping levels approaching the percolation limit that significant hysteresis appears. Figure 6.9 shows the magnetization at 300 K and 5 K of Fe-doped SnO_2 films grown using the target of 5 at. % Fe content. The films are ferromagnetic at room temperature with evident hysteresis. Coercivity increases from 56 mT at 300 K to 150 mT at 5 K. Hysteresis is also present in the Co-doped HfO_2 films, where the coercivity increase with cobalt content reaching 23 mT at $x = 0.04$.

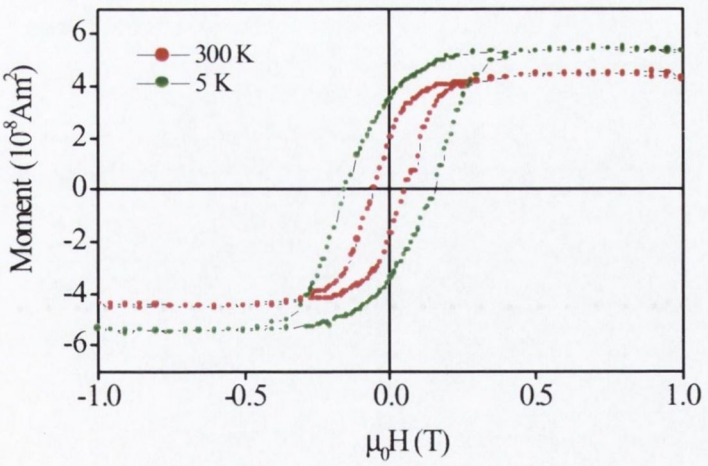


Figure 6.9 Magnetisation loops of a $Sn_{0.75}Fe_{0.25}O_2$ film at 300 K and 5 K

6.3 Impurities and secondary phases

Many still believe that dilute magnetic oxides are not intrinsically ferromagnetic. The results were so unexpected that explanations were initially sought in terms of phase segregation, particularly in transition metal doped TiO_2, where an intrinsic origin of the ferromagnetism has been called into question by the detection of a secondary magnetic phase composed of cobalt nanoclusters [2]. We have taken precautions at every stage of the production process to ensure that our films are single phase.

We use high quality oxide powders (at least 99.99 % pure) which we analyse by XRD, EDAX and SQUID measurements. The targets are made and sintered in clean environments. Typically only one film is grown from each target, almost immediately after it has been sintered, reducing the risk of subsequent contamination or target degradation.

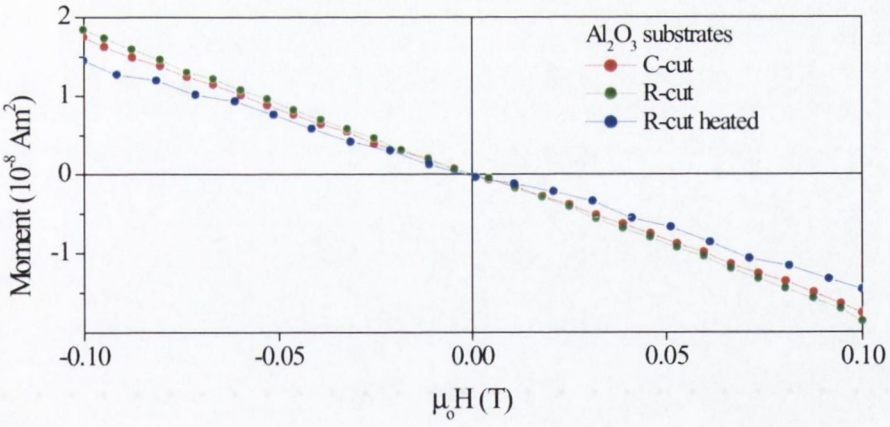


Figure 6.10 Typical magnetisation curves of C-cut and R-cut sapphire, and a heat-treated R-cut sapphire substrate

We use high quality single crystalline substrates, several of which are measured in the SQUID to ensure they contain no ferromagnetic impurities. The magnetisation curves for

a typical R-cut and C-cut sapphire substrate are shown in figure 6.10. We also reproduce the deposition environment for blank substrates and re-measure them in the SQUID. They are attached to the PLD heater with silver paint, the chamber is pumped down and the substrate heated to a typical deposition temperature (700 °C) for the length of a typical deposition (10 - 15 minutes). The substrate is then allowed to cool in vacuum, removed, cleaned and prepared for the SQUID in the way any film is and re-measured (figure 6.10). We have never found a ferromagnetic signal in any substrate. Two R-cut sapphire substrates were also analysed by Activation Laboratories in Canada, and they found no Fe or Ni at the ppm level, Co $<$ 5 ppm and Mn $\leq$ 3 ppm.

We perform detailed XRD, SEM (and in some cases TEM) and EDAX analysis on the films, and in all cases they appear to be uniform, homogeneous and single-phase. We always make several undoped films for comparison and in the case of SnO_2 and ZnO these films are never ferromagnetic - indicating that our powders, substrates and films are free of contamination. Although we unexpectedly find that undoped HfO_2 films are ferromagnetic, we believe this to be an intrinsic effect. Following a report by Kennedy et al [8] that resistivity follows a $\log \rho \sim T^{-\frac{1}{2}}$ dependence, characteristic of hopping transport in multiphase systems, over a wide temperature range in cobalt doped TiO_2 films as a result of cobalt clusters we plotted all of our SnO_2 and ZnO data in this way (HfO_2 is insulating), but found no such resistivity dependence (or to $T^{-\frac{1}{4}}$ (variable range hopping) or T^{-1} (Arrhenius)).

These tests simply demonstrate the absence of impurity phases, but we can also show that in the case of cobalt doped ZnO, Co^{2+} does substitute for zinc on the tetrahedral sites of the ZnO wurtzite structure from optical spectra. Perhaps the strongest evidence that ferromagnetism in dilute magnetic oxides is not due to secondary phases is that the

behaviour of these films clearly differ from those of any conventional ferromagnetic material - in this case the moment per 3d cation which exceeds the spin only value, and the anisotropy of the magnetisation. No known room temperature ferromagnets approach this level of anisotropy at room temperature.

In addition, Sc-doped ZnO does show strong anisotropic ferromagnetism at room temperature. This observation rules out the possibility of secondary ferromagnetic phases since neither Zn^{2+} ($3d^{10}$) or Sc^{3+} ($3d^{0}$) are magnetic ions.

6.4 The syndrome

Secondary phases cannot account for the observed magnetisation. A syndrome, or set of symptoms is associated with the high-temperature ferromagnetism in dilute magnetic oxide thin films:

1. The oxides are generally n-type, but they may be partially compensated

2. All have high static dielectric constants ($\varepsilon = 3.9$, 4.0 and 25 in SnO_2, ZnO and HfO_2 respectively)

3. The ferromagnets may be degenerate or non-degenerate semiconductors, or they may be insulators

4. The ferromagnetism is present at concentrations that lie far below the percolation threshold x_p associated with nearest-neighbour cation coupling ($x_p = 0.25$ in the rutile SnO_2 structure and 0.18 in wurtzite ZnO)

5. The average moment per transition-metal cation m_c approaches (or even exceeds) the spin-only moment at low concentrations x of magnetic cations. It falls progressively as x increases towards x_p.

6. Properties vary greatly for samples of the same nominal composition prepared by

different methods, or by different groups

These results challenge our understanding of magnetism in oxides. Superexchange, which is predominantly antiferromagnetic and short-ranged [9], cannot be invoked because the magnetic order appears where $x < x_p$. Regardless, the average net moment per magnetic cation in ferrimagnetically-ordered superexchange systems is rarely much greater than 1 μ_B. The ferromagnetic double-exchange mechanism (Zener double exchange in mixed valence manganites) can produce large moments but is also a nearest-neighbour interaction that requires mixed cation valence so that $3d^n \longleftrightarrow 3d^{n+1}$ configuration fluctuations can occur. There is also no evidence that mixed-valency is a common feature of these dilute oxides.

Point 4 in our syndrome states that ferromagnetism is present at concentrations that lie far below the percolation threshold x_p associated with nearest-neighbour cation coupling - so how then does the ferromagnetic interaction arise? We believe it is through the formation of magnetic polarons by donor defects resulting in an 'impurity' band. Over a sphere of radius R around the defect, it can orient the moments of the dopant ions parallel to its own. The radius of the electron orbital is of the order εa_o, where a_o is the Bohr radius and ε is the high-frequency dielectric constant of the oxide. This is illustrated in figure 6.11, where the donor defects are shown as yellow squares, the dopant ions are closed black circles and $x = 0.1$.

Ferromagnetism sets in when these magnetic polarons reach their percolation threshold. In materials with no d electrons such as Sc-doped ZnO or undoped HfO_2, it might be possible for the impurity band to overlap with an empty d band leading to some charge transfer, d population and consequent spin polarisation. The nature of the donor defects is unclear but they may be oxygen vacancies, which have been reported in SnO_2 [10] and ZnO [11] of

the order of a few percent. If the defects are oxygen vacancies, the vacancy with trapped electrons constitutes an F centre.

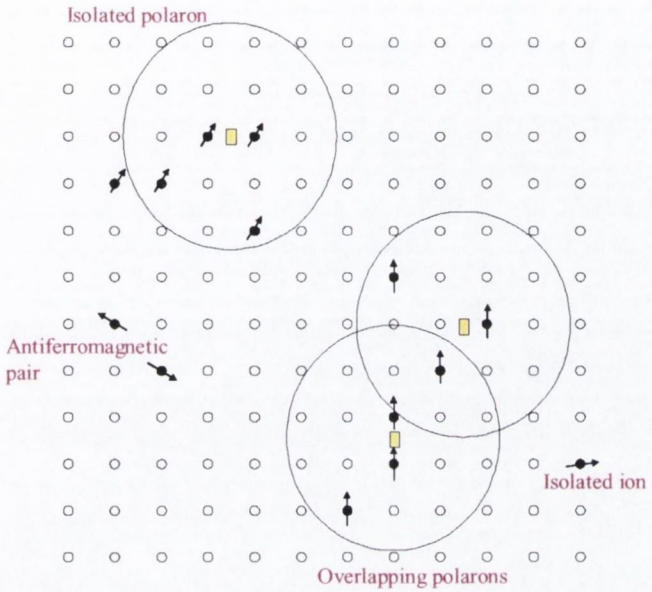


Figure 6.11 Schematic representation of a magnetic polaron, where $x = 0.1$ The donor defects are represented by yellow rectangles and the dopant ions as closed black circles

This model, based on donor electrons in a spin-split impurity band, for high-temperature ferromagnetism in dilute n-type magnetic semiconductors has been examined recently [12]. The model predicts ferromagnetism when the carrier concentration per cation δ exceeds $4.4/\gamma 3$, where $\gamma = km/m^*$; k is the high-frequency dielectric constant and m^* is the electron effective mass. To avoid antiferromagnetic coupling, the concentration of magnetic cations x must lie below the cation nearest-neighbour percolation threshold x_p. High Curie temperatures are expected when $3d$ states of the transition element hybridize with the spin-split impurity-band states at the Fermi level, providing charge transfer from the impurity band to the $3d$ ion of $0.01 - 0.02$ electrons per cation.

The variation of magnetic moment across the series shown in figure 6.3b is exactly as expected from this spin-split impurity band model. For the light $3d$ elements (e.g. Ti), the

$3d^{\uparrow}$ states lie high in the 2p(O) – 4s(Zn) gap, overlapping the spin-split donor impurity band. In the middle of the series (e.g. Mn), there is no overlap with the $3d$ levels and exchange is weak, but towards the end of the series (e.g. Co) the $3d^{\downarrow}$ states overlap the impurity band, which then has the opposite spin splitting for the same occupancy as seen in figure 6.12.

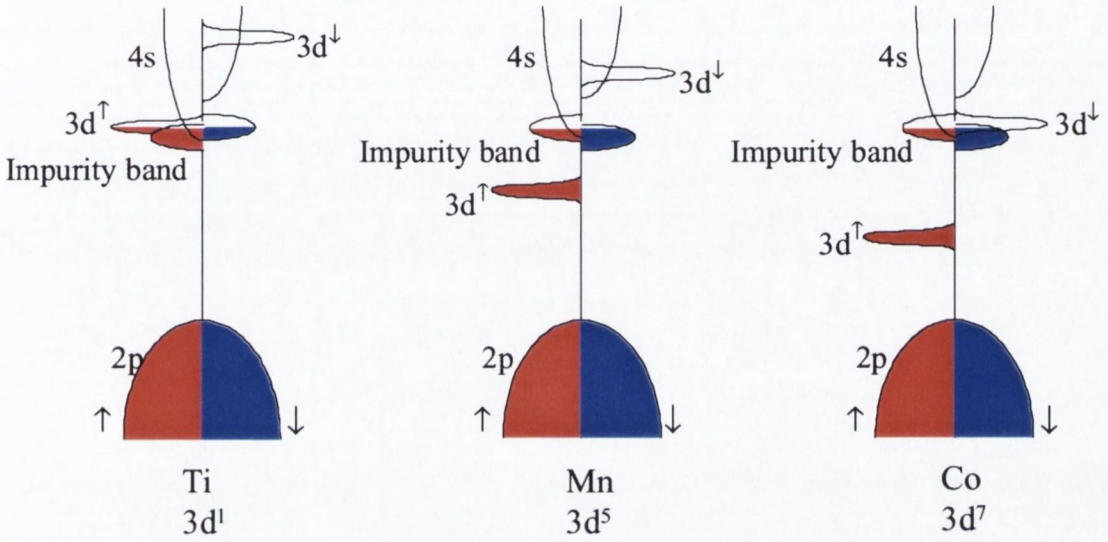


Figure 6.12 Schematic band structure of Ti, Mn, or Co doped ZnO

However, this model cannot explain moments in excess of the spin only moment of the dopant ions. We suspect that there is an additional contribution to the observed ferromagnetic signal from defects at the film/substrate interface. This argument is supported by the lack of proportionality of magnetic moment and x or film thickness. It has long been known that two-electron defect centres in oxides such as the F_t centre (adjacent F^+ centres) or two-hole centres such as a neutral cation vacancy (V^o centre) have a spin triplet ground state or low-lying triplet excited state [13] having an S = 1 magnetic moment associated with an orbitally-degenerate molecular orbital. These orbitals could then overlap to form a spin-split impurity band - the average triplet separation in a 10 nm film is about 0.5

nm. This band may split spontaneously (as in the case of undoped HfO_2) or be polarised by exchange with the $3d$ cation when present. The fact that we find no trace of magnetism in undoped ZnO or SnO_2 suggests that the defects are somehow 'switched on' by the dopants. This could arise is if the two-electron or two-hole defect centres have a singlet ground state, but a low-lying triplet excited state. Exchange coupling with the $3d$ dopant ions may then stabilize the triplet, making the defect magnetic. Near-degenerate singlet and triplet states are known to occur for certain defects in oxides [13][14]. The general requirement for a ferromagnetic ground state is that the ground state of the charge compensating molecular orbital at the defect be orbitally degenerate, so that a spin triplet state can be formed in the vicinity [15]. The triplets then couple via a spin-polarized 'impurity' band due either to the triplets themselves, or other defects in the film.

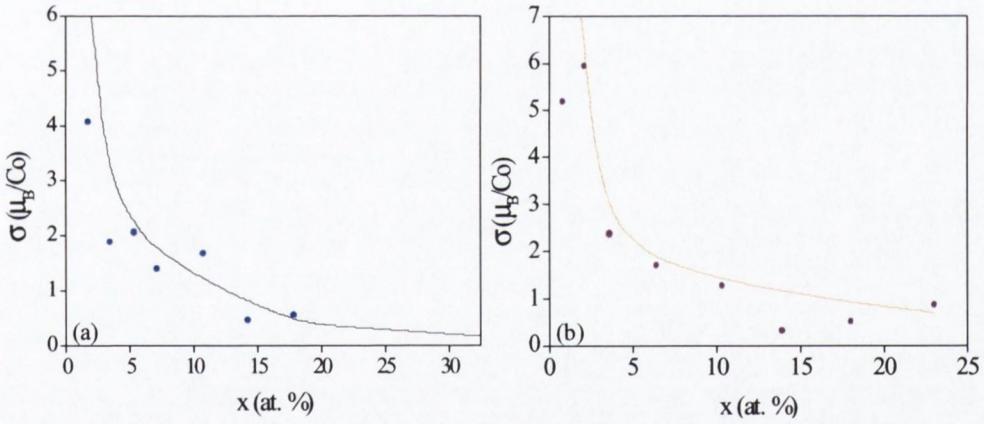


Figure 6.13 The moment per dopant atom versus x in Co-doped (a) SnO_2 and (b) ZnO, with the new fit combining contributions from dopant atoms and defects at the film/substrate interface

As discussed in section 6.2, we found that in all cases the moment extrapolates to 150 - 200 $\mu_B \mathrm{nm}^{-2}$ at $x = 0$ suggesting that defects are somehow responsible. If we add this contribution to what we calculated by assigning moments to the dopant ions distributed across the lattice (in the SnO_2 and ZnO cases) we get a very good fit to the experimental data (figure 6.13) in Co-doped SnO_2 and ZnO systems.

6.5 Conclusion

1. We have presented evidence for defect-induced ferromagnetism in undoped thin films of the high-k dielectric HfO_2.

2. Anisotropy of the saturation magnetisation is a key test to rule out the possibility of secondary ferromagnetic phases.

3. Although no ferromagnetism is observed in undoped SnO_2 or ZnO, it is suggested that magnetic dopants may switch on the defect mechanism, leading to giant magnetic moments exceeding spin-only values in thin films of SnO_2 doped with Mn, Fe or Co and ZnO or HfO_2 doped with Co.

4. The observed magnetisation seems to be the sum of two contributions - one due to transition metal doping and a second (due to defects) which is roughly constant for any film with a value of about 150 - 200 $\mu_B \mathrm{nm}^{-2}$. The defects probably lie in the vicinity of the film/substrate interface. We have been able to model the behaviour of both contributions, resulting in a good fit to the experimental data.

5. A novel exchange mechanism involving donor electrons in a defect related impurity band has been proposed to account for the ferromagnetism of these oxides.

References

[1] Y. Matsumoto, M. Murakami, T. Shono, T. Hasegawa, T. Fukumura, M. Kawasaki, P. Ahmet, T. Chikyow, S. Koshihara and H. Koinuma, Science 291, 854 (2001)

[2] J.-Y. Kim, J.-H. Park, H.-J. Noh, S.-J. Oh, J. S. Yang, D.-H. Kim, S. D. Bu, T.-W. Noh, H.-J. Lin, H.-H. Hsieh and C. T. Chen, Phys. Rev. Lett., **90** 017401 (2003)

[3] K. Ueda, H. Tabata and T. Kawai, Appl. Phys. Lett., **79** 988 (2001)

[4] C. B. Fitzgerald, M. Venkatesan, J. G. Lunney, L. S. Dorneles and J. M. D. Coey, to be published in Applied Surface Science

[5] S.B. Ogale, R.J. Choudhary, J.P. Buban, S.E. Lofland, S.R. Shinde, S.N. Kale, V.N. Kulkarni, J. Higgins, C. Lanci, J.R. Simpson, N.D. Browning, S. Das Sarma, H.D. Drew, R.L. Greene and T. Venkatesan, Phys. Rev. Lett. 91, 077205 (2003)

[6] M. S. Ramachandra Rao, S. Dhar, S. J. Welz, S. B. Ogale, D. C. Kundaliya, S. R. Shinde, S. E. Lofland, C. J. Metting, R. Erni, N. D. Browning and T. Venkatesan, cond-mat/0405378

[7] M. Venkatesan, C. B. Fitzgerald, J. G. Lunney and J. M. D. Coey, cond-mat/0406719 (2004), in press Physical Review Letters

[8] R. J. Kennedy, P. A. Stampe, E. Hu, P. Xiong, S. von Molnár and Y. Xin, Appl. Phys. Lett., **84** 2832 (2004)

[9] J. B. Goodenough, *Magnetism and the Chemical Bond*, Interscience, New York (1963)

[10] J. Yahia, Phys. Rev., **130** 1711 (1963)

[11] A. F. Kohan, D. Ceder, D. Morgan and C. van de Walle, Phys. Rev. B, **61** 15019 (2000)

[12] J. M. D. Coey, M. Venkatesan and C. B. Fitzgerald, submitted to Nature Materials

[13] A. M. Stoneham, Theory of defects in solids, Ch.16, Clarendon Press, Oxford 1975

[14] A. M. Stoneham, A.P. Pathak, R.H. Bartram, J. Phys C 9, 73 (1976)

[15] I. S. Elfimov, S. Yunoki and G. A. Sawatzky, Phys. Rev. Letters **89** 216403 (2002)

Chapter 7

Ferromagnetic carbon

7.1 Introduction

Carbon has a molecular weight of 12.01, a melting point of 3550 °C and a boiling point of 4827 °C. The graphite form of carbon has a simple hexagonal structure (figure 7.1a) with the $P6_3mc$ space group, lattice parameters $a = 2.47$ Å and $c = 6.79$ Å and a density of 2.22 gcm^{-3}. Graphite is a semimetal with good electrical conductivity. The diamond form of carbon has a cubic structure consisting of two interpenetrating face-centred cubic lattices (figure 7.1b) with the Fd3m space group, $a = 3.57$ Å, and a density of 3.52 gcm^{-3}. Diamond has a wide (5.4 eV) indirect bandgap and is an electrical insulator.

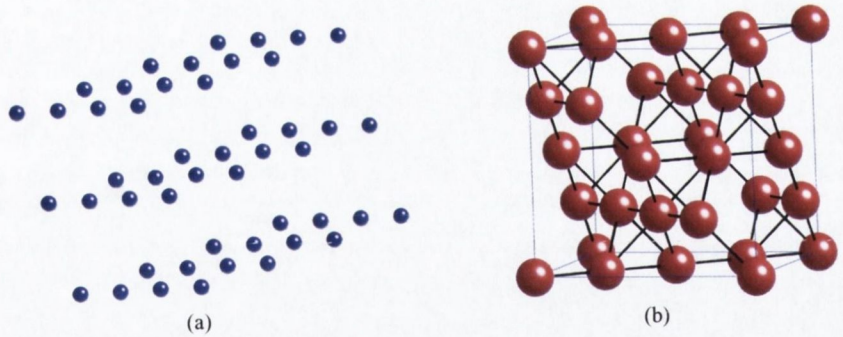


Figure 7.1 (a) The hexagonal graphite structure and (b) the cubic diamond lattice

Ferromagnetism in organic materials was first predicted in the 1960s [1][2] and since then there have been recurrent reports of weak ferromagnetism in graphite [3][4] and synthetic carbon materials such as rhombohedral C_{60} [5]. Others report that ferromagnetism may coexist with superconductivity in the graphite-sulphur system [6], while in addition to predicting ferromagnetism in $p-$type Mn doped II-VI, III-V and oxide materials, Dietl et

al [7] have suggested that diamond should become a ferromagnet with a high Curie temperature, $T_c \sim 480$ K when doped with 5 at. % Mn. Table 1 summarises the experimental results.

	σ_s Am^2kg^{-1}	μ_B/C	T_c (K)	Reference
HOPG	0.003 (RT)	0.000006	> 500	P. Esquinazi et al, (2002) [3]
Rh-C_{60}	0.09 (RT)	0.0002	~ 500	T. L. Makarova et al, (2001) [5]
Graphite-sulphur system	0.02	0.00004		S. Moehlecke et al [6]
Pyrolysed carbon	36.2 (4.5 K)	0.072		K. Murata et al, (1996) [8]
C/Fe multilayer		0.05	> 300	H. Mertins et al, (2004) [9]

Table 1.Summary of reported ferromagnetism in carbon materials, where RT indicates room temperature measurements

The weakness and variability of the moments, together with doubts as to the purity of the samples, has led to many of the reports being dismissed. We decided to take a very different approach to the problem and have examined meteoritic graphite and carbonado samples. They have experienced temperatures and pressures which cannot be re-created in a laboratory environment. While both have metallic, and even ferromagnetic, impurities we have been able to separate their contributions to the magnetisation from those of carbon.

Carbon which is ferromagnetic at room temperature could be very useful to the spin electronics community. Combining the unusual properties encountered in the different carbon forms - the strength and stability of a carbon nanotube, excellent thermal conductivity and extreme hardness in diamond - with ferromagnetism could open up many more device opportunities.

7.2 The Canyon Diablo meteorite

The impact some 50,000 years ago of the 50,000 tonne Canyon Diablo meteorite at a relative velocity of about 20 kms^{-1} created a crater of diameter 1.3 km in the Arizona desert (figure 7.2a). Canyon Diablo is classified as a silicate-bearing IAB iron [10][11]. The

origin of this group is uncertain, but it may have involved mixing of the molten iron core of an asteroid in a collision with a chondritic body in the first few million years of the solar system. The IAB group exhibit enormous heterogeneity in their range of inclusions. Rounded graphite-rich nodules are a particular feature of the Canyon Diablo meteorite.

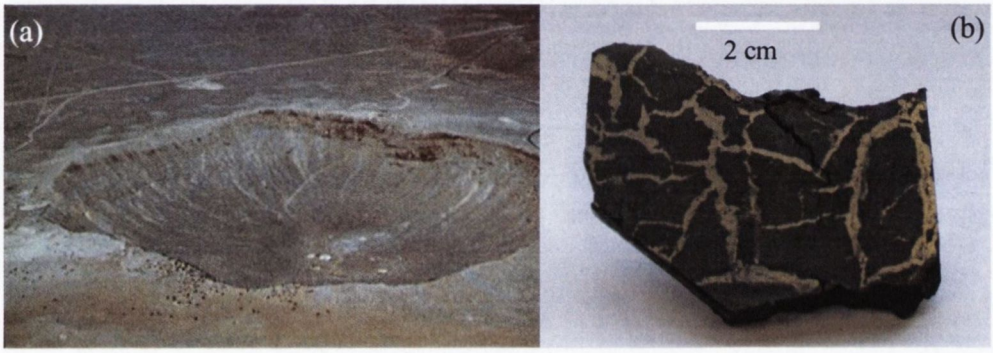


Figure 7.2 (a) The Canyon Diablo crater in the Arizona desert and (b) a section of the graphite nodule from the Canyon Diablo meteorite that was studied

Figure 7.2b shows a cut and polished section of the graphite nodule which was studied, with interconnecting veins of kamacite ($Fe_{94}Ni_6$) visible in the graphite matrix. Appendix A contains a table listing mineral names and their chemical compositions. The sample corrodes in ambient humidity and is stored in a dessicator, and was obtained from The Mineralogical Research Company, San Jose, California.

7.2.1 Optical microscopy and scanning electron microscopy

Several small pieces were removed from the nodule, polished and examined by optical microscopy - figure 7.3 a and b. The graphite is crossed by a network of metal veins roughly 1 mm wide and 5 - 10 mm apart. Metal also occurs as embayed nuggets < 50 μm across, lightly peppering the graphite.

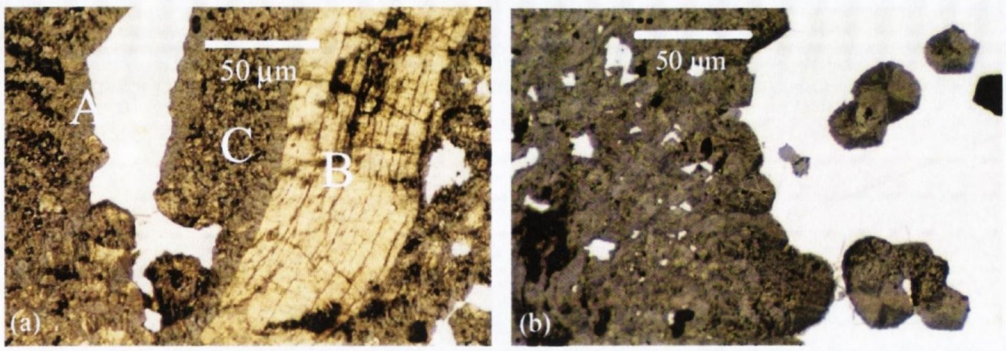


Figure 7.3 (a) Reflected polarised light image of the polished meteorite showing graphite with three distinct morphologies A, B and C and (b) cliftonite inclusions in kamacite

The graphite exhibits three distinct morphologies - A, B and C in figure 7.3a. 'A' is an inclusion-free zone, usually 30 - 50 μm wide, which borders the veins and larger nuggets of metal. 'B' are large plates of graphite up to 500 μm long, with skeletal grains of magnesium silicate. The plates, which are strained and buckled, are usually surrounded by small, randomly arranged grains of porous graphite - 'C'. Less commonly they are bordered by cliftonite, which is a polycrystalline aggregate of graphite with cubic morphology, thought to be exsolved from carbon-rich metal on cooling [12]. Cliftonite is also found as inclusions in the metal nuggets as it forms by precipitation within them, as seen in figure 7.3b.

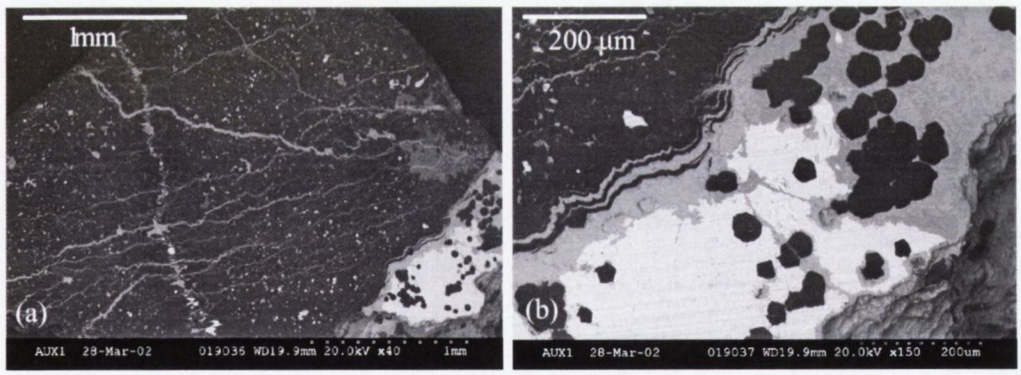


Figure 7.4 (a) An SEM image of the graphite nodule with metal veins and inclusions clearly visible and (b) cliftonite inclusions in kamacite

SEM images again show the metal veins and inclusions in the graphite matrix - figure 7.4a - and cliftonite inclusions in the metal - 7.4b. Carbon, iron, nickel, sulphur, phosphorous,

magnesium, silicon, aluminium, calcium and potassium were all found by EDAX analysis. The metal veins and many of the metal inclusions were found to be kamacite, while some nickel-free inclusions could be identified as magnetite. The graphite matrix was always found to contain traces of Fe. Small amounts of schreibersite $(Fe_{2.0}Ni_{1.0})P$, troilite (FeS) and enstatite (Mg_2SiO_3) were also identified in the nodule.

7.2.2 Structural and compositional analysis

Ten graphite samples of 100 - 500 mg were selected for further analysis. The mass of each sample was measured in air, M_1, and in water, M_2, and the density, $\rho_{graphite}$, calculated as $\rho_{graphite} = M_1\rho_{water}/(M_1\text{-}M_2)$, where $\rho_{water} = 1$ gcm^{-3}. The measured densities range from 2400 - 3600 kgm^{-3} and are greater than the x-ray density of graphite which is 2260 kgm^{-3}. This is consistent with the presence of the heavier metal phases identified by microscopy. Part of each sample was then ground to powder in an agate mortar, where any obvious kamacite nuggets were removed.

A typical XRD pattern of the powdered samples is shown in figure 7.5, with graphite/cliftonite (C), magnetite (M), kamacite (K), akaganéite (A) and haematite (H) peaks identified.

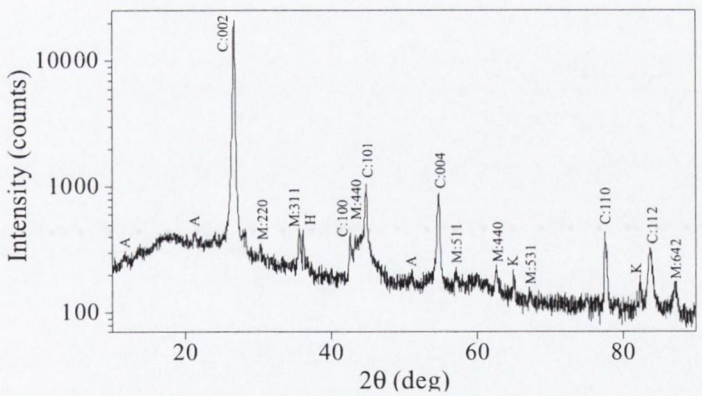


Figure 7.5 A typical XRD pattern of a powdered meteorite sample. The peaks belong to graphite/cliftonite (C), magnetite (M), kamacite (K), akaganéite (A) and haematite (H).

The unit cell in graphite is about 1 % shorter in both a and c directions than usual,

with lattice parameters a_o = 0.2450 (5) nm, c = 0.6713 (5) nm, but neither c-axis nor basal-plane reflections are anomously broad. Neither is there any indication of intercalation or poor crystallinity on the nanometer scale. The unit cell in magnetite is about 0.35 % shorter than usual, with a = 8.363 (5) nm.

Using the Scherrer formula,

$$B(2\theta) = \frac{0.94\lambda}{L\cos\theta} \tag{7.1}$$

where λ = 1.5406 Å, L is the crystal dimension and B(2θ) is the full width in radians subtended by the half maximum intensity width of the pattern peak, a grain size of 40 nm was estimated for both graphite and magnetite.

A powdered sample, of mass > 1 g, was analysed by Activation Laboratories in Canada. The results can be seen in Table 2. The data are the average of three separate analyses.

Element/oxide	**Weight %**
C	51.8
S	0.09
P	0.12
$FeO_{1.12}$	41.6
NiO	2.50
CoO	0.21
SiO_2	1.70
Al_2O_3	0.19
MnO	<0.01
MgO	0.49
CaO	0.06
Na_2O	0.02
K_2O	0.02
TiO_2	0.01

Table 2.Chemical analysis of Canyon Diablo sample

7.2.3 Magnetic properties

Each part of every sample was found to be strongly magnetic, jumping to a small

ferrite magnet, with magnetisation curves similar to the one shown in figure 7.6a. Values of σ_s for the ten powder samples range from 21 - 70 Am^2kg^{-1}. There is a little hysteresis, with coercivity $\mu_o H_c$ in the range 6 - 14 mT, as seen in figure 7.6b.

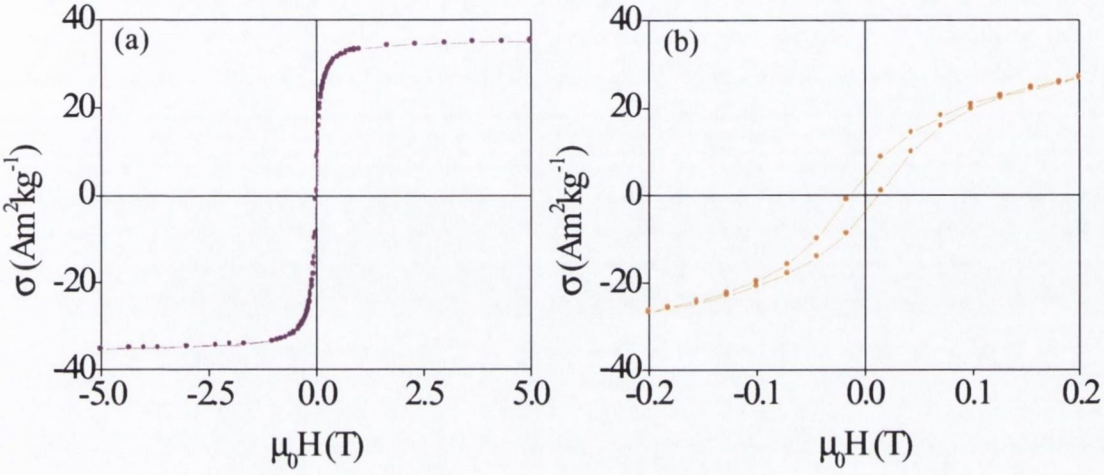


Figure 7.6 (a) A typical powdered meteorite room temperature magnetisation curve and (b) coercivity in the sample

Several small fragments (1 - 10 mg) were selected from the samples in order to investigate the variability of the magnetisation. The range found was 6 - 185 Am^2kg^{-1}, the latter being measured on a kamacite nugget. Of the iron-rich minerals present, magnetite, kamacite and schreibersite are intrinsically ferromagnetic or ferrimagnetic, troilite and haematite are antiferromagnetic and akaganéite is paramagnetic at room temperature.

Approximately 100 mg from several of the powder samples was placed in a platinum crucible and heated in a furnace to 1200 °C for 6 hours and the loss on ignition measured. This method slightly underestimates the loss of carbon, as iron present in the sample will increase in mass as it is oxidised. The loss on ignition (LOI) ranged from 28.5 - 74.9 %, and there was a significant drop in the moment of the samples after heat treatment as shown in figure 7.7.

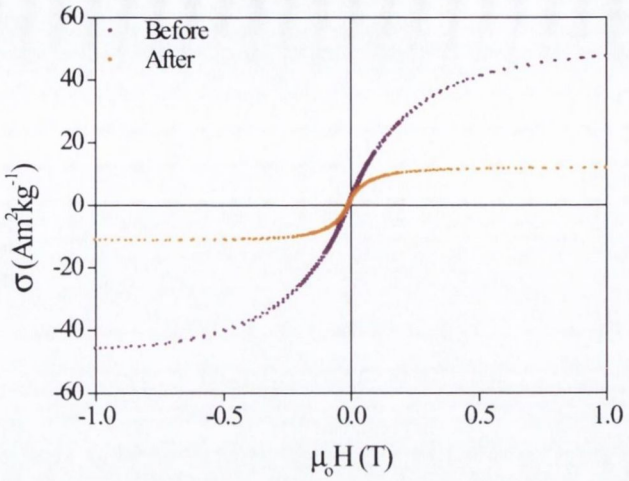


Figure 7.7 The magnetisation curves of a powdered sample before (purple) and after (orange) heat treatment

Curie temperatures (T_c) were determined from thermogravimetric scans in a magnetic field gradient as seen in figure 7.8. The two sharp transitions at 1030 K and 860 K correspond to T_c for kamacite and magnetite respectively, and the broad decrease in magnetisation at around 570 K is attributed to ferromagnetic graphite.

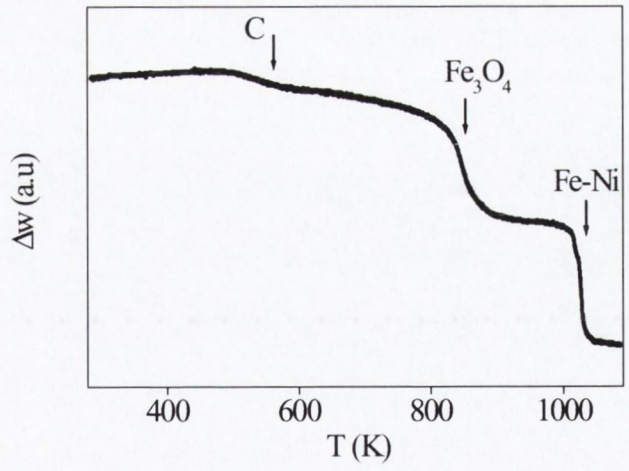


Figure 7.8 A thermomagnetic scan of the meteorite powder showing Curie temperature transitions for carbon, magnetite and kamacite

MFM studies suggest that some domain structure is seen in the graphitic areas of the

meteorite. Figure 7.9a is an optical microscope image of the meteorite with a box marking the area studied by AFM (7.9b) and MFM (7.9c). In this case clear domain structure is seen in the kamacite regions of the MFM, but not so clearly in the cliftonite or graphite. However, in the area outlined in 7.9d domain structure is seen in the kamacite inclusions but magnetic contrast is also seen in the graphite area (7.9f).

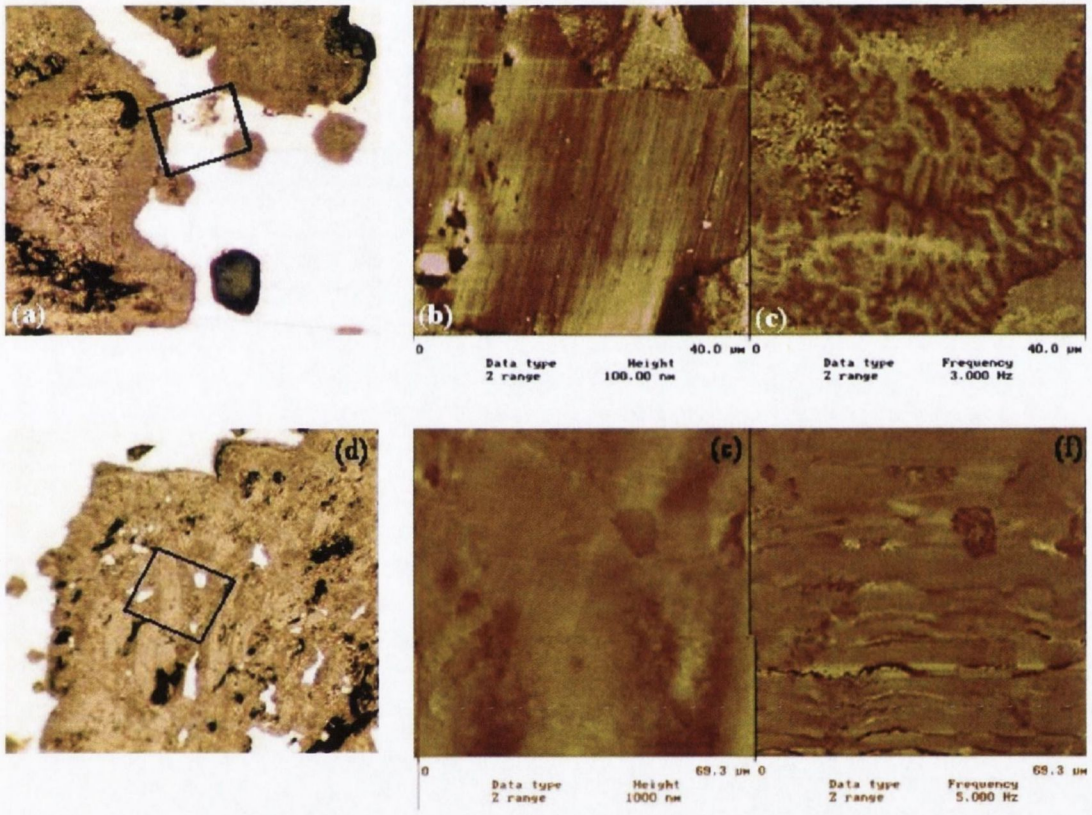


Figure 7.9 (a) An optical microscope image of the meteorite with the area studied by AFM (b) and MFM (c) marked with a black box. Similarly the are marked on (d) is the area studied by AFM (e) and MFM (f)

In Table 3, the weight percentage of the ferromagnetic minerals in each of the graphitic samples is listed, together with their combined contribution to the magnetization, σ_{imp}, calculated by assuming values of 75, 216 and 100 Am^2kg^{-1} for oxidised magnetite, kamacite and schreibersite, respectively.

Sample	ρ (kg m^{-3})	σ_s (Am^{2}kg^{-1})	LOI %	C (wt.%)	Fe (wt.%)	Fe_3O_4 (wt.%)	$Fe_{94}Ni_6$ (wt.%)	$(Fe_{2.0}Ni_{1.0})P$ 'nc iron' (wt.%)	σ_{imp} (Am^{2}kg^{-1})	$\Delta\sigma$ (Am^{2}kg^{-1})	σ_c (Am^{2}kg^{-1})
1.1	nd	70.0	51.8	54.2	31.8	26.2	6.3	0.0	33.3	36.7	67.7
1.2	nd	30.0	43.9	48.5	36.4	27.0	0.0	9.8	30.1	-	-0.2
1.3	2630	30.5	74.9	69.8	18.8	6.1	7.8	0.4	21.8	8.7	12.5
1.4	3040	28.7	46.5	51.5	32.0	15.6	3.6	9.1	28.6	0.1	0.2
1.5	3010	41.5	46.2	46.2	43.5	15.8	7.2	9.1	36.6	4.9	10.6
1.6	2430	25.9	62.6	66.1	23.3	15.4	4.3	3.6	24.5	1.4	2.1
1.7	3350	51.5	28.5	39.8	44.0	16.5	6.2	6.4	32.2	19.3	48.5
1.8	3380	38.4	51.8	54.4	29.0	9.6	5.2	3.6	22.0	16.4	30.1
1.9	3360	62.3	29.0	36.7	44.8	19.6	9.8	8.3	44.2	18.1	49.3
1.10	3650	21.2	53.8	56.0	28.5	11.0	3.2	4.6	19.8	1.4	2.5
Average (SD)	**3106 (412)**	**40.6 (13.1)**		**52.1 (11.7)**	**34.2 (10.5)**				**29.7 (7.0)**	**10.8 (9.5)**	**23.1 (21.5)**

Table 3 Ferromagnetic properties and related data for samples from the Canyon Diablo graphite nodule.

The weight percent of these minerals was derived by distributing the total iron among the phases in proportion to their Mössbauer absorption areas [13] (or in the case of $(Fe_{2.0}Ni_{1.0})P$, based on the P content). Experimental uncertainties are given in parentheses. The observed magnetization, σ_s, in Table 3 significantly exceeds σ_{imp} in six out of ten samples, even allowing for a nanocrystalline iron phosphorous phase ('nc iron'), with magnetisation of 100 Am^2kg^{-1}. The average value of σ_s weighted by sample mass (40.6 Am^2kg^{-1}) is 38 % greater than that of σ_{imp} (29.7 Am^2kg^{-1}). Attributing the difference $\Delta\sigma = \sigma_s - \sigma_{imp}$ to the graphite, we find an average magnetization σ_c of 23.1 Am^2kg^{-1}, which corresponds to 0.05 μ_B/carbon atom. If this ferromagnetic 'nc iron' is not present, and there is good reason from Mössbauer data to believe it is not, these numbers will be 40 % greater. In figure 7.10 the contribution to the magnetisation of the ferromagnetic phases for each sample is outlined. The unshaded residue is associated with graphite.

That the magnetization of the graphitic material significantly exceeds anything that can be attributed to the iron-rich phases does not rest on the details of the phase analysis. For example, sample 1.7 contains 44 wt. % iron according to the chemical analysis. Of this, only 38 % is magnetically ordered. Even if it was all pure iron (σ_s = 220 Am^2kg^{-1}), the

magnetization would only be 37 Am^2kg^{-1}, compared with the 52 Am^2kg^{-1} measured on the same powder.

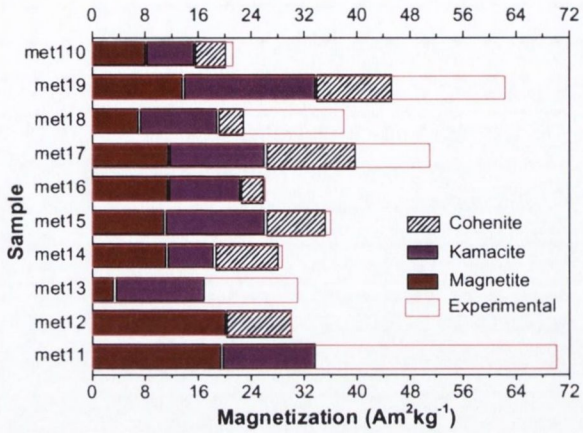


Figure 7.10 Contribution to the magnetisation of the ferromagnetic phases (shaded: 'nc iron' is probably overestimated, as this phase is likely to be antiferromagnetic). The unshaded residue is associated with graphite.

The density, ρ, sets another limit of 38 Am^2kg^{-1} for this sample, assuming a mixture of graphite and iron. Furthermore, extrapolation of σ_s vs ρ for 17 specimens (figure 7.11) gives a completely independent value of the average magnetization, 21 (13) Am^2kg^{-1} at the density of graphite.

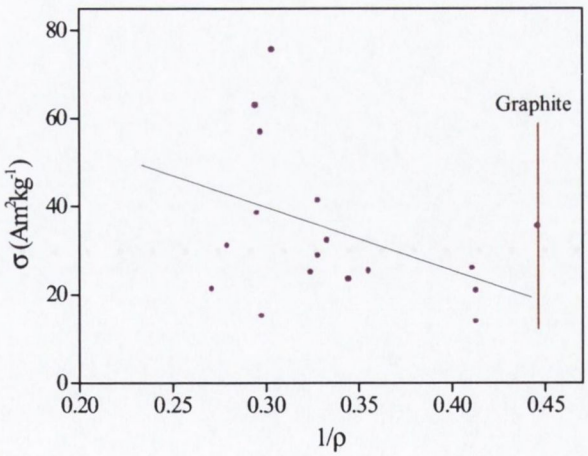


Figure 7.11 Extrapolation of σ_s versus $1/\rho$ for 17 specimens. $1/\rho$ of graphite is marked with a solid line.

7.3 Carbonados

Carbonados are sintered polycrystalline microdiamond aggregates, with a porous, ceramic texture and a melt-like surface patina, and are found in alluvial deposits of the Central African Republic and the Bahia Province of Brazil. Their origin is uncertain, but several hypotheses have been proposed, ranging from extraterrestrial, to crustal and mantle provenances. A meteoritic impact in the Precambrian onto carbon-rich crustal material could account for both the Brazilian and African occurrences, as the continents were then unseparated [14][15][16]. Carbonados have been identified in graphite nodules from Canyon Diablo [17] and other meteorites. Alternative, extraterrestrial origins that have been suggested including the possibility that they originated outside the solar system as ejecta from a collapsing red giant star [18]. It has also been theorised that the carbonados originated on Earth. They may have formed in cold subduction slabs near continental margins [19], which could provide the high pressures needed to produce them, or in the Earths mantle, as they are similar in several ways to kimberlites [20]. The alluvial deposits in which they are found are $\sim$ 1.5 x 10^9 years old (1.5 Ga), while the carbonados are between 2.6 and 3.8 Ga. They are commonly intergrown with haematite and magnetite, while the diamond matrix contains small amounts of α-Fe, Ni, Cr, Fe-Mn, Ti, SiC and taenite γ-(Fe, Ni).

It has been reported that carbonados exhibit saturation magnetisation in the range 10^{-4} to 10^{-2} Am^2kg^{-1} [21], although most of the magnetisation is lost following acid treatment. From the variation of the ferromagnetic signal on acid leaching, it was concluded that the ferromagnetism was mostly associated with the surface and open pores, rather than the bulk of the material.

In this study the carbonados were of Brazilian origin, supplied by Shannon Abrasives

Ltd., Shannon, Co. Clare, Ireland. Masses were in the range 3 – 20 mg. They are different shades of grey in colour as seen in figure 7.12. Many, but not all, samples respond to a small rare-earth magnet.



Figure 7.12 Several carbonados beside a one cent coin

7.3.1 Structural and compositional analysis

SEM images show the distribution of heavy metals to be inhomogeneous, concentrated in the pores. Fe and Co inclusions are seen as bright spots in the diamond in the images in figure 7.13 .

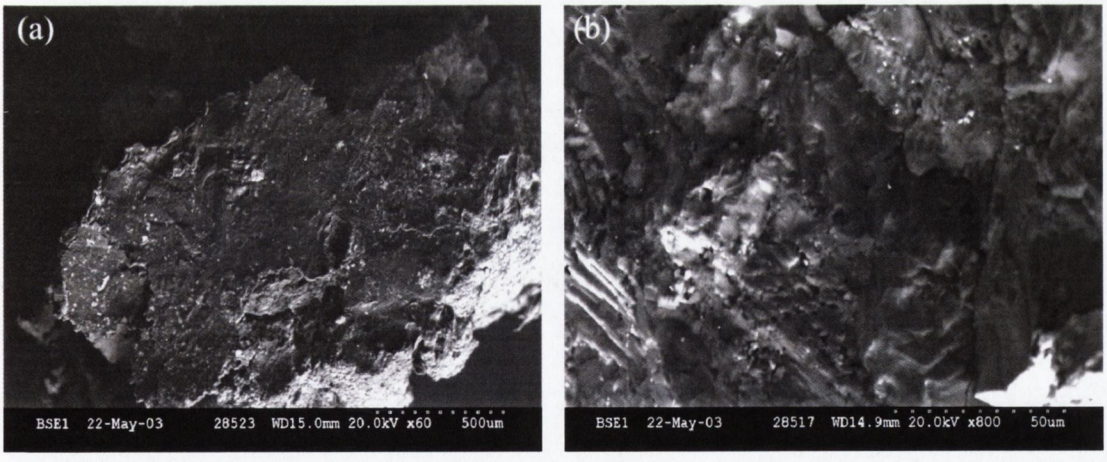


Figure 7.13 SEM images of the surface of carboando samples. The bright areas are Fe and Co inclusions in the diamond

The main impurities identified by EDAX were iron and cobalt, potassium, calcium,

silicon, aluminium and sulphur, and less commonly copper, chlorine and titanium, with the results of 14 analyses summaried in Table 4. While many of these impurities have been widely reported previously, cobalt has not been found before.

	1	2	3	4	5	6	7	8	9	10	11	12	13	14
C	98.91	98.31	98.79	39.84	58.39	47.29	64.49	62.29	70.25	88.21	76.13	76.83	55.34	92.70
Al	0.42	0.52	0.41	0.30	0.54	0.32	2.71	0.56	-	0.29	0.29	0.21	0.01	0.26
Si	0.05	0.06	0.04	0.08	0.27	0.88	1.77	0.90	-	-	-	-	-	-
P	-	0.16	0.04	-	-	-	-	-	-	-	-	-	-	-
S	-	0.03	0.07	-	1.66	0.88	-	9.59	-	-	-	-	-	-
Cl	-	-	-	0.08	1.43	0.68	0.39	-	-	-	-	-	1.41	0.35
K	-	0.02	-	-	0.02	0.09	3.19	0.58	-	-	-	-	-	-
Ca	-	0.23	0.11	0.09	1.44	3.01	-	-	-	-	-	-	-	-
Ti	-	-	-	0.21	-	-	0.87	0.23	-	-	-	-	-	-
Cr	-	-	-	-	-	-	-	-	5.94	-	-	-	-	-
Mn	-	-	-	0.11	-	-	-	-	0.64	-	-	-	-	-
Fe	0.63	0.67	0.57	13.33	0.75	1.10	7.02	17.38	20.80	10.14	5.55	12.47	7.16	0.15
Co	0.02	0.01	-	-	-	-	-	-	-	-	-	-	-	-
Ni	-	-	-	34.80	-	0.15	-	-	2.38	-	-	-	-	-
Cu	-	-	-	-	18.33	0.20	-	0.20	-	0.43	0.25	0.16	0.04	-
Zn	-	-	-	-	3.85	-	-	-	-	0.89	-	-	-	-
Ag	-	-	-	-	-	-	-	-	-	-	-	-	-	6.48
Ba	-	-	-	-	0.69	4.15	-	-	-	-	-	-	-	-

Table 3.The results of 14 EDAX analyses on carbonado samples

The XRD spectrum of crushed carbonado powder is shown in figure 7.14. It shows the cubic diamond structure with (111) and (220) reflections and $a = 3.56$ Å. No other phases are visible.

7.3.2 Magnetic properties

Magnetization curves for six samples at room temperature are shown in figure 7.15a. All show a ferromagnetic signal, which corresponds to a spontaneous magnetization M_s in the range 0.25 – 3 Am^2kg^{-1}, and a diamagnetic background. In order to remove any associated phases, the diamonds were treated in aqua-regia solution for 24 hours. The samples were then rinsed twice in water and placed in an acetone bath. Analysis after acid treatment

showed that many of the impurities had been removed from the surface and open pores, but that a substantial amount remained. The samples were then re-measured in the SQUID.

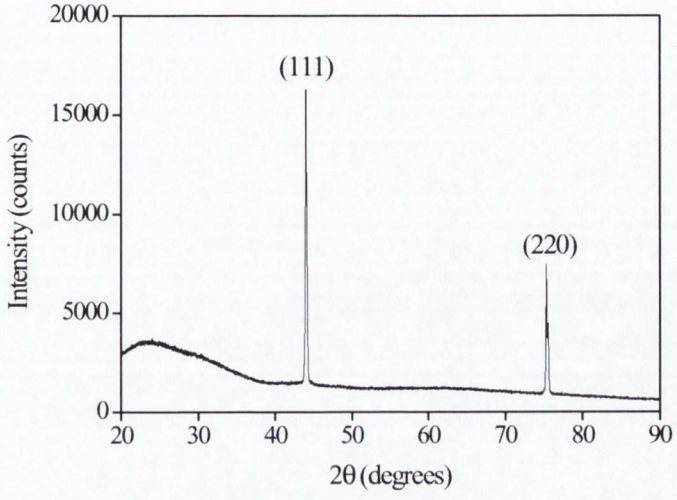


Figure 7.14 The XRD spectrum of a crushed carbonado

After the acid treatment, the signal is significantly reduced for some of the samples - figure 7.15b. It is clear that part of the magnetization is associated with surface or open pore material, rather than the bulk of the carbonados themselves.

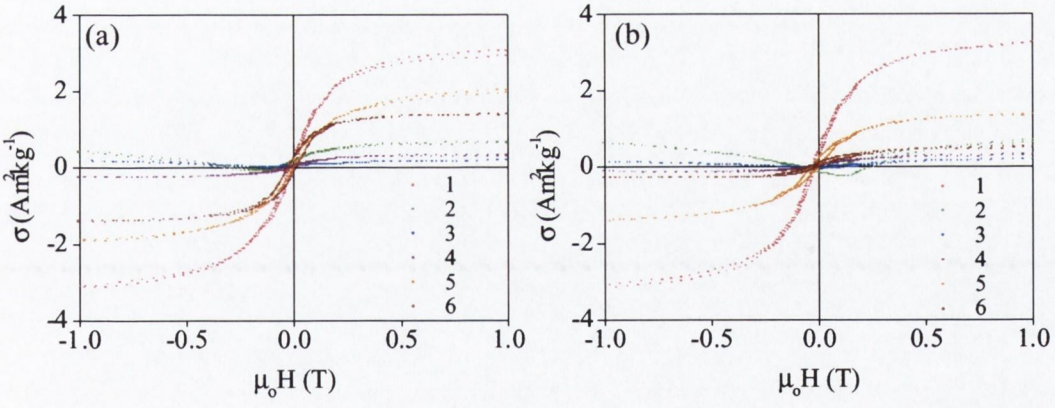


Figure 7.15 The magnetisation curves of six carbonados (a) before acid treatment and (b) after acid treatment

The magnetisation of sample 1 is almost unaffected by the acid treatment and so it was

chosen for Curie temperature measurements. The magnetisation was measured as a function of temperature, data below 300 K being taken in the SQUID magnetometer (figure 7.16a), and a high temperature furnace attachment used to measure up to 800 K (figure 7.16b). The results indicate that the Curie temperature, T_c, exceeds 800 K.

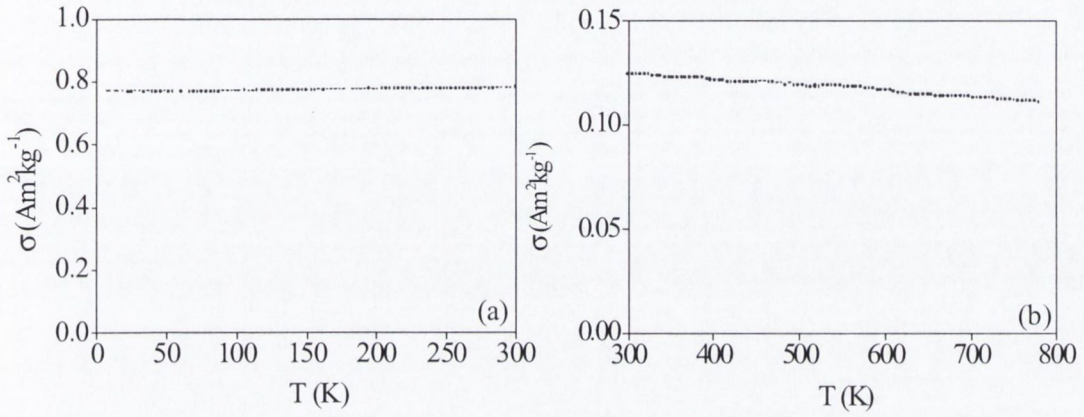


Figure 7.16 Magnetisation as a function of temperature for sample 1 (a) measured in the SQUID magnetometer and (b) using the high temperature furnace attachment

A Curie temperature of 570 K associated with ferromagnetic graphite was tentatively identified in the meteorite samples, but no such transition is seen for the carbonado samples. Instead the Curie temperature of the ferromagnetic phase present exceeds 800 K. This phase is most likely metallic iron, with a T_c of 1043 K. Confirmation that the ferromagnetism of the carbonados is essentially due to the inclusions of ferromagnetic iron is provided by Mössbauer spectra.

While some iron is trapped in open pores of the carbonado surface and can be removed using acid treaments, it is likely that some is also trapped in enclosed pores from which it cannot be leached. It is difficult to estimate the amount of iron contained in these pores, but this is most likely responsible for the ferromagnetic signal. We find no evidence from the carbonados for the existence of transition-metal doped ferromagnetic carbon. Instead

the ferromagnetism is associated with inclusions of metallic iron or cobalt.

7.4 Discussion

Both graphite nodules from the Canyon Diablo meteorite and carbonados from Brazil are ferromagnetic at room temperature. There is no doubt that they both contain ferromagnetic impurities, but the question is whether they are present in sufficient quantities to explain the magnetisation data. In the case of the meteorite we find that impurities alone cannot account for the observed moment, but we find that ferromagnetism in carbonados is associated with inclusions of metallic iron. Much of the iron is included in closed pores from which it cannot be leached.

So how does the ferromagnetism in meteoritic carbon come about? One idea is that meteoritic graphite is somehow different from terrestrial graphite, due perhaps to its mode of formation, chemical doping (Fe, S, P, N...), or the shock of impact. Defects tend to enhance the susceptibility of graphite, and may even lead to ferromagnetism [22] (and possible superconductivity [23]). There are theoretical reports that graphene strips a few nanometers in width show an unusual density of states which leads to local moments at the strip edges which are paramagnetic [24], or, with a suitable stacking, antiferromagnetic [25]. But there have been no suggestions that nanographite should be ferromagnetic. Ferromagnetism would not normally be expected in graphite, a semi-metal with Fermi energy $E_F \sim 20$ meV, where the Fermi level falls at a sharp minimum in the density of states [26]. Nor is there any indication on the x-ray patterns of intercalation or poor crystallinity on the nanometer scale. The unit cell is about 1 % shorter in both a and c directions than usual, with lattice parameters $a = 0.2450\ (5)$ nm, $c = 0.6713\ (5)$ nm, but neither c-axis nor basal-plane reflections are anomalously broad. EDAX analysis of the graphite regions shows no heavy

element other than iron at the 0.1 wt % level.

Another idea is that the ferromagnetic inclusions somehow induce a moment in the graphite. Scanning electron micrographs indicate that magnetite and kamacite particles of all sizes down to 50 nm or less are individually embedded in graphite. Perfectly-encapsulated particles are not removed by acid treatment. Since magnetite is a half-metal [27], matching the chemical potential of the $\uparrow$ and $\downarrow$ electrons at the interface leads to complete spin polarization of the adjacent carbon atoms. If the spin splitting of the graphite bands at the Fe_3O_4 interface is a few tenths of an electron volt, the Fermi level there falls in a higher density of states, tending to sustain the spin polarization.

Meteoritic graphite is ferromagnetic with an average magnetization of 23 Am^2kg^{-1}, or 0.05 Bohr magnetons (μ_B) per carbon atom. The implications of ferromagnetic carbon, whatever its origin, are likely to be wide-reaching. Potentially, we have a new, zero-gap high-temperature ferromagnetic semiconductor.

Appendix A
Mineral names and their chemical compositions

Mineral name	Chemical composition
Akaganéite	βFeOOH:Cl
Cohenite	Fe_3C
Enstatite	Mg_2SiO_3
Haematite	Fe_2O_3
Kamacite	$Fe_{94}Ni_6$
Magnetite	Fe_3O_4
Schreibersite	$(Fe_{2.0}Ni_{1.0})P$
Troilite	FeS

Table 4.Mineral names and compositions

References

[1] H. M. McConnell, J. Chem. Phys., **39** 1910 (1963)

[2] N. Mataga, Theoret. Chim. Acta, **10** 372 (1968)

[3] P. Esquinazi, A. Setzer, R. Hohne, C. Semmelhack, Y. Kopelevich, D. Spemann, T. Butz, B. Kohlstrunk, M. Losche, Phys. Rev. B, **66** 024429 (2002)

[4] R. Höhne and P. Esquinazi, Adv. Mater., **14** 753 (2002)

[5] T. L. Makarova et al, Nature **413** 716 (2001)

[6] S. Moehlecke, P. C. Ho, M. B. Maple, Philosophical Magazine B, **82** 1335 (2002)

[7] T. Dietl, H. Ohno, F. Matsukura, J. Cibert and D. Ferrand, Science **287**, 1019 (2000)

[8] K. Murata and H. Ushijima, J. Appl. Phys., **79** 978 (1996)

[9] H.-Ch. Mertins, S. Valencia, W. Gudat, P. M. Oppeneer, O. Zaharko and H. Grimmer, Europhys. Lett., **66** 743 (2004)

[10] Grady M. M., Catalogue of Meteorite 5th edition (British Museum, Natural History) pp 89 - 90 (2000)

[11] Papike J. J., (editor) Planetary Materials Reviews in Mineralogy vol 35 (The mineralogical Society of America, Washington DC) 1998

[12] R. Brett and G. T. Higgins, Cliftonite: A proposed origin, and its bearing on the origin of diamonds in meteorites, Geochimica at Cosmochimica Acta, 33, 1473-1484 (1969)

[13] J. M. D. Coey, M. Venkatesan, C. B. Fitzgerald, A. P. Douvalis and I. S. Sanders, Nature, **420** 156 (2002)

[14] J. V. Smith, J. B. Dawson, Geology **13** 342-3 (1985)

[15] D. Shelkov et al, Lunar Planet. Sci. **26** 1281-2 (1995)

[16] S. Master, 61st Annual Meteoritical Society Meeting, Abstract

[17] K. J. Ksandra and E.P. Henderson, Amer. Miner. **24** 677 (1939)

[18] S. A. Haggerty EOS Trans, AGU Supp. S143 (1996)

[19] D. N. Robinson, Mineral. Sci. Eng. **10** 55 (1978)

[20] H. Kagi et al, Geochim. Cosmochim. Acta **58** 2629 (1994)

[21] G. Kletetschka et al, Earth and Planetary Science Letters, Vol. **181**, Issue 3, 279 (2000)

[22] P. Esquinazi, D. Spemann, R. Hohne, A. Setzer, K. H. Han, T. Butz, Phys. Rev. Lett., **91** 227201 (2003)

[23] J. González, F. Guinea and M. A. H. Vozmediano, Phys. Rev. B **63** 134421 (2001)

[24] K. Wakabayashi, M. Jujita, H. Ajiki and M. Sigrist, Physica B **280**, 388 (2000)

[25] K. Harigaya, J. Phys.: Condens. Matter **13**, 1295 (2001)

[26] B. T. Kelly, Physics of Graphite, Applied Science Publishers, London (1981)

[27] J. M. D. Coey and M. Venkatesan, J. Appl. Phys **91** 8345 (2002)

Chapter 8

Further work

8.1 Dilute magnetic oxides

Ferromagnetism in dilute magnetic oxides may prove to be one of the most interesting new problems in magnetism to emerge this century. Our understanding of these materials is sure to advance at a rapid pace given their importance in the field of spin electronics. The main stumbling block in II-VI and III-V systems has been achieving Curie temperatures above room temperature - which are regularly achieved in the oxide materials. The results were so unexpected initially that explanations were sought in terms of phase segregation - and in some cases ferromagnetic impurity phases were responsible [1] - but this cannot now be accepted as a general explanation. However, until a clear connection between the magnetic properties and electronic structure can be demonstrated, doubts about sample purity will persist. This is because the often performed magnetisation measurements are unable to distinguish an intrinsic ferromagnetic signal from an extrinsic one, as this method probes all of the magnetisation from both sources. The intrinsic ferromagnetism is caused by spin-polarised charge carriers that mediate ferromagnetic exchange interaction between distant localised spins of magnetic impurities. Hence the ferromagnetic response caused by the charge carriers can be a direct manifestation of intrinsic ferromagnetism. A well known ferromagnetic response of charge carriers in ferromagnetic semiconductors is the Anomalous Hall Effect (AHE). Anomalous Hall Effect controlled by charge carriers in a room temperature ferromagnetic semiconductor would be strong evidence of intrinsic ferromagnetism and also an important milestone towards the realisation of semiconductor spin-electronics de-

vices operable at room temperature. Anomalous Hall Effect measurements have recently revealed the magnetic interaction between itinerant charge carriers and the localised Mn spins in $In_{1.7}Sn_{0.2}Mn_{0.1}O_{3-\delta}$ thin films [2] and Co spins in Co-doped TiO_2 [3] - a unique feature of magnetic semiconductors. Measurements of this type are needed for all of these oxide systems. We also believe that measurements of the anisotropy of the saturation magnetisation is a key test to rule out secondary ferromagnetic phases. It is a challenge to explain the huge anisotropy, which may reflect the presence of persistent orbital currents due to unpaired electrons in extended molecular orbitals associated with the defects. A measurement of optical magnetic circular dichroism (O-MCD) or spin-polarized photoemission should be able to resolve the question of whether the donor electrons mediating the exchange occupy an impurity band or a spin-split conduction band.

Efforts should be made to verify our belief that there are two separate contributions to ferromagnetism in dilute magnetic oxide thin films - the first due to the formation of magnetic polarons by defects resulting in a spin-split impurity band, and the second due to defects at the film/substrate interface - and to probe the predictions made recently by Coey et al [4] in their model for high-temperature ferromagnetism in dilute n-type magnetic semiconductors.

Experimental studies have outpaced theoretical work in these systems, and requires some focus. Electronic structure calculations are needed to define the role of defects and evaluate the d character acquired by the impurity-band defect states on hybridisation with the transition metal $3d$ states, in order to elucidate the nature and extent of the orbital moment. Detailed application of an impurity-band model requires a knowledge of the defect states at the interface, and appropriate electronic-structure calculations, but such a model

can account, at least qualitatively, for the paradoxical d^o ferromagnetism of HfO_2 and Sc-doped ZnO.

High resolution TEM and nanoscale SIMS are required for interface studies, lattice imaging and precise compositional analysis.

Further challenges are to tune the ferromagnetic properties of the oxides by modifying the donor concentration by compensation, or by the use of a gate electrode, and increasing the mobility of the spin-polarised F-center electrons, and developing the link with high-k dielectrics.

Finally, the present results suggest a new focus for the search for new ferromagnetic semiconductors and insulators – oxides with d^o cations. There may be no need to substitute magnetic ions into certain nonmagnetic matrices in order to make them ferromagnetic. In the case of HfO_2, when insignificant amounts of magnetic ions are present, it seems it is sufficient to have the right kind of defects.

8.2 Ferromagnetic carbon

Potentially, we have a new, zero-gap high-temperature ferromagnetic semiconductor in carbon. We have found that meteoritic graphite is ferromagnetic, and have suggested that it may be due to its mode of formation, chemical doping (Fe, S, P, N...), or the shock of impact - or that ferromagnetic inclusions may somehow induce a moment in the graphite. While there have been recurrent reports of weak ferromagnetism in graphite [5][6] and synthetic carbon materials such as rhombohedral C_{60} [7] since the first predictions in the 1960's, the approach has been quite haphazard. The detected magnetic signals of carbon are typically very weak and so it is difficult to rule out a parasitic signal of magnetic impurities. Techniques which allow a moment on carbon to be unambiguously distinguished from that

on any impurities - for example x-ray magneto-optical reflectivity of polarised synchrotron radiation - need to be used in an extensive study of HOPG, pyrolysed carbon, C_{60}, and carbon nanotubes and multilayers.

References

[1] J.-Y. Kim, J.-H. Park, H.-J. Noh, S.-J. Oh, J. S. Yang, D.-H. Kim, S. D. Bu, T.-W. Noh, H.-J. Lin, H.-H. Hsieh and C. T. Chen, Phys. Rev. Lett., **90** 017401 (2003)

[2] J. Philip, N. Theodoropoulou, G. Berera, J. S. Moodera and B. Satpati, Appl. Phys. Lett., **85** 777 (2004)

[3] J. S. Higgins, S. R. Shinde, S. B. Ogale, T. Venkatesan and R. L. Greene, Phys. Rev. B, **69** 073201 (2004)

[4] J. M. D. Coey, M. Venkatesan and C. B. Fitzgerald, submitted to Nature Materials

[5] P. Esquinazi et al, cond-mat/0203153 7 Mar 2002

[6] R. Höhne and P. Esquinazi, Adv. Mater., **14** 753 (2002)

[7] T. L. Makarova et al Nature **413** 716 (2001)

Publications

[1] *SnO_2 doped with Mn, Fe or Co: Room temperature dilute magnetic semiconductors,* C. B. Fitzgerald, M. Venkatesan, A. P. Douvalis, S. Huber, J. M. D. Coey and T. Bakas, J. Appl. Phys., **95** 7390 (2004)

[2] *Ferromagnetism in Fe-doped SnO_2 thin films,* J. M. D. Coey, A. P. Douvalis, C. B. Fitzgerald and M. Venkatesan, Appl. Phys. Lett., **84** 1332 (2004)

[3] *Cobalt doped ZnO – a room temperature dilute magnetic semiconductor,* C. B. Fitzgerald, M. Venkatesan, J. G. Lunney, L. S. Dorneles and J. M. D. Coey, presented as a poster at the EMRS in Strasbourg in May 2004, to be published in Applied Surface Science

[4] *Ferromagnetism in substituted zinc oxide*, M. Venkatesan, C. B. Fitzgerald, J. G. Lunney and J. M. D. Coey, in press Physical Review Letters

[5] *Anisotropy of the magnetisation of a dilute magnetic oxide*, J. M. D. Coey, M. Venkatesan, C. B. Fitzgerald, L. S. Dorneles, P. Stamenov and J. G. Lunney, presented at the JEMS Conference in Dresden September 2004, to be published in Journal of Magnetism and Magnetic Materials

[6] *Structural and compositional analysis of ferromagnetic wide bandgap semiconductor PLD thin films,* L. S. Dorneles, D. O'Mahony, C. B. Fitzgerald, F. McGee, M. Venkatesan, I. Stanca, J. G. Lunney and J. M. D. Coey, submitted to Applied Surface Science

[7] *Unexpected magnetism in a dielectric oxide*, M. Venkatesan, C. B. Fitzgerald and J. M. D. Coey, Nature **430** 630 (2004)

[8] *Magnetism in hafnium dioxide*, J. M. D. Coey, M. Venkatesan, L. S. Dorneles, C. B. Fitzgerald and P. Stamenov, with reviewers, Physical Review B, Rapid Communications

[9] *Exchange in dilute ferromagnetic oxides*, J. M. D. Coey, M. Venkatesan and C. B. Fitzgerald, submitted to Nature Materials, currently with referees

[10] *Ferromagnetism of a graphite nodule from the Canyon Diablo meteorite,* J. M. D. Coey, M. Venkatesan, C. B. Fitzgerald, A. P. Douvalis and I. S. Sanders, Nature **420** 156 (2002)